

DISSERTATION

IN-SITU LASER TAGGING OF BARIUM IONS IN LIQUID XENON FOR THE EXO
EXPERIMENT

Submitted by

Kendy Hall

Department of Physics

In partial fulfillment of the requirements

For the Degree of Doctor of Philosophy

Colorado State University

Fort Collins, Colorado

Spring 2012

Doctoral Committee:

Advisor: William Fairbank

Mario Marconi

Jacob Roberts

Walter Toki

ABSTRACT

IN-SITU LASER TAGGING OF BARIUM IONS IN LIQUID XENON FOR THE EXO EXPERIMENT

The goal of the Enriched Xenon Observatory (EXO) collaboration is to measure the half life of neutrino-less double beta decay using a ton size liquid ^{136}Xe detector with zero background. Zero background detection can only be achieved if the daughter nucleus, ^{136}Ba , can be tagged. The EXO collaboration is investigating several techniques to tag the ^{136}Ba daughter. The goal of this thesis is to investigate the prospects of directly observing a single $^{136}\text{Ba}^+$ ion in the liquid using a laser aimed at the decay site, hence in-situ laser tagging. Because the energy levels of Ba^+ ions are expected to be altered from the vacuum configuration, in-situ laser tagging can only be accomplished if the spectroscopy of the Ba^+ ions in liquid xenon is understood. An ultra pure liquid xenon test apparatus with a liquid xenon purity monitor has been built to study the spectroscopy of the Ba^+ ions. An unexpected discovery of the nonresonant multiphoton ionization of liquid xenon using pulsed UV lasers was made while characterizing the purity monitor. The discovery was vital to the ability to accurately measure the purity of the liquid xenon. The spectroscopy of Ba^+ ions in liquid xenon and the multiphoton ionization studies are the two key topics that are presented in this thesis.

TABLE OF CONTENTS

1	Introductory	1
1.1	Neutrinos	1
1.2	Massive Neutrinos	2
1.3	Absolute Neutrino Mass	5
1.4	Neutrinoless Double Beta Decay	6
1.5	Enriched Xenon Observatory	7
1.5.1	EXO-200	8
1.5.2	FULL EXO	10
2	Physics Background	14
2.1	Spectroscopy	15
2.1.1	Ba ⁺ Vacuum Energy Levels	15
2.1.2	Analogs for Ba ⁺ in liquid xenon	16
2.1.3	Expected emission signal of Ba ⁺ ions in liquid xenon	19
2.2	Nonresonant Multiphoton Ionization	21
3	Apparatus	25
3.1	LXe System	25
3.1.1	Gas Handling System	27
3.1.2	Xenon Cell	28
3.1.3	Cryogenics	31
3.2	Ba ⁺ Ion Creation	33
3.2.1	Laser Ablation	34
3.2.2	Ba ⁺ ion detection	35
3.3	Liquid Xenon Purity Monitor	40

3.3.1	ICARUS Liquid Xenon Purity Monitor	41
3.3.2	CSU Liquid Xenon Purity Monitor	42
3.4	Nonresonant Multiphoton Ionization of LXe	44
3.5	Spectroscopy	51
3.5.1	Fluorescence Spectra setup	55
3.5.2	Plasma Emission Setup	56
3.5.3	Time Resolved Fluorescence	58
3.5.4	Collection Efficiency	59
4	Results: Nonresonant Multiphoton Ionization	61
4.1	Order n of the Multiphoton Process	62
4.2	Cross Section Calculations	64
4.3	Discussion	66
5	Results: Ba⁺ Spectroscopy	69
5.1	Plasma Emission Spectra	70
5.2	Observed Fluorescence Spectra	73
5.3	Time Resolved Spectroscopy	75
5.3.1	Oxidized Ba Metal Experiments	79
5.3.2	Cleaned Ba Metal and BaAl ₄	90
5.4	Discussion	98
6	Summary	99
	Bibliography	101

Chapter 1

Introductory

1.1 Neutrinos

Neutrinos were first postulated in a letter sent from Wolfgang Pauli to the participants of the 1930 Tübingen physics conference to address the continuous spectrum of β^- emission which implied that energy and angular momentum was not conserved [1] [2]. At the time, β decay was only thought to be a two-body radioactive process in which an unstable nucleus releases an electron or positron (both β particles) as it changed to a more stable nucleus according to the equation,



Pauli proposed the neutrino to carry away the missing energy and angular momentum and postulated the neutrino as a massless, electrical neutral particle with spin of $\frac{1}{2}$. Although not detectable yet, the neutrino was a viable solution to the β decay problem. The particle was actually coined as the neutrino by Fermi in his theory of beta decay because the original name, neutron, was given to the particle recently discovered by Chadwick [3].

The first experimental evidence of neutrino interactions came from the inverse beta decay experiments

$$\bar{\nu}_e + p^+ \rightarrow \beta^+ + n \quad (1.2)$$

reported by Clyde Cowan and Frederick Reines in the summer of 1956 [4]. Experiments providing evidence that β^- decay and β^+ produced different types of neutrinos were conducted. Those experiments implied that the neutrino has a corresponding anti-particle, the antineutrino. The β decay process is given by

$${}^A_Z X \rightarrow {}^A_{Z+1} Y ({}^A_{Z-1} Y) + e^- (e^+) + \nu_e (\bar{\nu}_e). \quad (1.3)$$

Experiments observing discrepancies in muon energy from pion decay confirmed the existence of the muon neutrino and its antiparticle followed from a group lead by Lederman, Schwartz, and Steinberger [5]. Lastly, the tau particle discovery from a series of experiment conducted from 1974-1977 by Perl implied the existence of tau neutrinos and antineutrinos [6]. It took almost 30 years until DONUT group [7] first observed the tau neutrino.

1.2 Massive Neutrinos

The idea that neutrinos could be massive particles was first introduced by Pontecorvo [8]. He postulated that a neutrino flavor could change to another flavor (or oscillate) as it propagates through space. This directly implied that they are not massless because the observed weak eigenstates are a linear superposition of the mass eigenstates. Thus,

$$|\nu_\alpha\rangle = \sum_i U_{\alpha i}^* |m_i\rangle \quad (1.4)$$

where $|\nu_\alpha\rangle$ ($\alpha = e, \mu, \tau$) are the weak eigenstates, $|m_i\rangle$ ($i = 1, 2, 3$) are the mass eigenstates, and $U_{\alpha,i}$ is the Pontecorvo-Maki-Nakagawa-Sakata (PMNS) leptonic mixing matrix. For the

full 3 flavor oscillation matrix $U_{\alpha,i}$ can be written as

$$U_{\alpha,i} = \begin{bmatrix} 1 & 0 & 0 \\ 0 & c_{23} & s_{23} \\ 0 & -s_{23} & c_{23} \end{bmatrix} \begin{bmatrix} c_{13} & 0 & s_{13}e^{i\delta} \\ 0 & 1 & 0 \\ -s_{13}e^{i\delta} & 0 & c_{13} \end{bmatrix} \begin{bmatrix} c_{12} & s_{12} & 0 \\ -s_{12} & c_{12} & 0 \\ 0 & 0 & 1 \end{bmatrix} \begin{bmatrix} e^{i\alpha_1/2} & 0 & 0 \\ 0 & e^{i\alpha_2/2} & 0 \\ 0 & 0 & 1 \end{bmatrix} \quad (1.5)$$

where $c_{ij} \equiv \cos\theta_{ij}$ and $s_{ij} \equiv \sin\theta_{ij}$. The mixing angle between mass states i and j is θ_{ij} , and δ is the Charge-Parity (CP) violating phase, which is zero if CP violation holds. The phases $\alpha_{1,2}$ are Majorana phases that are nonzero if the neutrinos are shown to be Majorana particles ($\nu_\alpha = \bar{\nu}_\alpha$) [9] [10].

In the case that only two neutrinos significantly participate in the oscillation, the effective mixing, U , matrix becomes

$$U = \begin{bmatrix} \cos\theta & \sin\theta \\ -\sin\theta & \cos\theta \end{bmatrix} \quad (1.6)$$

The propagation a neutrino in any mass eigenstate, $|\nu_i\rangle$, as it travels from the source of origin to the detector is described by a plane wave solution in quantum mechanics

$$|\nu_i(t)\rangle = e^{-i(E_it - \vec{p}_i \cdot \vec{x})} |\nu_i(0)\rangle \quad (1.7)$$

and simplifies to

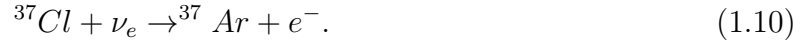
$$|\nu_i(L)\rangle = e^{-im_i^2 \frac{L}{2E}} |\nu_i(0)\rangle \quad (1.8)$$

in the ultra-relativistic limit since neutrinos travel close to the speed of light. The probability that a ν_α will be observed as ν_β is given by

$$P(\nu_\alpha \rightarrow \nu_\beta) = \sin^2(2\theta) \sin^2\left(1.27 \frac{\Delta m^2(\text{eV})L(\text{km})}{E(\text{GeV})}\right) \quad (1.9)$$

where E is the energy, L is the distance traveled and, $\Delta m^2 \equiv |m_i^2 - m_j^2|$ is the mass difference.

The experiment conducted by Ray Davis in the Homestake Mine in South Dakota is credited as the first observation of neutrino oscillations [11]. The goal of the experiment was to measure the solar neutrinos predicted by the Standard Solar Model(SSM) from the process



The Standard Solar Model(SSM) was well developed at the time and it predicted the total solar neutrino flux from the sun to be 8.1 ± 1.2 SNU (1 SNU= 10^{-36} neutrino interactions per target atom per second). The results of the Homestake Mine experiment was a neutrino flux of 2.56 ± 0.25 SNU which was much smaller than neutrino flux predicted by the SSM. The discrepancy was known as the Solar Neutrino Problem. The Homestake Mine experiment was only sensitive to the detection of electron neutrinos, and the deficit in the flux was due to the electron neutrino oscillating to a different flavor as postulated by Pontecorvo. Many other experiments have since observed neutrino oscillations; thus providing strong evidence of neutrinos having mass. SNO [12], SAGE [13], and GALLEX/GNO [14], are a few other solar neutrino experiments. Atmospheric neutrinos have been observed from the interaction of cosmic rays with atomic nuclei in the atmosphere in the experiments by IMB [15], Kamiokande [16], and SuperKomiakande [17]. Neutrino oscillations have also been observed from neutrinos produced from nuclear reactors and neutrino beams from particle accelerators. These experiments are conducted by collaborations such as T2K [18], MINOS [19], and KamLAND [20]. A more exhaustive list can be found in many review articles [21].

The current values of the mixing angles and Δm^2 s from the many neutrino oscillation experiments are summarized in a review article by Altarelli [22]

$$\sin^2(\theta_{12}) = 0.312 \pm_{0.018}^{0.019} \quad (1.11)$$

$$\sin^2(\theta_{23}) = 0.466 \pm_{0.058}^{0.073} \quad (1.12)$$

$$\sin^2(\theta_{13}) < 0.016 \pm 0.010 \quad (1.13)$$

$$|\Delta m_{23}^2| = 2.39 \pm_{0.08}^{0.11} \times 10^{-3} eV^2 \quad (1.14)$$

$$\Delta m_{12}^2 = 7.67 \pm_{0.19}^{0.16} \times 10^{-5} eV^2 \quad (1.15)$$

$$(1.16)$$

Neutrino oscillation experiments are only sensitive to Δm^2 , and the individual masses of the neutrinos cannot be determined.

1.3 Absolute Neutrino Mass

Direct measurements are needed to determine the absolute masses, and are being pursued by a number of groups. Direct measurements consist of the precise observation of weak decays involving any of the three neutrino flavors, such as the Mainz and Troitzk experiments, in which the shape of the β^- - decay spectrum of tritium(3He) is measured at the endpoint. The results of these experiments yields, $m_{\bar{\nu}_e} < 2.3eV$, at the 95% confidence level [23]. The current KATRIN experiment is measuring the same β^- decay spectrum and expects to reach a sensitivity of $m_{\bar{\nu}_e} 0.20eV$ [24]. Cosmological neutrino experiments measure the sum of three neutrino masses from the remnants left behind after the big bag or supernova events [25]. The combined results are model dependent with a current limit $\Sigma m_\nu < 0.28eV$ for the combined 3 masses. The search for the nuetrinoless double decay ($0\nu\beta\beta$) process is a way of measuring the absolute electron neutrino mass, with the possibility of probing down to the meV mass scale. This is the detection method of choice for the EXO collaboration.

1.4 Neutrinoless Double Beta Decay

Neutrinoless double beta decay ($0\nu\beta\beta$) is similar to the allowed double beta decay ($2\nu\beta\beta$) process given as

$$(Z, A) \rightarrow (Z + 2, A) + 2e^- + 2\bar{\nu}_e \quad (1.17)$$

where two anti-neutrinos are emitted. Double beta decay is a second-order process in the Standard Model that can only be observed in isotopes in which β decay is energetically forbidden or strongly suppressed so that there is no competition with the $2\nu\beta\beta$ decay. Otherwise the event rate of β decay would dominate. There are 35 naturally occurring isotopes that can undergo $2\nu\beta\beta$ that would serve as possible candidates to observe the rare $0\nu\beta\beta$ [1].

Neutrinoless double beta decay may exist in the following form

$$(Z, A) \rightarrow (Z + 2, A) + 2e^-. \quad (1.18)$$

A nucleus with charge Z and mass A decays into a nucleus with charge $Z+2$ and mass A releasing only two electrons. This process is currently forbidden by the standard model since no anti-neutrinos are released, violating lepton number conservation. If $0\nu\beta\beta$ is detected, it implies that the neutrino and anti-neutrino are the same particle and would be the first evidence of a Majorana particle. The effective neutrino mass is given by [26].

$$\langle m_{\beta\beta} \rangle = \left| \sum_i U_{ei}^2 m_i \right| \quad (1.19)$$

where U_{ei}^2 is again the PMNS mixing matrix. The effective neutrino mass is related to the half-life of the decay, $T_{1/2}^{0\nu\beta\beta}$, by

$$\langle m_{\beta\beta} \rangle = \left(T_{1/2}^{0\nu\beta\beta} G^{0\nu\beta\beta}(Q, Z) \left| M_G^{0\nu\beta\beta} - \frac{g_V^2}{g_A^2} M_F^{0\nu\beta\beta} \right|^2 \right)^{-\frac{1}{2}} \quad (1.20)$$

where $G^{0\nu\beta\beta}(Q, Z)$ is a phase-space factor depending on the decay end point energy Q and the nuclear charge Z . $M_{GT}^{0\nu\beta\beta}$ and $M_F^{0\nu\beta\beta}$ are the Gamov-Teller and Fermi nuclear matrix elements, and $g_{V,A}$, are the vector (V) and axial-vector (A) coupling constants. The nuclear mixing elements must be calculated based upon theoretical models and are the dominate uncertainty in the conversion from $T_{1/2}^{0\nu\beta\beta}$ to $\langle m_{\beta\beta} \rangle$.

Including the recent observation by our collaboration, $2\nu\beta\beta$ had been observed in about 12 isotopes with measured half-life varying from 10^{18}yr to 10^{24}yr [1] [27]. The observation of $2\nu\beta\beta$ gives important information about the nuclear structure of the decay that might be useful for the calculation of the values of the nuclear matrix elements of the $0\nu\beta\beta$ mode [28]. Neutrinoless double beta decay has only been claimed to be observed by subset of collaborators of the Heidelberg-Moscow group [29] [30]. The results are controversial; even members of the same collaborators refute aspect of analysis used to make the claim. A note from members in the neutrino physics community has addressed the claim [31].

Experimentally $0\nu\beta\beta$ and $2\nu\beta\beta$ are distinguished by the different energy distributions of the two electrons, as shown in Figure 1.1. For $2\nu\beta\beta$, the electron energy spectrum is a broad continuum, due to sharing of the energy with the neutrinos that are not detected, that ends at the decay Q -value. For $0\nu\beta\beta$, the electron energy is approximately a delta function at the Q -value but will be broadened by the resolution of the detector. If $0\nu\beta\beta$ exists, it will be an extremely rare decay. Thus a detector with a large isotopically enriched source mass with good energy resolution and nearly zero background would enhance the ability to observe the $0\nu\beta\beta$ process.

1.5 Enriched Xenon Observatory

The goal of the Enriched Xenon Observatory (EXO) collaboration is to measure $0\nu\beta\beta$ half-life using 80% enriched ^{136}Xe xenon as the parent decay nucleus in a 1-10 ton xenon time projection chamber (TPC). The TPC measures the energy of the two electrons and determines the location of the decay site. The $0\nu\beta\beta$ decay that EXO plans to observe is

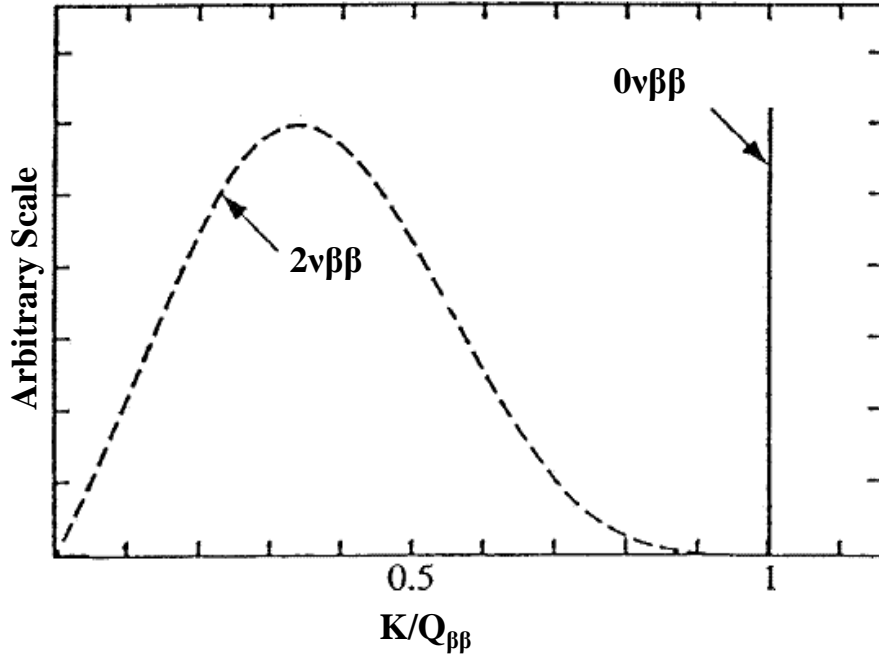


Figure 1.1: The summed energy spectra for $2\nu\beta\beta$ and $0\nu\beta\beta$. K is the combined energy of the electrons

the following



1.5.1 EXO-200

EXO-200 is the current detector of the EXO collaboration. The purpose of the smaller detector is to develop the techniques of working with liquid xenon in a time projection chamber (TPC), procure low background materials, and to develop background removal techniques; as well as to measure the $2\nu\beta\beta$ half-life of ^{136}Xe , and to possibly measure $0\nu\beta\beta$ or to establish a mass limit of $\sim 0.2\text{eV}$. The EXO-200 detector is a 200kg liquid xenon TPC enriched to 80% ^{136}Xe located at the Waste Isolation Pilot Plant (WIPP) southeast of Carlsbad, NM in a salt deposit that is at a depth of about 1600 meters of water equivalent.

A schematic drawing of the class 1000 clean room that houses the detector, as it is installed in the mine, is shown in Figure 1.2. The TPC sits inside a double walled vacuum

cryostat. The cryostat is filled with HFE7000 fluid (HFE) that cools that TPC to approximately 167K and that also provides thermal stability. The temperature of the HFE is controlled by large refrigerators. Copper feed-through ports are welded onto the cryostat for all electrical connections to the TPC, and for the supply and return line for each the xenon gas and the HFE lines. The cryostat itself is enclosed in a lead structure for radioactive shielding. A conceptual diagram of TPC operation is shown in Figure 1.3. The EXO-200

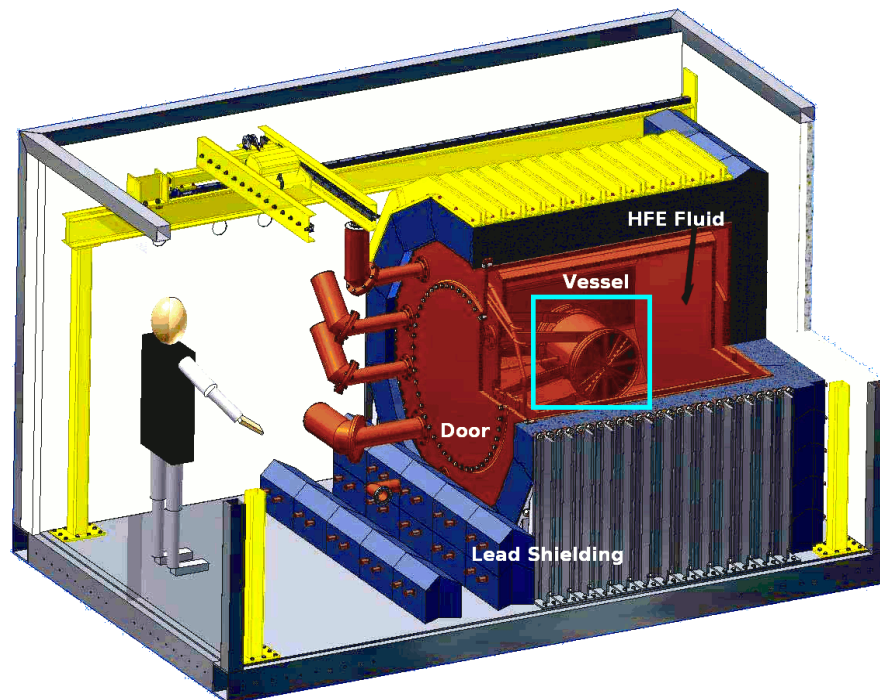


Figure 1.2: The EXO-200 detector

TPC has cylindrical symmetry with a diameter and length of approximately 40cm. The cathode grid divides the detector into two halves with anode planes at the end of each half. The grids measure the energy of the electrons. Each anode plane consists of two sets of grid wires crossed at a 60° angle that also provide two dimensional location of the ionizing event. Behind the grids is an array of approximately 250 large-area avalanche photodiodes (LAAPDs) that allow for the readout of the scintillation in the liquid xenon. The LAAPDs give a time stamp of the ionizing event, and combined with the two dimensional location from the crossed grids, provide 3-dimensional positioning of an ionizing event. An official paper

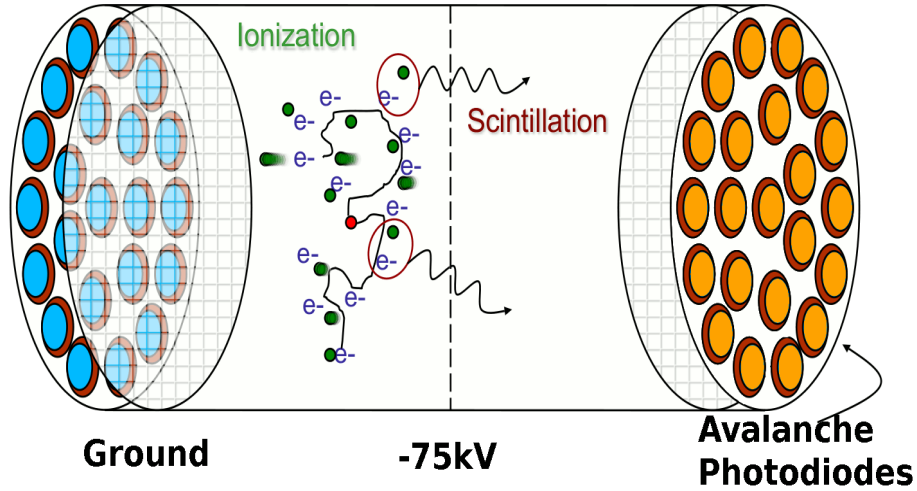


Figure 1.3: The EXO-200 TPC

explaining the EXO-200 detector in more detail has been accepted for publication [32]. The EXO collaboration has successfully used the EXO-200 detector to make the first measurement of the half-life of the $2\nu\beta\beta$ decay mode of ^{136}Xe , $T_{1/2} = 2.11 \pm 0.04(\text{stat}) \pm 0.21(\text{sys}) \times 10^{21}$ yr [27].

1.5.2 FULL EXO

In the planned 1-10 ton liquid xenon TPC detector, Full EXO, zero background detection is expected to be achieved by tagging the barium daughter ion in the reaction (1.21). The idea of tagging the daughter ion was first introduced by Moe [33]. He proposed using a laser to excite the barium ion and then to collect the light from the emission, thus distinguishing a $0\nu\beta\beta$ or $2\nu\beta\beta$ decay event from all background events. Moe thought that tagging the daughter ion in the liquid xenon with lasers could be accomplished since it was known that the mobility of positive ions in liquid xenon was relatively low. Our group at CSU has provided the only measurement of the mobility of Ba^+ ions in liquid xenon to, $\mu = 0.000211^{+20}_{-12}$ $\text{cm}^2\text{V}^{-1}\text{s}^{-1}$ [34], confirming that the daughter ion would not move very quickly from its origin in the detector. Thus, there should be plenty time tag the daughter ion.

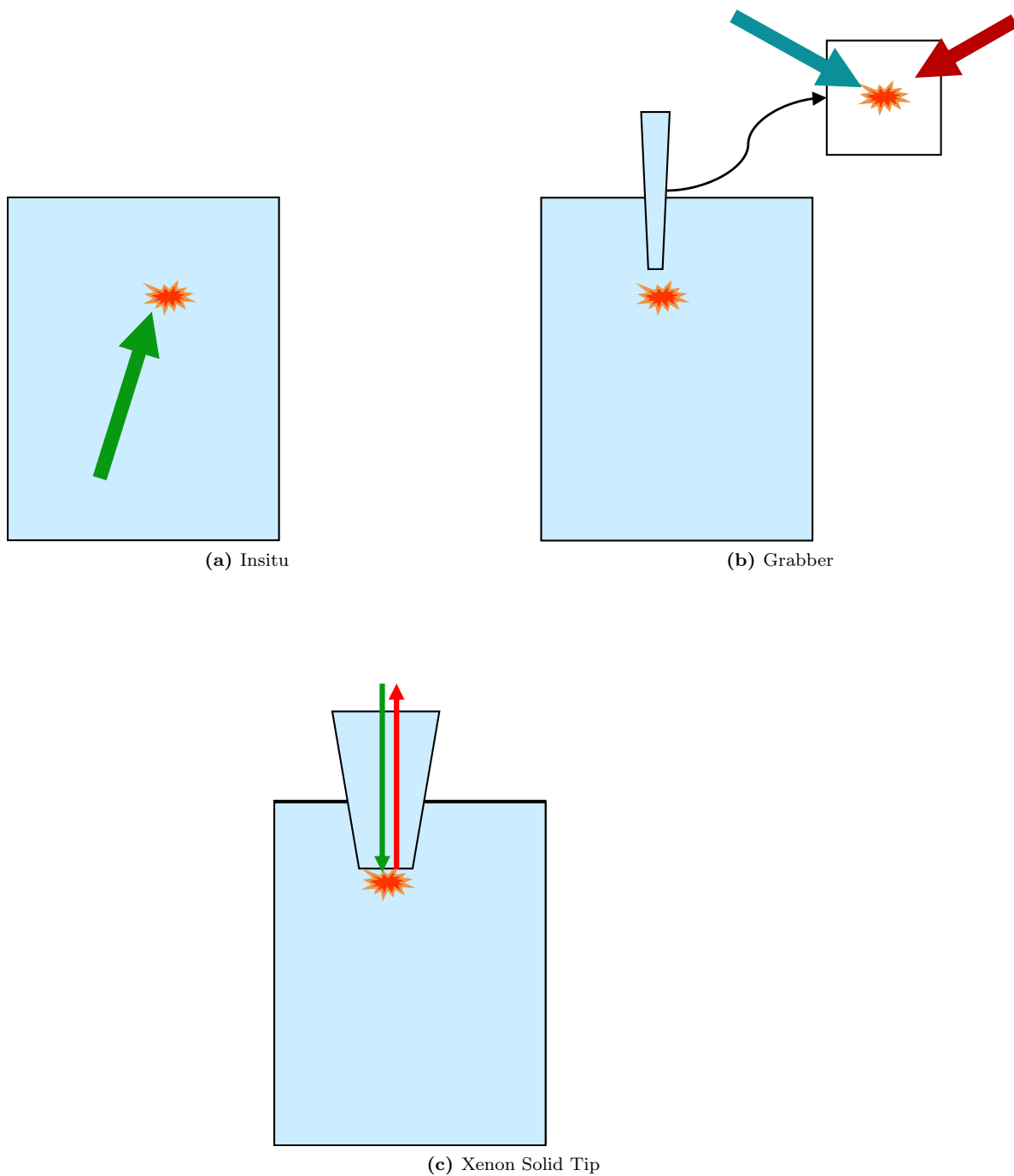


Figure 1.4: The full EXO tagging schemes: (a) Direct tagging in the liquid xenon, (b) Ba^+ ion grabber and confirmation rf-trap, (c) Direct tagging in the liquid on a solid xenon tip

EXO is currently investigating several techniques to tag the daughter ion in liquid xenon using the three general schemes shown in Figure 1.4: (1) in-situ tagging in the liquid by

bringing lasers into the TPC and collecting the fluorescence light; (2) grabbing the Ba^+ ion, fetching it out of the TPC, and releasing it into an rf-linear Paul trap to observe the fluorescence in vacuum; and (3) freezing the Ba^+ ion in a solid xenon matrix and detecting the fluorescence while it is in the TPC.

The goal of this thesis work is to investigate the prospects of directly observing the daughter ion as shown in Figure 1.4a. Direct tagging of the $^{136}Ba^{++}$ daughter with a laser is only possible in the liquid xenon detector if the $^{136}Ba^{++}$ ion is able to grab an electron from liquid xenon in the following process



where Xe^{h+} is a hole left in the liquid xenon valance band [33]. The process listed in Equation 1.22 has not be proven yet. It is completely forbidden in xenon gas because the ionization potential of xenon gas is higher than that of Ba^+ . The band gap of liquid xenon is lower as seen in Figure 1.5, thus the process should be possible.

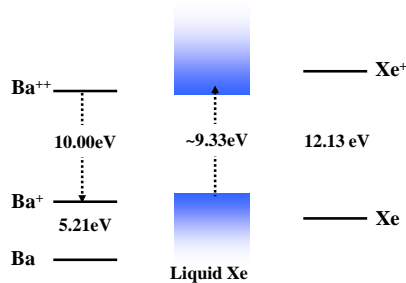


Figure 1.5: The ionization potential of Ba, Xe, and the band structure of liquid xenon

In order to accomplish in-situ tagging in the liquid, one must first understand the Ba^+ energy levels since they are expected to be altered from the vacuum configuration due to the interaction of the Ba^+ ions with the xenon atoms. We have designed an ultra-pure liquid xenon test chamber to study the spectroscopy of the Ba^+ ions in liquid xenon which Ba^+ ions are injected into the liquid xenon. The biggest advantages of detecting the Ba^+ ion in-situ are that it is simple, it is non invasive to the ion, the method can be used to track

the ion in the liquid xenon, and it can in principle be used in combination with any tagging technique. The engineering of the actual collection of the fluorescence light in a TPC is the greatest design challenge.

Chapter 2

Physics Background

The relevant physics background and the theory that support the experimental work of this thesis are discussed in this Chapter. The Ba^+ ionic energy levels in vacuum are explained first in Section 2.1.1. The spectroscopic studies of Ba^+ and Yb^+ ions in liquid helium are the only other atomic ions in liquid noble gases found in the literature in which we can use to draw comparison to Ba^+ in liquid xenon. The preliminary studies of Ba^+ ions in liquid xenon performed prior to this thesis work will be discussed later in Chapter 5. Mobility studies performed by our group have provided some evidence that the Ba^+ ions might be surrounded by 1-2 layers of xenon ice [34]. Thus, in parallel with this thesis, Ba^+ ions studies in solid xenon were conducted to initially aid the liquid xenon studies. To our knowledge, Ca^+ ions in solid argon are the only other optical studies of an atomic ion in a solid noble gas. A greater collection of experiments on neutral metal atoms in different solid noble gas matrices exist in the literature. Spectra for two alkali neutral atoms in three of the solid noble gases will be discussed in Section 2.1.2. The absorption cross section for Ba^+ ions in liquid xenon is predicted assuming a reasonable broadening of the absorption band in Section 2.1.3. It is used to predict the ability to detect Ba^+ ions in our test system under favorable fluorescence assumptions and helps guide the design of the experimental setup. The chapter concludes with Section 2.2 in which the background and theoretical details for

measurement the of Non Resonant Multi-Photon Ionization (NRMPI) cross section of liquid xenon with different wavelengths of pulsed UV light is presented.

2.1 Spectroscopy

2.1.1 Ba⁺ Vacuum Energy Levels

The lowest atomic energy levels of Ba⁺ in vacuum are shown in Figure 2.1. The ground

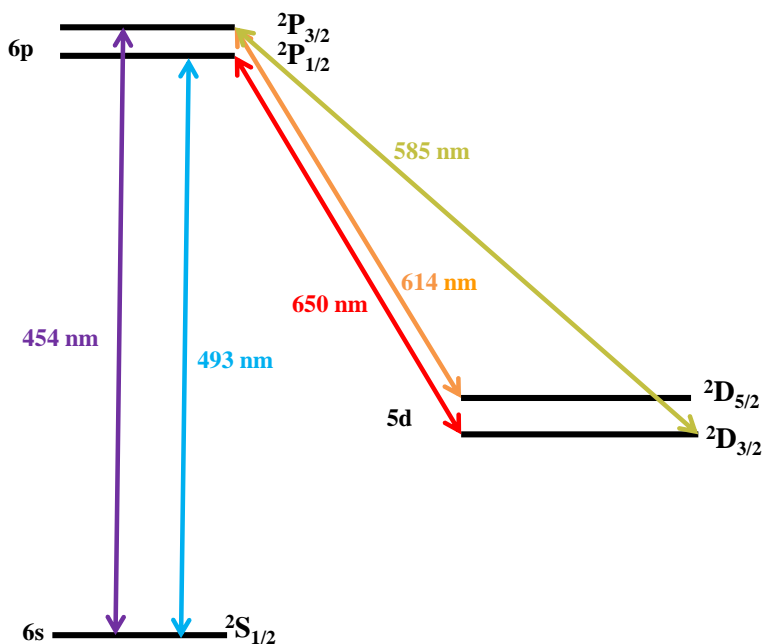


Figure 2.1: Ba⁺ vacuum energy levels

state is the 6s ²S_{1/2} state. There are two strong transitions from the ground state to the excited 6p state, ²P_{1/2} and ²P_{3/2}, corresponding to 455nm and 493nm, with spontaneous decay rates of $1.11 \times 10^8 \text{ s}^{-1}$ and $9.53 \times 10^7 \text{ s}^{-1}$ respectively. According to the electron dipole selection rules, once excited to the 6p states, the ions can decay back to the ground state or to the metastable 5d states. The ions in the excited 6p ²P_{3/2} state can decay to either the 5d ²D_{3/2} or 5d ²D_{5/2} states, giving off 585nm ($A=6.00 \times 10^6 \text{ s}^{-1}$) and 614nm ($A=4.12 \times 10^7 \text{ s}^{-1}$) light respectively. The ions in the excited 6p ²P_{1/2} state, can only decay to the 5d ²D_{3/2} state giving

off 650nm ($A=3.10 \times 10^7 \text{ s}^{-1}$) light. The metastable 5d states have lifetimes greater than 30s for decay to the 6s ground state [35]. To observe Ba^+ in vacuum it is necessary to use two lasers: one laser at 493nm to excite from the ground state to the $6p \ ^2P_{1/2}$ excited state and another laser at 650nm to repump the ions out of the metastable $5d \ ^2D_{3/2}$ state.

2.1.2 Analogs for Ba^+ in liquid xenon

The excitation spectra of Ba^+ ions in liquid helium obtained by Reyher et al. are shown in Figure 2.2 [36]. A splitting in one of the absorptions bands was observed. The splitting

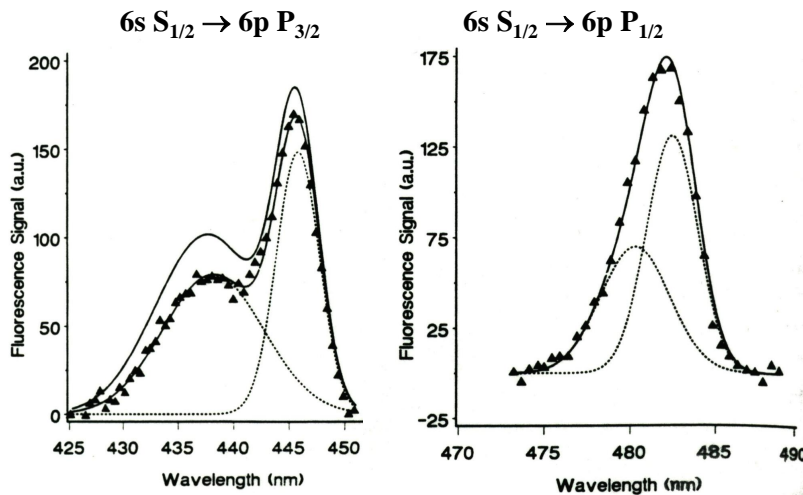


Figure 2.2: Excitation spectra of Ba^+ ions in liquid helium. The $6s \ ^2S_{1/2} \rightarrow 6p \ ^2P_{3/2}$ transition shows a splitting into two peaks due to the Jahn-Teller effect. Reprinted from Physics Letters A, 115, H.J. Reyher and H. Bauer and C. Huber and R. Mayer and A. Schfer and A. Winnacker, Spectroscopy of barium ions in He II, 238-244, Copyright (1981), with permission from Elsevier.

is due to the Jahn-Teller effect: Every nonlinear molecule or crystal defect that has orbital electronic degeneracy when the nuclei are in a symmetrical configuration is unstable with respect to at least one asymmetric distortion of the nuclei which lifts the degeneracy [37]. Thus it was concluded that three absorption bands from the ground 6s state to the first excited 6p states should exist. The absorptions bands are blue shifted from the vacuum transitions. Only three emission bands in the range 400nm-800nm were observed, peaked at

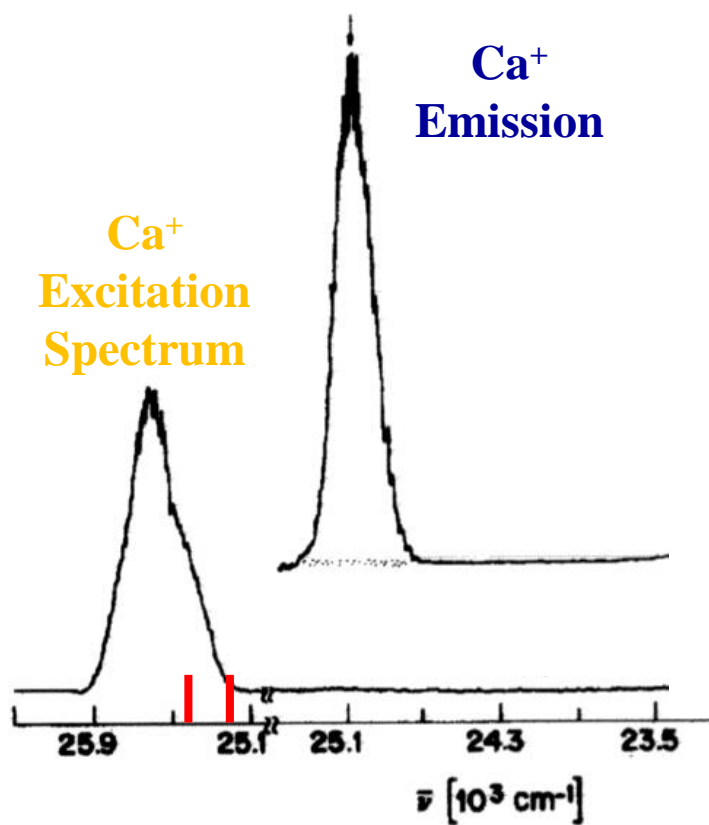
491nm, 523nm, and 648nm with approximately FWHM of 2nm, 10nm and 4nm respectively. From a detailed analysis, it was shown that the 491nm and 648nm emission bands are emission from the 6p excited states. The origin of the 523nm emission was unclear to the authors.

Another way of understanding the atomic/molecular structure of ions in liquid noble gases is from mobility measurements. There are many mobility measurements for monatomic and molecular ions in liquid helium, but limited mobility experimental studies exist for ions in the other liquid noble gases. Fortunately, the measurement of the mobility of Mg^+ , Ca^+ , Sr^+ , and Ba^+ ions in liquid xenon was concluded at the onset of this thesis work [34]. The results provided evidence that the 1-2 layers of solid xenon forms around the Ba^+ ions in what is known as a snowball structure. It is caused by the charge-induced dipole attraction between the Ba^+ ion with neighboring xenon atoms [38]. The 1-2 layers of solid xenon surrounding the ions support the idea that the energy level configuration of the Ba^+ ions in liquid xenon will be similar to that of the Ba^+ ions in solid xenon.

Given that a thesis and a paper are in progress, spectra on Ba^+ ions in solid xenon are not discussed in detail. It will only be mentioned that one absorption band and five emission lines have been observed. Evidence for strong parity violating transitions from the 5d state back to the ground state in the matrix was discovered. The absorption band is shifted from the vacuum transitions, and all the emission lines are red shifted from the absorption.

The absorption and emission spectra of Ca^+ in solid argon reported by Bondebey and English are shown in Figure 2.3 [39]. One asymmetric absorption band that overlapped the spin-orbit split of the 4p vacuum states was observed. One symmetric emission band was also observed. The blue shift of the absorption relative to the vacuum transitions was modest, with the emission line being red shifted.

The qualitative observations shown above for ions in noble gas matrices are also found in the optical studies of neutral atoms in solid noble gas matrices, especially the red shift of the emission lines from the absorption bands. In the white light absorption spectra of



I: Gas phase transitions

Figure 2.3: Excitation and emission spectra of Ca^+ ions in solid argon. "Reprinted with permission from V. E. Bondybey and J. H. English, *J. Chem. Phys.* 71, Copyright 2005, American Institute of Physics."

Na[40] and K [41] in solid Ar, Kr, and Xe, the absorptions bands of both Na and K are shifted from blue to red as the size of the noble gas increased. This is attributed to the increase in polarizability as the noble gases become heavier because the dominant potential that governs the interaction is proportional to the polarizability of the noble gas atom [42].

In summary, the interaction between neutral atoms and ions in a noble gas matrix leads to symmetry breaking, mixing, and degeneracy lifting of the electronic states. This leads to the observation of multiple peaks in the absorption, observations of emission lines that are forbidden in vacuum, and also missing allowed vacuum emission lines. A common observation is that the emission is always red shifted from the absorption. There are other spectral properties and features of metals atoms not mention in this brief discussion. A good review article is written by Crepin-Gilbert and Tramer [42].

2.1.3 Expected emission signal of Ba⁺ ions in liquid xenon

In order to determine the feasibility of conducting an experiment to look for the emission of the Ba⁺ ions in liquid xenon, it is important to have a gauge on the expected size of the fluorescence signal. For a two level system, the expected excitation rate for an atom in a laser beam is determined by the rate of absorption,

$$W_{12} = \sigma_{12}(\nu) \frac{I_\nu}{h\nu} \quad (2.1)$$

where $\sigma_{12}(\nu)$ is the absorption cross section, I is the intensity of the laser, and $h\nu$ is the energy of the laser photon. For a Lorentzian line shape $\sigma_{12}(\nu)$ is given by,

$$\sigma_{12} = \frac{g_2}{g_1} A_{21} \frac{\lambda^2}{8\pi} \left[\frac{\Delta\nu/(2\pi)}{[(\nu - \nu_c)^2 + (\Delta\nu/2)^2]} \right] \quad (2.2)$$

where g_1, g_2 are the degeneracy of the lower and upper states, A_{21} is the radiative decay rate for the transition, ν is the frequency of the laser, ν_c is the center frequency of the absorption line, and $\Delta\nu$ is the absorption line width. When on resonance in vacuum, $\nu = \nu_c$, the

absorption line width is equal to the natural broadening ($\Delta\nu = \Delta\nu_n$), which is $A_{21}/(2\pi)$. Equation 2.2 becomes

$$\sigma_{12} = \frac{g_2 \lambda^2}{g_1 2\pi}. \quad (2.3)$$

From the analogs shown in Section 2.1.2, it is reasonable to assume that there will be broadening in the absorption bands from the ground state to the first excited states. When there is broadening greater than the natural broadening, the absorption cross section on resonance can be approximated by

$$\sigma_{broad} \approx \frac{g_2 \lambda^2 \Delta\nu_n}{g_1 2\pi \Delta\nu}. \quad (2.4)$$

For Ba^+ ions in liquid xenon, an absorption width of 30nm is assumed. This is much larger than the observed width in liquid helium taking, into account the greater polarizability of xenon. The peak absorptions should be red-shifted from the 454nm and 493nm vacuum transitions. This is inferred from the observations seen in the Na and K experiments Ar, Kr, Xe mentioned above. The nine discrete wavelengths of an argon ion laser, in the range of 454nm-514nm, should be suitable to find the resonance absorption given the assumed 30nm width of the absorption band. The absorption cross section with broadening for the $6s \ ^2S_{\frac{1}{2}} \rightarrow 6p^2 P_{\frac{1}{2}} (g_2/g_1 = 1)$ transition then becomes

$$\sigma_{broad} \approx \frac{(500 \times 10^{-5} \text{cm})^2}{2\pi} \times \frac{9.53 \times 10^{-7} \text{s}^{-1}/(2\pi)}{3.6 \times 10^{13} \text{s}^{-1}} \approx 1.7 \times 10^{-15} \text{cm}^2. \quad (2.5)$$

for a peak absorption around 500nm with $\Delta\nu \approx 3.6 \times 10^{13}$ Hz.

With laser excitation, the expected fluorescence rate, R , emitted by one Ba^+ ion is

$$R = \frac{\sigma_{broad}}{A} \times \frac{P}{h\nu} \quad (2.6)$$

where P is the laser power, and A is the $1/e^2$ area of the laser beam. The total number of emitted photons for N Ba^+ ions is

$$n = \frac{\sigma_{braod}}{A} \times \frac{P_\lambda}{hc/\lambda} \times t \times N \quad (2.7)$$

where t is the time the ions are in the laser beam.

In the the calculation of n as shown in Equation 2.7 it is assumed that there are strong parity violating transitions from the 5d state back to the ground state, as observed in the Ba^+ ions in solid xenon, to prevent significant optical pumping. If there is negligible decay of the metastable states during the time that the ions are in the laser beam, they will go out of resonance with the laser beam. In that case, the maximum number of emitted photons is given as

$$n = \frac{1 - \eta}{\eta} \times N \quad (2.8)$$

where η is the branching ratio: the ratio of $p \rightarrow d$ transition probability to the $p \rightarrow s$ transition probability. For Ba^+ in vacuum, $\frac{1-\eta}{\eta}$ is approximately 4 [43].

2.2 Nonresonant Multiphoton Ionization

An atom may be ionized directly by a photon if the energy of the photon, $h\nu$ is equal to or greater than the ionization potential, E_i , of the atom. This process is photoionization. It is also possible for an atom to be ionized by photons with energy, $h\nu$, lower than ionization potential of the atom. The second process can only happen if the photon flux is strong enough that the atom absorbs multiple photons at the same time and is called multiphoton ionization (MPI). MPI was first theorized by Goeppert-Mayer in 1931 [44]. Experimental confirmation of this process was not achievable in those days due to the intense monochromatic radiation that was needed. It was not until after the advent of the Q-switch pulsed ruby laser that experiments testing Goeppert-Mayers theory were done. MPI was first observed by Voronov and Delone by ionizing rare-gas atoms [45].

Two ways in which an atom is ionized by multiple photons are shown in Figure 2.4. In

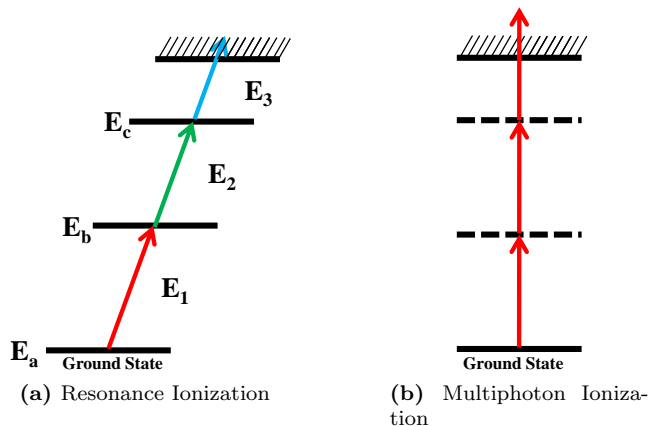


Figure 2.4: This figure shows two ways an atom can be ionized by intense laser light from multiple laser pulse

the first case, Figure 2.4a, absorption of photon E_1 excites the atom to an upper resonant state of the atom, absorption of photon E_2 then excites the atom to an even higher resonant state. The atom is then ionized when it absorbs the photon with energy E_3 . The process is called resonance ionization since the photon energies, E_1 and E_2 , match the resonant transitions between atomic energy levels. In Figure 2.4b the laser photon energies are the same, $E_1 = E_2 = E_3$. The intermediate energy levels are not resonant states of the atom, but are virtual states (represented by the dotted lines). This second case is called nonresonant multiphoton ionization (NRMPI). Because the transitions are nonresonant, pulsed lasers are essential to create the required photon density needed to observe a MPI process. In this thesis, NRMPI of liquid xenon was observed and studied for the first time by collection of the electrons that are freed in the process.

The ionization rate for n-photon NRMPI, from n^{th} order time-dependent perturbation theory, is proportional to laser intensity to the n^{th} power

$$W(\vec{\mathbf{r}}, t) = \sigma^{(n)} \left(\frac{I(\vec{\mathbf{r}}, t)}{E_p} \right)^n . \quad (2.9)$$

Here, n is the minimum number of photons needed to ionize the atom, I is the laser intensity, E_p is the energy of the laser photon, and $\sigma^{(n)}$, is the ionization cross section. Calculation of the number of atoms ionized is determined from rate equations, given as

$$N_{ions} = \int_v n_o \left[1 - \exp \left(- \int_{-\infty}^{\infty} \sigma^{(n)} \left(\frac{I(\vec{\mathbf{r}}, t)}{E_p} \right)^n dt \right) \right] dV \quad (2.10)$$

where n_o is neutral atom density. When the intensity of the laser beam is not high enough to ionize a large fraction of the atoms in the laser beam, Equation 2.10 becomes

$$N_{ions} = n_o \sigma^{(n)} \int_v \int_{-\infty}^{\infty} \left(\frac{I(\vec{\mathbf{r}}, t)}{E_p} \right)^n dt dV. \quad (2.11)$$

The intensity of the laser beam can be separated into temporal and spatial components as

$$I(\vec{\mathbf{r}}, t) = I_{max} F(\vec{\mathbf{r}}) G(t) \quad (2.12)$$

where I_{max} is the maximum laser intensity, in position and time. The function $F(\vec{\mathbf{r}})$ represents a dimensionless spatial distribution function normalized to unity at the center of the focus of the laser beam, and $G(t)$ is a temporal distribution function defined similarly. Defining the following

$$V_n \equiv \int_v [F(\vec{\mathbf{r}})]^n dV \quad (2.13)$$

$$\tau_n \equiv \int_{-\infty}^{\infty} [G(t)]^n dt \quad (2.14)$$

as the effective interaction volume and interaction time respectively, Equation 2.11 becomes

$$N_{ions} = n_o \sigma^{(n)} \tau_n V_n \left(\frac{I_{max}}{E_p} \right)^n. \quad (2.15)$$

Conservation of energy requires that in a lossless medium the energy is constant at any point z measured along the propagation axis of a laser pulse. Thus the energy of the laser

pulse, ϵ can be written as

$$\epsilon = \int I(z, r, \phi, t) r dr d\phi dt. \quad (2.16)$$

By substituting Equation 2.12 and using the definitions assigned in Equation 2.13 and Equation 2.14, Equation 2.16 becomes

$$\epsilon = I_{max} \tau_n \int F(z, r, \phi) r dr d\phi. \quad (2.17)$$

At the focus $z = 0$, Equation 2.17 becomes

$$\epsilon = I_{max} \tau_n \int F(0, r, \phi) r dr d\phi \quad (2.18)$$

Assuming a Gaussian distribution of the laser pulse energy,

$$\int F(0, r, \phi) r dr d\phi = \frac{\pi w_o^2}{2} \equiv A_o \quad (2.19)$$

where, w_o is the $1/e^2$ radius of the focused laser beam. The energy of the laser beam, ϵ , becomes

$$\epsilon = I_{max} \tau_n A_o. \quad (2.20)$$

The number of atoms ionized is equal to the number electrons that are freed in the process, so N_{ions} can be replaced with N_{e^-} . Thus, Equation 2.15 becomes

$$N_{e^-} = n_o \sigma^{(n)} \tau_n V_n \left(\frac{\epsilon}{E_p \tau_n A_o} \right)^n. \quad (2.21)$$

This relationship will be used to determine the order n of the ionization process and the corresponding cross section, σ_n , for the NRMPI of liquid xenon for different pulsed laser wavelengths.

Chapter 3

Apparatus

In this chapter the design of the liquid xenon apparatus and the methods used to carry out the goals of this thesis are explained. The liquid xenon system is described in section 3.1. The Ba^+ ion creation and identification are introduced in section 3.2. In Section 3.3 the liquid xenon purity monitor(LXPM) apparatus is explained with a brief discussion of the results of the purity measurements. The purity monitor measures the survival rate of electrons as they drift through the liquid xenon. In the process of completely understanding the electron creation in the LXPM, it was discovered electron-hole pairs were being created in the liquid xenon by nonresonant multiphoton ionization. The methods used to observe this physical phenomenon are discussed in Section 3.4. The various experimental setups and techniques used in the spectroscopy experiments are explained in the last Section 3.5.

3.1 LXe System

A diagram of the entire liquid system apparatus is given in Figure 3.1. The system is divided into the Vacuum/Cryogenics section and Gas Handling section. Each component of the system in the diagram will be explained in the following subsections. The xenon gas supply and purification system are described first in Subsection 3.1.1. The construction of the xenon cell with the new components for liquid xenon evaporation and re-circulation

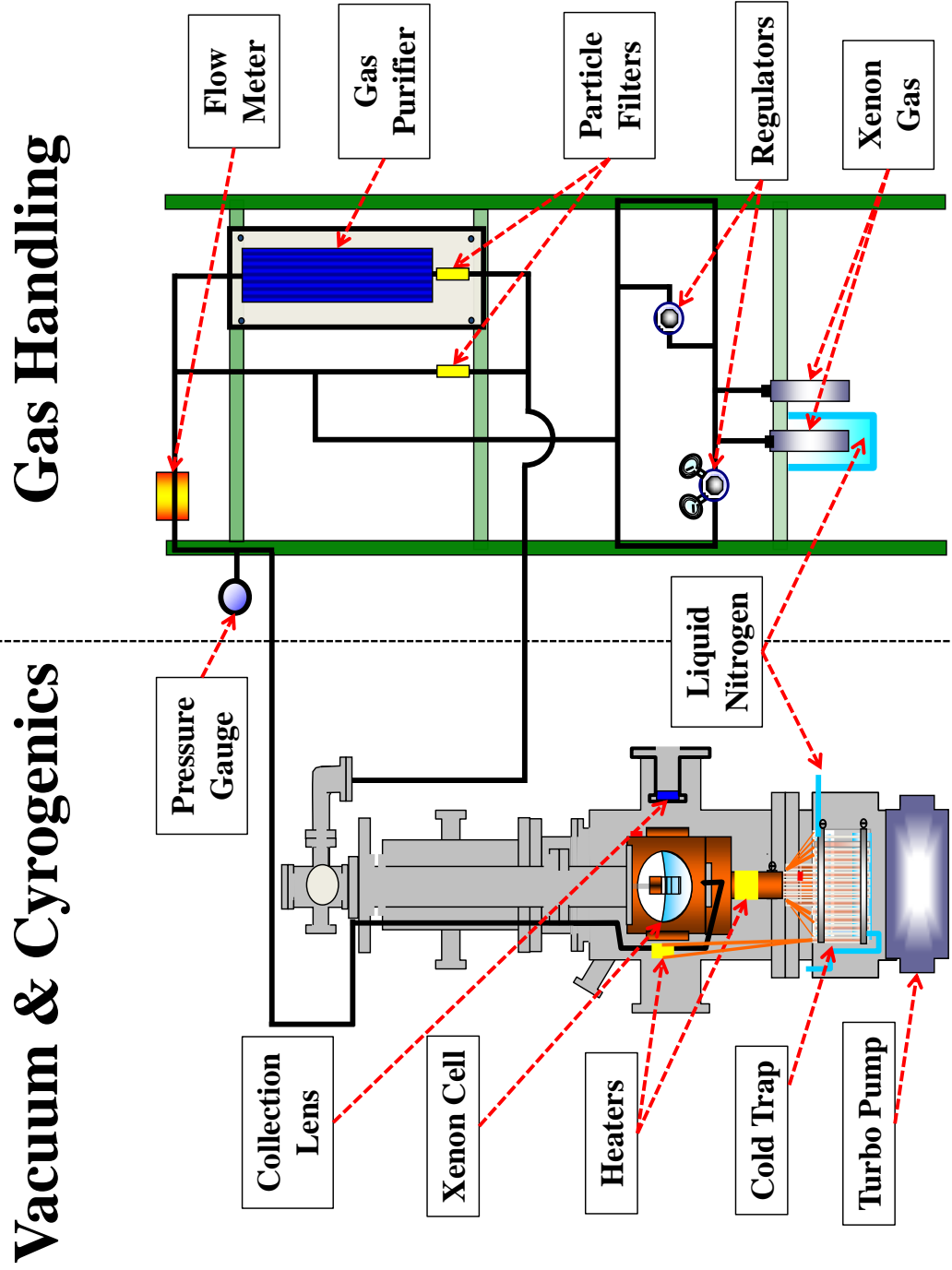


Figure 3.1: Liquid Xenon System. The system is divided into two parts. The components are explained in the text.

is explained in Subsection 3.1.2; the section also includes a detailed description of xenon liquefaction, re-circulation, and recovery of the xenon and the instruments used to monitor and control the system.

3.1.1 Gas Handling System

A simplified flow diagram of the xenon gas system is shown in Figure 3.2. All the gas

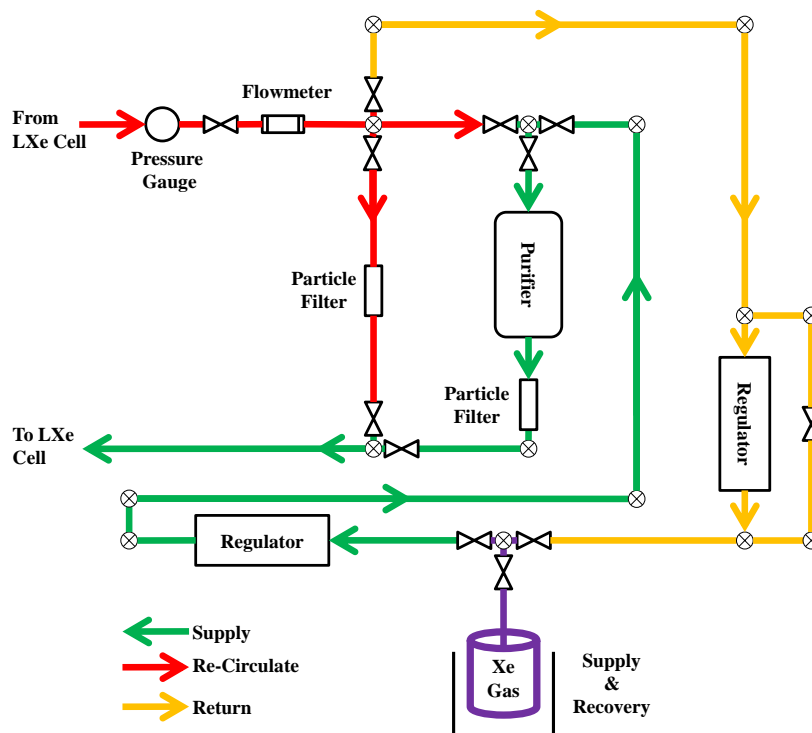


Figure 3.2: Simplified diagram of the gas handling system. The path for condensation (green), recovery (yellow) and re-circulation (red) are shown by the arrows.

transfer lines are 1/4 inch electro-polished stainless-steel tubing with VCR connections and valves. After exposure to air, the transfer lines are baked for three to four days at 120C. The gas supply cylinder is full of 99.999% pure xenon gas with the following specifications: O₂, CO, CO₂, THC, H₂, H₂O, N₂ and other hydrocarbons at the 1 ppm level. During condensation, shown by the green arrows, an ultra high vacuum regulator controls the outlet pressure of the xenon gas supply cylinder as it pushes the gas through the purifier. The

purifier is a SAES MonoTorr rare gas purifier, Model PS3-MT3-R-1. The purifier contains a patented getter alloy that removes impurities by creating irreversible chemical absorption once heated. The operating temperature of the purifier is between 350C to 400C. The purifier is rated for 5 standard liters per minute (SLPM) flow rate at 15 psig pressure drop. With proper usage, the purifier reduces O₂, CO, CO₂, THC, H₂, H₂O, N₂ to the 1 ppb level. At the outlet of the purifier is a particle filter.

During re-circulation, a MKS type 179A flow meter measures the gas flow rate as the xenon gas either bypasses the purifier or flows back through the purifier to re-condense, shown by the red arrows. The purpose of the bypass is to study the flow dynamics of the recirculation system during the testing phases of construction and to study recirculation without purification. The particle filter in the bypass is the same particle filter used after the purifier in order to simulate the same pressure drop that exists when filling through the purifier.

Xenon gas recovery is achieved by cyropumping back into the supply bottles that is placed in a liquid nitrogen bath half way up the bottle. Heater tape is wrapped around the top of the supply bottle to prevent freezing of the valve. The path of recovery is shown by the orange arrows.

3.1.2 Xenon Cell

Temperature stability and adequate optical access are two important considerations in the design of the liquid xenon cell. Thermal instability causes bubbling in the liquid xenon. Bubbling scatters the incoming excitation laser light complicating the ability to collect the Ba⁺ ion fluorescence because of the increase of background scatter from the bubbles. Bubbling also creates noise on the electrodes and large current spikes, making it difficult and sometimes impossible to detect the Ba⁺ ion current signal. The triple point of xenon is 161.35K, and the boiling point is 165.03K. It is critical to control the stability of the liquid xenon to better than 1K to maintain a thermal stability. In order for the liquid xenon cell to

have good thermal stability and to avoid temperature difference that might lead to bubbling, it is built from pure copper.

The liquid xenon cell is shown in Figure 3.3. It is constructed from a 3.82in x 3.82in

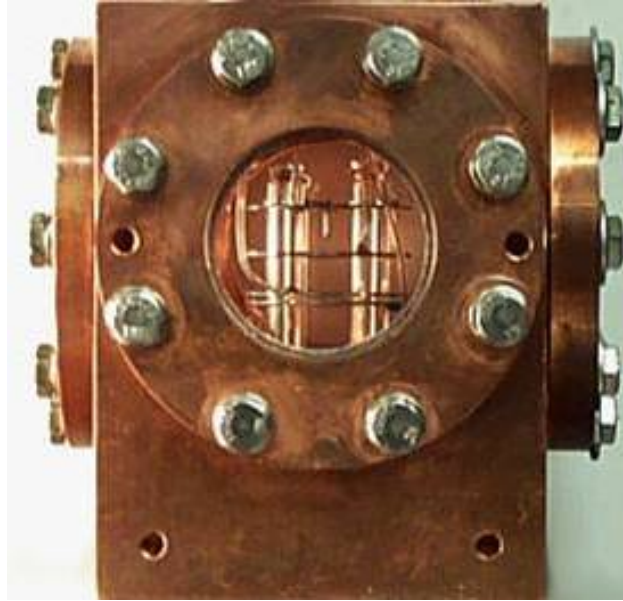


Figure 3.3: The xenon cell. It is built out of pure copper in order to obtain temperature tolerance of $\pm 0.1\text{K}$ at the setpoint.

x 5.11in copper block. Optical access is obtained from 4 viewports. The viewports are anti-reflection (AR) coated fused silica windows. The AR coating reduces back reflections of the incoming excitation laser which might result in additional background scatter in the fluorescence studies. Since the xenon cell is made of copper, all vacuum seals are made with indium wire instead of the conventional vacuum seal of a copper gasket between stainless steel conflate flanges. How to achieve good seals is explained in a paper by Lim [46]. The top and bottom seals of the liquid xenon cell are relative easy to construct following recommendations of Lim. Sealing the viewports is very challenging. According to Lim, three important factors are critical to achieve a successful window seal. (1) A machine finish of the sealing surfaces. (2) Adequate indium flow between the gaps of the sealing parts, and (3) equal compression of the indium around the circumference of the window. In addition to the recommendation of Lim, heating the window flanges is a tremendous aid in helping the indium flow between

gaps of the the window and the copper. Thus the LXe cell was placed into a homemade oven and heated to 120C as equal torque was continuously applied to the copper flanges as the xenon cell cooled back to room temperature. During the heating process, the homemade oven was pressurized with argon in order to prevent oxidation of the xenon cell. The heating process is critical when replacing old windows because it helps to smoothly combine new and old indium. When replacing windows, the xenon cell only has to be re-machined if the sealing surfaces are scratched while removing the indium from the xenon cell; this can be avoided by using a material for scraping of the indium that is harder than indium but softer than copper.

The quality of the indium seals was tested using two methods. First, the xenon cell was removed from the bigger vacuum chamber and evacuated. Then it was leak tested with a helium leak detector attached while each window, top, and bottom flange was sprayed with small amounts of helium. After no significant leak was confirmed, a high pressure test was done. This test is important because the xenon gas pressures are typically 1-2atm at the liquid xenon temperatures of this work. To perform the pressure test, the xenon cell was pumped down inside the bigger vacuum chamber. After vacuum was reached, the xenon cell was isolated and filled with argon gas while the bigger vacuum chamber was under vacuum and monitored. The test was complete once no significant change was seen in the pressure of the bigger chamber, that was at 10^{-7} Torr. When a leak detector was not available, the high pressure test alone sufficed to confirm a leak tight seal. This test can be extremely tedious because the pressure test does not reveal which window or flange leaks; also removing and installing the cell including pumping back down takes a minimum of two days. Special attention was considered when adding the argon gas in case a significant leak exists. It was added slowly as the pressure of the outer vacuum chamber was monitored in order to protect the turbo pump from a possible huge pressure increase.

In order to recirculate the LXe, a funnel was machined in the center of the bottom flange that leads to hole where an electro-polished 1/4 stainless steel tubing is welded, as shown in

Figure 3.4. The tubing extends up the side of the xenon cell to the top of flange of the LXe

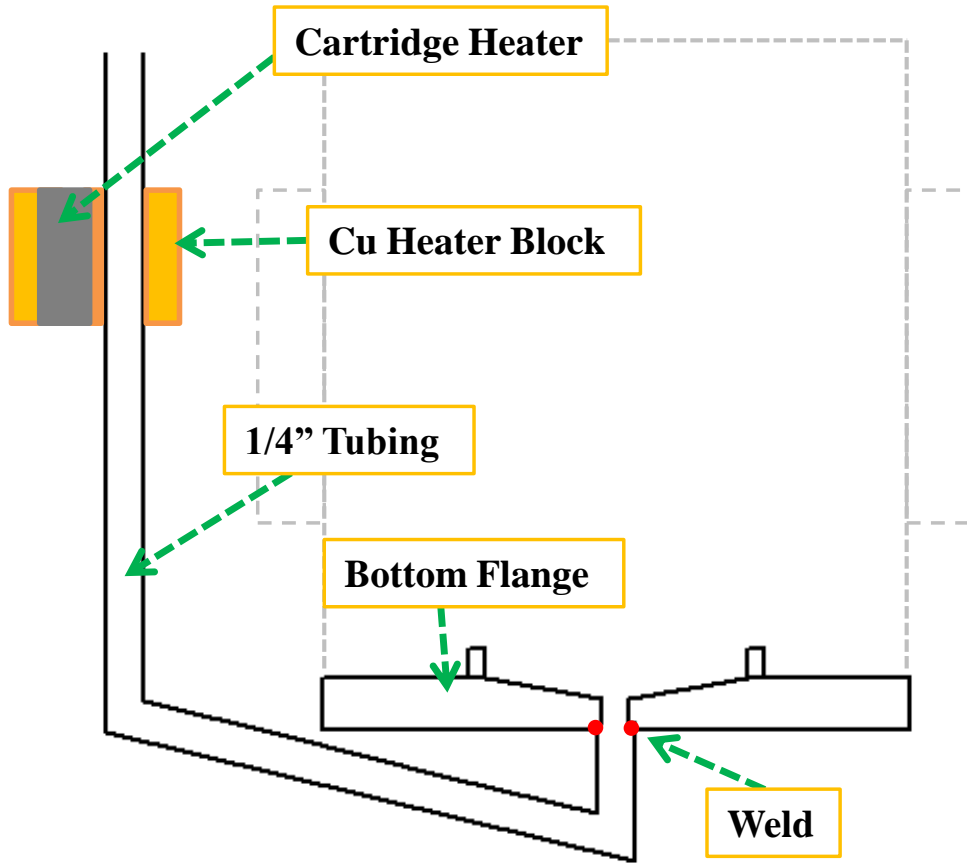


Figure 3.4: Schematic diagram of the bottom flange of the xenon cell and the recirculation tube and heater used to evaporate the liquid xenon.

apparatus. A cartridge heater is put in a small copper block to provide heat for evaporation of the liquid xenon. Indium foil is placed around the tube and cartridge heater inside the small copper block to ensure good thermal contact.

3.1.3 Cryogenics

The liquid xenon is cooled by thermal contact with liquid nitrogen cold trap that is welded inside the outer vacuum chamber as shown in Figure ?? . A thermal model excluding radiation can be found in the thesis of Jeng [47]. In order to ensure adequate heat flow to the

cold trap, a special homemade device applies a strong clamping force to attach aluminum plated copper braids to the cold trap. This device consists of a heat treated piece of thin aluminum sheet metal that is made to operate as a band clamp. For ease of use, a right angle drive is welded onto the band clamp. The other ends of the copper braids are clamped to a copper cylinder that attaches to the xenon cell. About thirty-two copper braids are used. Two braids are attached to the copper heater block that is shown in that surrounds the 1/4 tube for recirculation and cartridge heater that is shown more clearly in Figure 3.4. The xenon cell cools down to 165K in approximately 12 hours. Over time, thermal expansion and compression reduces the clamping force of the braids to the cold trap, and it takes longer to cool down the cell. Once it takes the xenon cell longer than 18 hours to cool down to 165K, the braids are retightened to the cold trap.

A LakeShore 331 temperature controller is used to stabilize the temperature of the xenon cell via a proportional-integral-derivative (PID) control loop. Two LakeShore silicon diodes measure the temperature of the xenon cell and the recirculation tube. Both are spring loaded: one onto the copper window flange of the xenon cell, and the other onto the copper block the holds the recirculation tube and cartridge heater. The temperature of sensor on the xenon cell drives the PID control loop of the temperature controller that sends current to a 25W D.C. band heater that is attached to the copper cylinder. The temperature controller can provide up to 50W. The cartridge heater that heats the liquid xenon and drives the recirculation flow is a 10W A.C. heater that is manually controlled using a Variac transformer.

A temperature stability of 0.1K at the set point is achieved if the cold trap is filled once every hour. A timer with 12 settings controls a solenoid valve that is attached to the output of a 180 liter liquid nitrogen tank to provide unmonitored filling of the cold trap. The effect of missing a fill is immediately noticed on the recirculation tube temperature sensor since there is no P.I.D to control the heater voltage. If more than one fill is missed, the cold trap has to be filled manually in between the settings of the timer in order to obtain temperature stability again.

Although a significant amount of effort went into the design and construction of the recirculation system, no further discussion of the systematic of the flow rate or how successful the recirculation system removed impurities will be given in this work. It will be discussed in the thesis of Cesar Benitez. The recirculation system was not needed or used in any of the experimental results to come. Basically, the modification to the xenon cell and the gas handling system done in this thesis work, combined with normal condensation through the commercial purifier was sufficient enough to obtain adequate liquid xenon purity in these experiments.

3.2 Ba⁺ Ion Creation

For all spectroscopy experiments in this work, Ba⁺ ions are created by laser ablation. Two different barium samples, a pure barium metal or a barium getter, are used. The barium metal sample is cut from a pure barium rod using a hack saw with a stainless steel blade. Smaller dykes and a hammer are used to mold the small piece of barium metal into a shape suitable for loading. Pure barium oxidizes quickly in air. A razor blade or a file is used to remove oxide layers prior to loading the barium metal into the xenon cell. The entire installation process is done as quickly as possible to prevent oxidation of the metal. This process typically takes 10 minutes before the system is under vacuum. A layer of oxide always exists on the pure barium metal sample once the xenon cell is back under vacuum.

The barium getter is a BaAl₄ alloy from the SAES Getters Group (ST2-FR-7X13). The getters are package in an argon atmosphere to prolong their shelf life. Speed in loading the getters is less important than for barium metal because once out of an inert atmosphere or vacuum, the oxidation process takes months according the manufacturer. The loading time for the getter material is about 1 hour because it has to be spot welded onto the target electrode. After installation of a new target, the excess barium rod and remaining getters are stored in an atmosphere of argon gas or in vacuum to prevent oxidation. Pictures of the barium samples are shown in Figure 3.5 Figure 3.5b is a image of the tip after the oxide

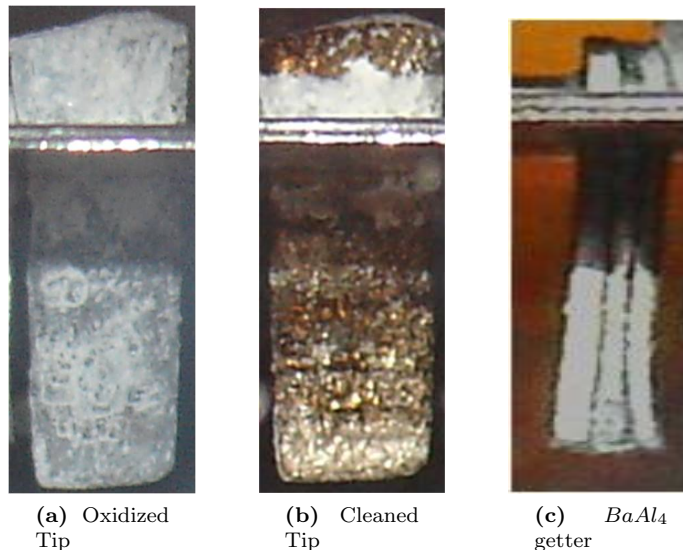


Figure 3.5: Barium metal samples: (a) barium metal after installation; (b) cleaned tip after the oxide layer has been removed via ablation; (c) $BaAl_4$ getter

layer has been blasted off using a focus pulsed laser beam.

3.2.1 Laser Ablation

Laser ablation is a common technique used to get a portion of a solid or liquid sample into the vapor phase for analysis by optical spectroscopy. An intense pulse of laser light vaporizes some surface material. The vaporized material further absorbs laser light, creating a plasma which contains free electrons, excited atoms, and ions. The overall number of atoms and ions created and the ionic charge extracted from the plasma is a function of the intensity of the laser beam. In these experiments, a focused 1064nm pulsed Quanta Ray DCR Nd:YAG laser with a pulse width of 9ns ablates the barium sample. Typically a 48cm lens was used to focus the 1064nm laser beam onto the barium sample. At the focus, the $1/e^2$ radius was measured to be $104\mu\text{m}$. With the pulsed laser operating at 1mJ of laser energy, the peak laser intensity at the focus is about $\sim 3 \times 10^8 \text{ W/cm}^2$. A laser beam of such high intensity removes more barium than desired, produces erratic amounts of ions from pulse to pulse, and eventually blasts a hole through the barium sample. Consistent ion charge, pulse to

pulse, was achieved by increasing the laser spot size on the sample by focusing the laser beam beyond the sample. The laser beam was usually focused 5cm behind the barium tip with a laser beam radius of approximately 0.05cm. The reduced laser intensity of $\sim 1.5 \times 10^7$ W/cm² produced a controlled number of extracted barium ions that was in the range of 10^6 to 10^7 with about 25 percent fluctuation from pulse to pulse. The laser ablation process takes place in 1-2atm of xenon gas above the liquid, and the ions are drawn into the liquid with an electric field.

3.2.2 Ba⁺ ion detection

A picture of the the electrode system used to pull the ions into the liquid is shown in Figure 3.6. The electrodes are made out of 304 stainless steel sheet metal. The diameter of

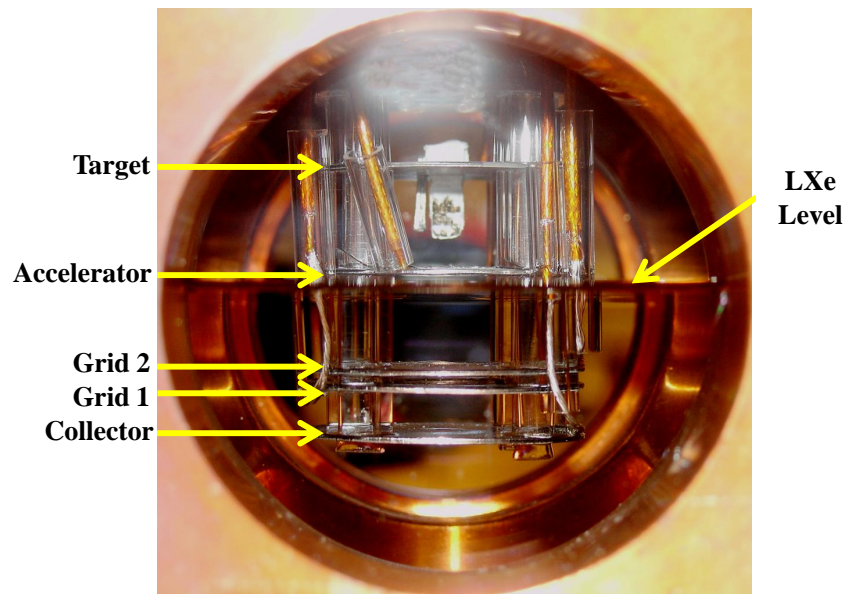


Figure 3.6: Picture of the electrodes and the mesh grids.

each of the electrode is 28.8mm and the thickness is 0.635mm. The electrodes are mounted inside the liquid xenon with from an aluminum rod attached 32 inches above the cell. From

top to bottom, the electrodes are labeled target (T), accelerator (A), grid2 (G2), grid1 (G1), and collector (C). The spacing between the electrodes is 14mm, 8mm, 1mm, and 4mm respectively. The electrodes are separated and electrically isolated with quartz tubes. Electric fields between the plates are generated from the voltages applied through ultra high vacuum coaxial cables that are soldered onto each electrode. The coaxial cable helps to eliminate electrical pickup from cables passing close to one another. The 8mm gap between the A and G2 electrodes defines the drift region. The ions are collected on the G1 electrode which is grounded through its connection to a Keithley 610C electrometer that measures the ion current. In the work the collector is ground, and is no used. A 10.6mm hole is punched into the center of A, G2, and G1 electrodes, and a mesh grid is soldered onto the electrodes covering each hole. The mesh grid consists of perpendicularly space wires with thickness of $46\mu m$ and spacing of $850\mu m$. The mesh grid shields the G1 electrode from induced current signals until the ions have traveled through the grid on G2. In order to pull 100% of the ions through the mesh grids, the electric field in the drift region is 3 times bigger than that in the region between the T-A, and 3 times less than that in the region between G2-G1. A calculation showing 100% charge transparency through a mesh grid which such a field ratio is given by Bunemann [48]. The geometry of our grids is somewhat different than the model of Bunemann, and the grid transparency ratio was determined experimentally. A SIMION simulation of the path the ions and the equipotential contours of the electrode setup is shown in Figure 3.7

The electrometer reads the ion current on G1. A typical electrometer raw signal is shown in Figure 3.8. The sharp rise at $t=0$ is due to photoelectrons created on G1 at the time of ablation from the intense plasma emission light, and marks the time of the ablation laser pulse. Due to the long time integration constant of the input circuit of the electrometer, a correction procedure was used to determine the true current from the output voltage of the electrometer. A equivalent circuit diagram of the electrometer is shown in Figure 3.9 Kirchhoff's rules give the following equations:

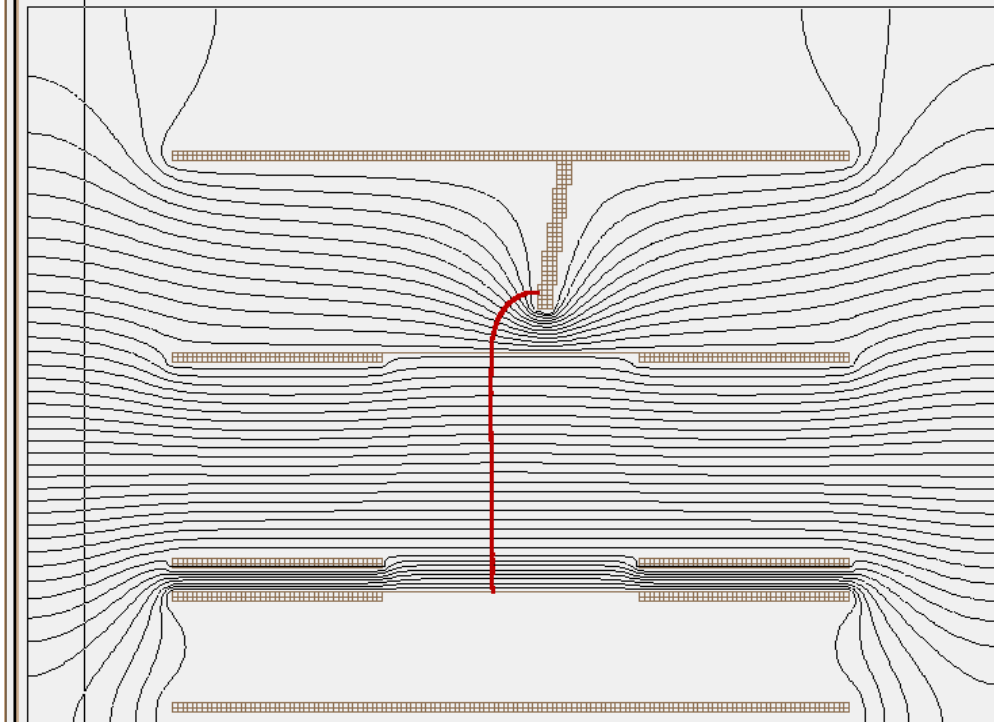


Figure 3.7: The equipotential contours and the expected Ba^+ ion path to the C electrode.

$$I = I_1 + I_2 \quad (3.1)$$

$$V = M \times V_1 \quad (3.2)$$

$$V_1 = -\frac{q_2}{C} = -I_1(t)R_1 \quad (3.3)$$

Solving these equations, the current, $I(t)$ is,

$$I(t) = -\frac{1}{R_1 M} \left(V + R_1 C \frac{dV}{dt} \right) \quad (3.4)$$

The resistance, R_1 , is given in the manual of the electrometer, and it depends on the amperage scale setting of the electrometer. For the experiments in liquid xenon the scale was typically set to $0.1 \times 10^{-10} \text{A}$, where R_1 is $10^{10} \Omega$. The multiplication factor M and effective capacitance C , are determined by calibrating the electrometer with a square wave input, V_{square} , through a large resistor, $R = 2.2 \times 10^9$. With the added resistor, the equivalent

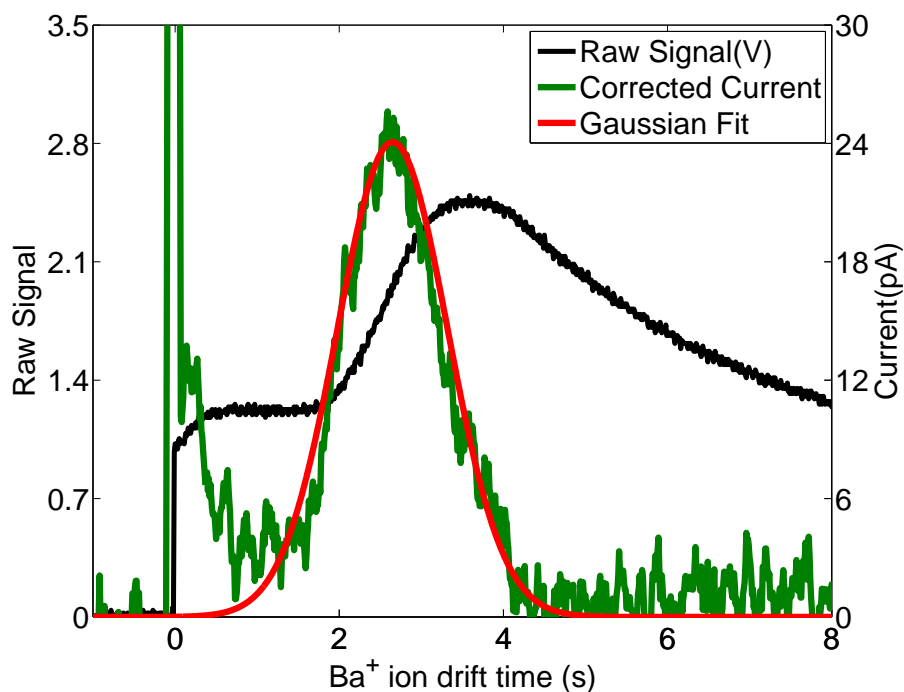


Figure 3.8: Sample of the inverse raw voltage signal from the electrometer, the derived Ba^+ current signal and a Gaussian fit to the current used to determine the Ba^+ ion charge

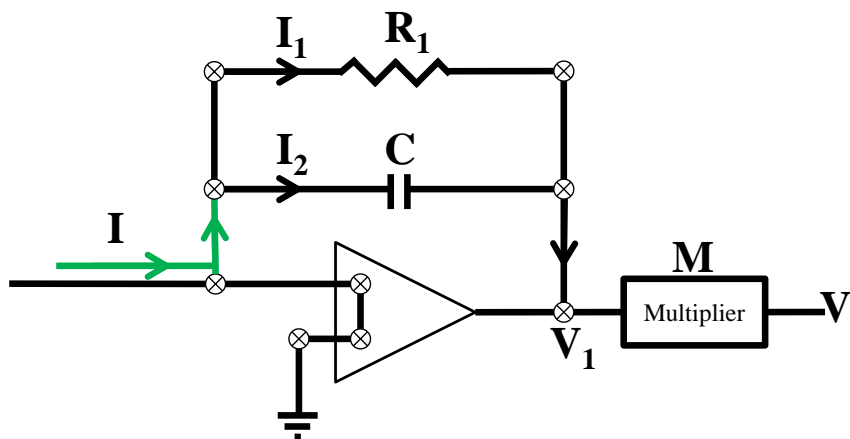


Figure 3.9: Equivalent Ba^+ ion current detection circuit

circuit is shown in Fig. 3.10, with the following additional Kirchhoff equation:

$$V_{square} - I(t)R = 0 \tag{3.5}$$

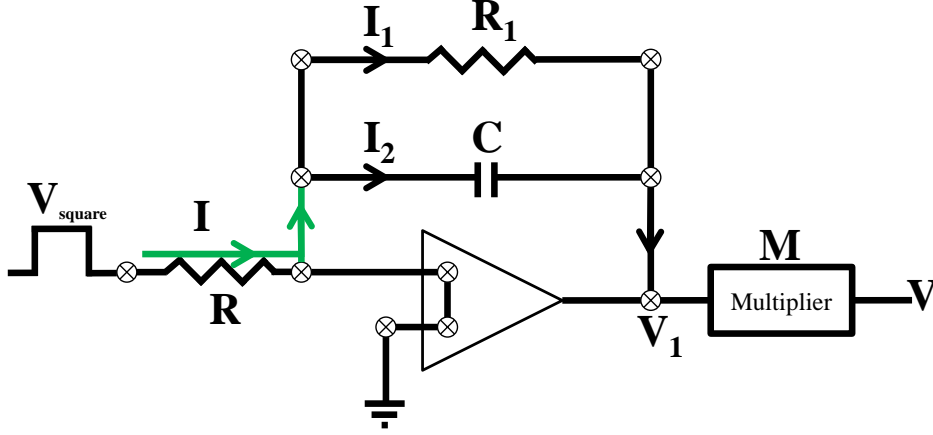


Figure 3.10: Electrometer calibration circuit

Equation 3.4 becomes

$$V_{square} = -\frac{R}{R_1 M} \left(V + \tau_{eff} \frac{dV}{dt} \right) \quad (3.6)$$

where $\tau_{eff} = R_1 C$ is the effective time constant. The output, V from the electrometer is inserted in Equation 3.6, and M and τ_{eff} are then adjusted until the calculation input V_{square} matches the actual square wave input. The best fit is determined when $\tau_{eff} = 4.2s$ and $M=26$. Thus the actual current signal is obtained from the following equation:

$$I(t) = -3.8 \times 10^{-12} \left(V(t) + 4.2 \frac{dV(t)}{dt} \right) \quad (3.7)$$

A sample corrected ion current is shown in Figure 3.8. A Gaussian fit is typically made to the corrected current and then integrated to determine the charge.

The ablation process and the current analysis are fully automated using a Labview program. A TTL signal generated from a Labview digital I/O box sends a trigger to the Nd:YAG laser to fire. Some of the reflected laser light is monitored by a photodiode and used to trigger the oscilloscope to begin a sweep. After a preset oscilloscope scan time, in which all the ions have reached G2, the Labview program stops the scope, grabs the trace, and performs the calculation of $I(t)$, from Equation 3.7, using the appropriate constants. Labview then fits a Gaussian, and integrates it to determine the amount of charge in the ion

bunch. A Coherent FieldMax TOP power/energy meter with either a J-25MB or J-25MB-E power head measures the energy of the Nd:YAG laser each shot, and it is recorded by the same Labview program. The Labview program stores the raw signals from the measurement devices, triggers, and relevant calculations from the equations above for each ablation shot along with temperature information from the Lakeshore temperature controller and any additional timing information needed from the experiments.

3.3 Liquid Xenon Purity Monitor

Since the barium metal tip is partially oxidized, the laser ablation process could introduce O_2 into the liquid xenon. The O_2 could react with the Ba^+ ions in the liquid and cause reduction in the fluorescence of the Ba^+ ions. Therefore it is desirable to have a monitor to measure the liquid xenon purity.

The concentration of electronegative impurities is obtained by measuring the survival rate of electrons drifting through the liquid xenon. The reaction is given by



where S is an electronegative impurity. The time rate of change of the total number of electrons n_e is given by

$$\frac{dn_e}{dt} = -k_S n_e n_S \quad (3.9)$$

where k_S is the attachment rate coefficient, which depends on the electric field of the drift region and n_S is the concentration of impurities. Solving equation 3.9 gives

$$n_e = n_0 e^{-\frac{t}{\tau}} \quad (3.10)$$

$$\tau \equiv \frac{1}{kn_S} \quad (3.11)$$

The electron lifetime, τ , is calculated from the ratio n_e/n_0 . The oxygen-equivalent impurity concentration, n_S , can be calculated using the measurements of the rate constant, k , at different drift fields provided by Bakale [49].

3.3.1 ICARUS Liquid Xenon Purity Monitor

The CSU liquid xenon purity monitor (LXPM) is based upon the design of a liquid argon purity monitor by the ICARUS collaboration [50]. A diagram of the ICARUS purity monitor

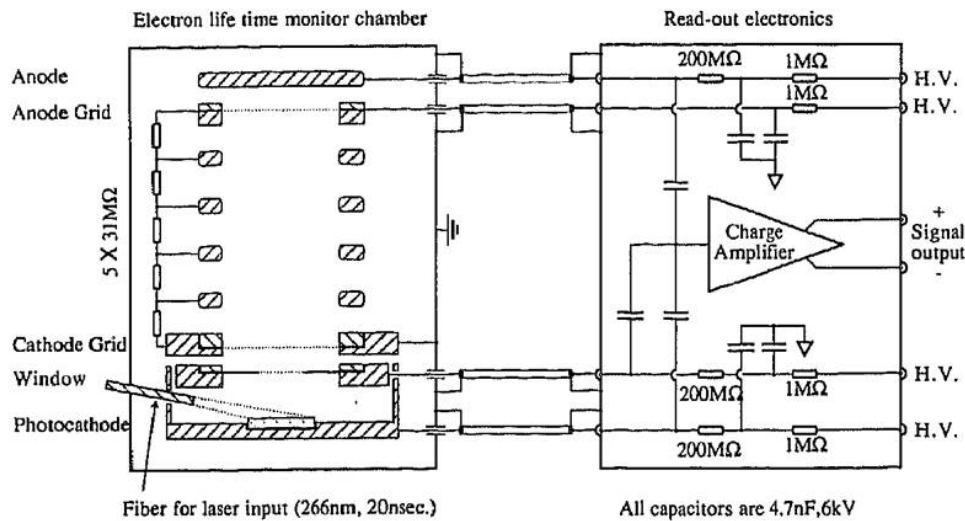


Figure 3.11: Electron creation and the electronics setup for ICARUS purity monitor. Reprinted from Nuclear Instruments and Methods in Physics Research Section A: Accelerators, Spectrometers, Detectors and Associated Equipment, 329, Benetti P et.al. , A simple and effective purifier for liquid xenon, 361-364, Copyright (1993), with permission from Elsevier

is shown in Figure 3.11. A fiber directs 266nm wavelength light, that is generated from the 4th harmonic of a pulsed Nd:YAG laser, toward a stainless steel cathode plate that is gold plated only in the center. Photo-electrons are emitted from the gold via the photoelectric effect. The fiber is inserted inside a cylinder in which the inside walls are coated with Cr_2O_3 in order to absorb any reflected or scattered 266nm laser light. At the top of the cylinder a grid at 100V bias pulls the electrons to the anode. The drift region, between the anode and cathode grid, is 50cm. Between the anode and cathode grids, field shaping rings with

create a uniform electric potential. The photocathode and window grid are coupled together so that the measured initial electron signal includes only electrons that are pulled through the window grid. This eliminates photoelectrons from reflections, for example. The final electron signal is measured at the anode. The anode, photocathode, and window grid are all capacitively coupled into a single charge sensitive preamplifier. Since the initial and final pulses are well separated in time, the transmission ration n_e/n_o can be obtained without calibration of separate preamps.

3.3.2 CSU Liquid Xenon Purity Monitor

The CSU LXPM is a little different than ICARUS design. The notable differences are:

1. A shorter drift region with no field shaping rings
2. Separate electrode signal readout
3. A different method of electron creation

The electrode setup is different because the purity monitor must use the electrode setup for the laser spectroscopy experiments. The ICARUS design is also a closed system with no optical access. A schematic diagram for the electrical setup and beam alignment for the purity measurements is shown in Figure 3.12. No electrons drift in the 14mm distance between the accelerator and target electrode because the voltages on these two electrodes are set to be the same. Because the signals on different electrodes are not fully separated in time, each electrode is connected to a separate charge sensitive preamplifier. The preamps are model eV-5092 made by Endicott Interconnect Technologies, Inc. Each preamp chip is installed in an eV-505 preamplifier box. One can easily swap to a different eV-509x preamp chip if different sensitivities are needed or if one is blown out. The high voltage to each electrode is fed through the preamps. The electrons are generated by multiphoton ionization between C and G1, and the drift region is between G2 and A.

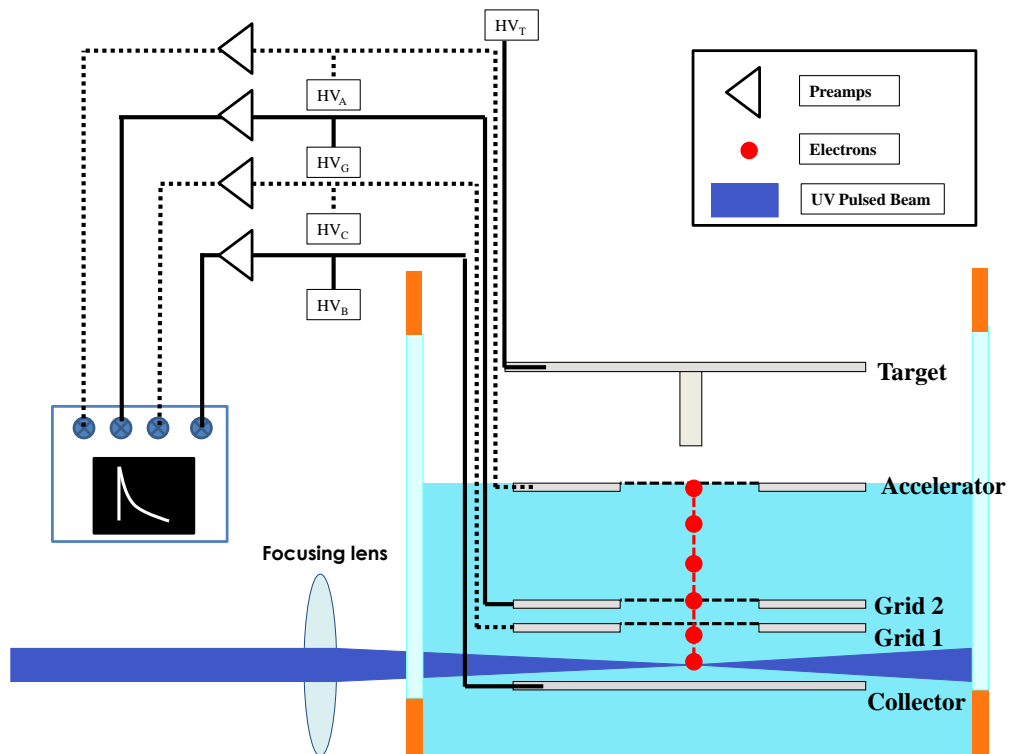


Figure 3.12: Electrical connections for the LXPM. Also shown is the focused laser between the plates that generates the electrons by ionizing the liquid xenon

Detailed measurements of the liquid xenon purity with the LXPM were made under many conditions. A more in depth analysis of those measurements and the operation of the LXPM will be discussed in a future thesis. After initial condensation, the concentration of oxygen equivalent impurities in the liquid xenon was always than 4 parts per billion (ppb). The most important measurement made with the LXPM purity monitor to this thesis work is that laser ablation of the oxidized barium metal had no effect on the purity of the liquid xenon. An unexpected discovery of the CSU LXPM was that electrons can be produced via nonresonant multi-photon ionization of the liquid xenon. We discovered this by noting that electrons were still created abundantly when the photoelectron producing laser was not hitting the electrodes. Given the compactness of our LXPM, a well-defined localized source of electron was vital for making accurate purity measurements.

3.4 Nonresonant Multiphoton Ionization of LXe

Detailed studies of nonresonant multiphoton ionization (NRMPI) of the liquid xenon were carried out by focusing a pulsed laser beam between two electrodes and measuring the electron charge generated with preamps connected to the electrodes. Attenuators were used to vary the laser pulse energy. The pulsed laser beam was focused in the middle between electrodes A and G2 or G1 and C (Figure 3.12). Four wavelengths were used to study the NRMPI process in LXe: 221nm, 266nm, 280nm and 355nm. The 355nm and 266nm wavelengths are the third and fourth harmonic of a Nd:YAG Quanta Ray pulse laser. The 280nm and 221nm are generated from a Quanta Ray PDL-2 pulse laser system that is pumped by the second harmonic (532nm) of the Nd:YAG laser and then doubled or mixed in a Quanta Ray WEX-1 Pulse Dye Laser Frequency Doubler (WEX). To get the 280nm wavelength, 560nm is first generated in the dye laser. A doubling crystal inside the WEX is used to generate 280nm light. The 221nm pulse was generated in the WEX by the sum frequency mixing of 280nm beam with the 1064nm beam from the Nd:YAG. In initial experiments, the laser energy was measured before all the attenuators and fluctuations in the laser energy

were recorded. An attenuation factor of 89%, 85%, 85% and 83% per attenuator, for 355nm, 280nm, 266nm, and 221nm, respectively, was measured. The error in the measurements are the same for all wavelengths, $\pm 1\%$. For improved accuracy, especially for the cross section measurements, the laser pulse energy was measured after being attenuated for 266nm and 355nm. This improvement could not be done for the 221nm and 280nm wavelengths because the laser pulse energy was too low to measure.

As derive in Section 2.2, the total number of atoms ionized in the intensity region, N_{e^-} , is given by

$$N_{ions} = N_{e^-} = n_o \sigma^{(n)} \tau_n V_n \left(\frac{\epsilon}{E_p \tau_n A_o} \right)^n. \quad (3.12)$$

where

$$V_n \equiv \int_v [F(\vec{\mathbf{r}})]^n dV \quad (3.13)$$

$$\tau_n \equiv \int_{-\infty}^{\infty} [G(t)]^n dt \quad (3.14)$$

are the effective interaction volume and time respectively, n_o is the neutral atom density, E_p is the energy of the laser photon, and $\sigma^{(n)}$, is the ionization cross section, ϵ is the laser pulse energy, and E_p is the photon energy of the laser. A typical raw signal from the preamplifier is shown in Figure 3.13. The peak preamp output, s , is related to N_e by the

$$N_e = \frac{s}{\beta e^-} \quad (3.15)$$

where $\beta=0.2$ mV/fC is the sensitivity factor of the preamplifier, and e^- is the charge of an electron. Substituting Equation 3.15 into Equation 3.12 and solving for, s , gives

$$s = \beta e^- n_o \sigma_n \tau_n V_n \left(\frac{\epsilon}{E_p \tau_n A_o} \right)^n \quad (3.16)$$

The experiments were performed at approximately 168K. The liquid xenon density at this temperature is 3.057 g/cm³, so $n_o = 1.33 * 10^{-12}$ atoms/cm³. The interaction time, τ_n , is

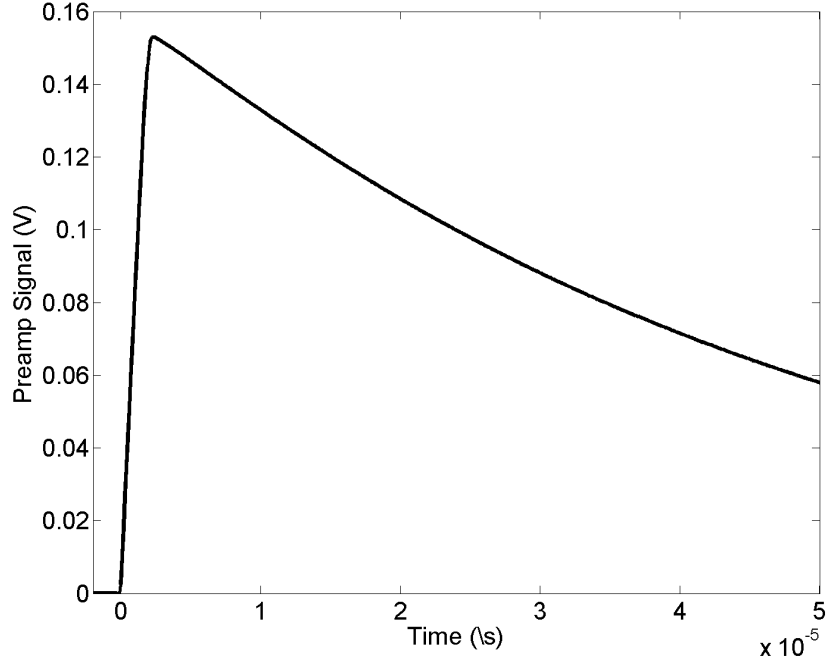


Figure 3.13: Typical raw signal from the preamplifier attached to the accelerator electrode. The peak of the signal is proportional to the number electrons according to Equation 3.15

the FWHM of the pulse width. By definition, $F(\vec{r})$ is a dimensionless shape factor that is normalized by the max laser intensity at the center of the laser beam, it is represented by

$$F(0, z) = \frac{I(0, z)}{I(0, 0)} = \frac{\epsilon(z)/(A(z)\tau)}{\epsilon(0)/(A(0)\tau)} \quad (3.17)$$

Conservation of energy requires the measurement of $\epsilon(z)$ at any point along z to be the same in a loss-less medium, therefore $\epsilon(z) = \epsilon(0)$ and

$$F(r, z) = \frac{A(0)}{A(z)} \quad (3.18)$$

where $A(z) = \pi w^2(z)/4$. Since $dV = A(z)dz$, the interaction volume, V_n , becomes

$$V_n = \int \left(\frac{A(0)}{A(z)} \right)^n A(z) dz \quad (3.19)$$

To simplify things $K_n \equiv V_n/A_o^n$, thus

$$K_n \equiv \int S_n(z) dz \quad (3.20)$$

where

$$S_n(z) \equiv [\pi w^2(z)]^{1-n} \quad (3.21)$$

Equation 3.12 then beomes

$$s = C_n \tau_n^{1-n} K_n \sigma_n \epsilon^n \quad (3.22)$$

with

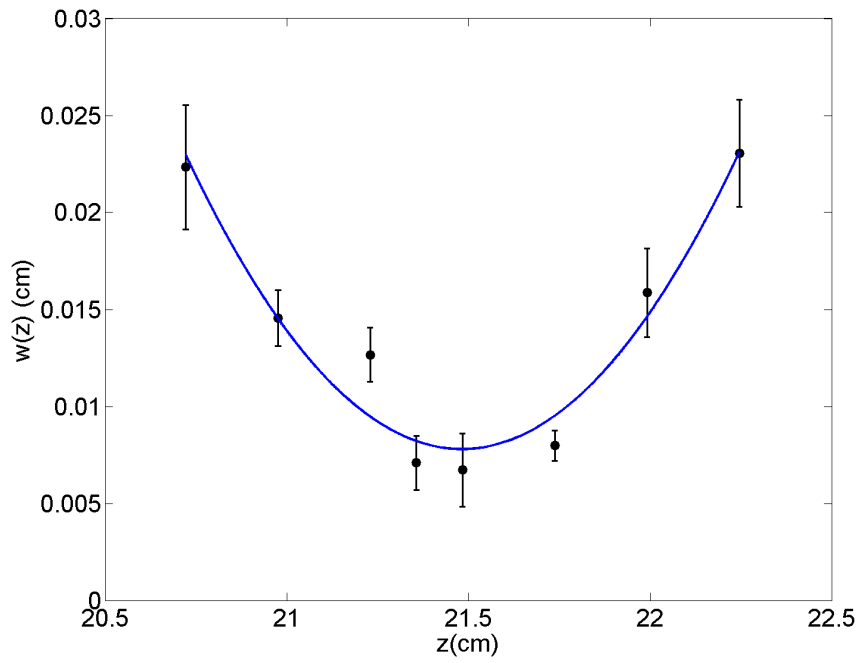
$$C_n \equiv \frac{\beta e^- N_o}{E_p^n} \quad (3.23)$$

The $1/e^2$ beam radius, $w(z)$, was determined from a knife edge beam profile at different z positions along the propagation path of the focused beam. Plots of the beam radius for 266nm and 355nm are given in Figure 3.14. The laser energy for 280nm and 221nm was too low to measure the beam radius with the knife edge technique. The same 20cm focal length lens was used to focus all wavelengths between the electrodes. Plots of $S_n(z)$ for 266nm and 355nm, assuming these are $n = 2$ and $n = 3$ photon processes respectively are given in Figure 3.15. The value of K_n is determined from the integration of $S_n(z)$ using the trapezoidal rule. The parameters C_n , τ_n , and K_n , for these two wavelengths are summarized in Table 3.1. From the plots of $S_n(z)$ it can be seen that the length of the interaction volume

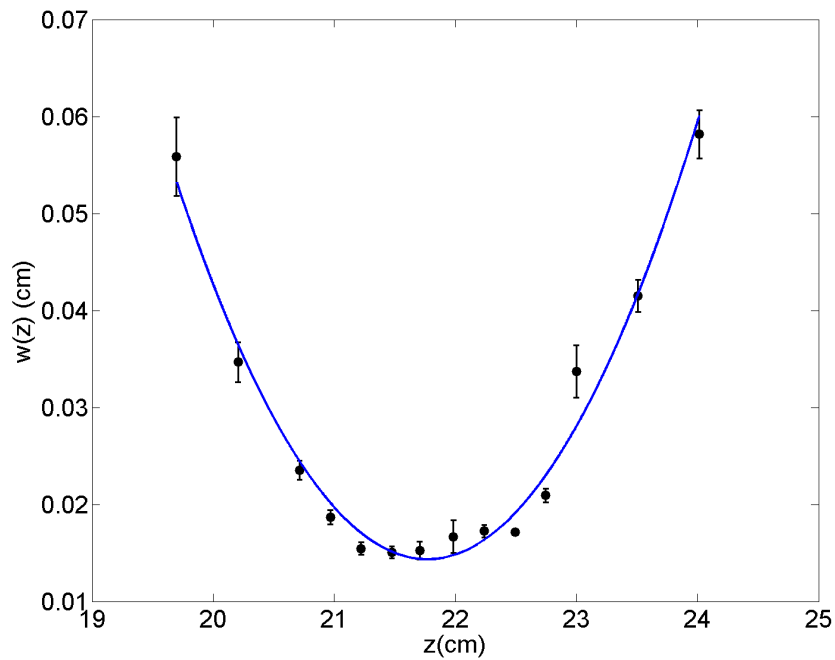
$\lambda(nm)$	n	$C_n(atoms * V/cm^3/J^n)$	$\tau_n(s)$	$K_n(cm^{3-2n})$
266	2	7.63×10^{50}	$(4.50 \pm 0.5) \times 10^{-9}$	$(4.65 \pm 1.28) \times 10^3$
355	3	2.42×10^{69}	$(5.50 \pm 0.5) \times 10^{-9}$	$(2.90 \pm 0.31) \times 10^6$

Table 3.1: Laser beam and liquid xenon parameters

is on the order of 2cm, and is well within the diameter of the electrodes of 2.8cm. Generation

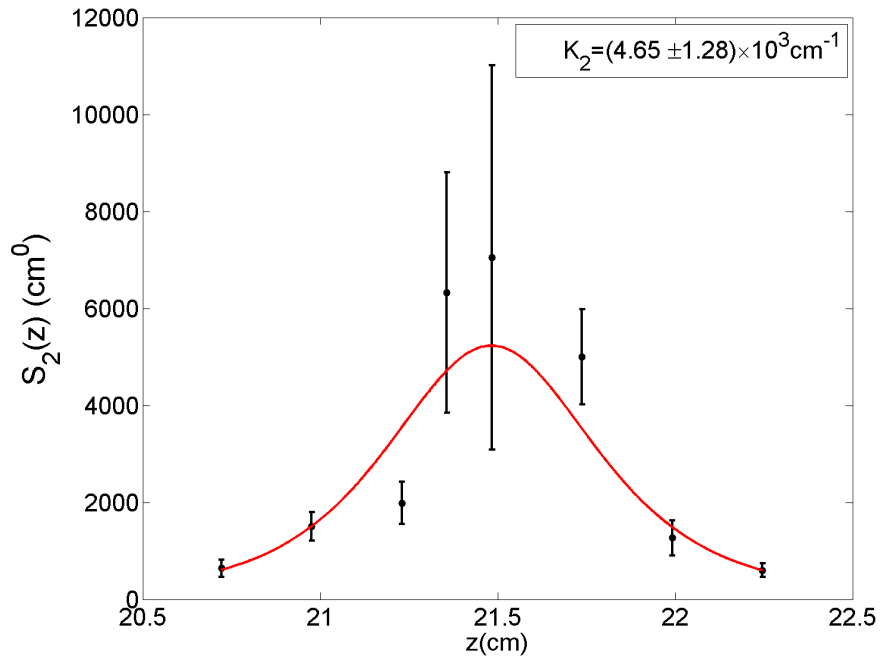


(a) 266nm

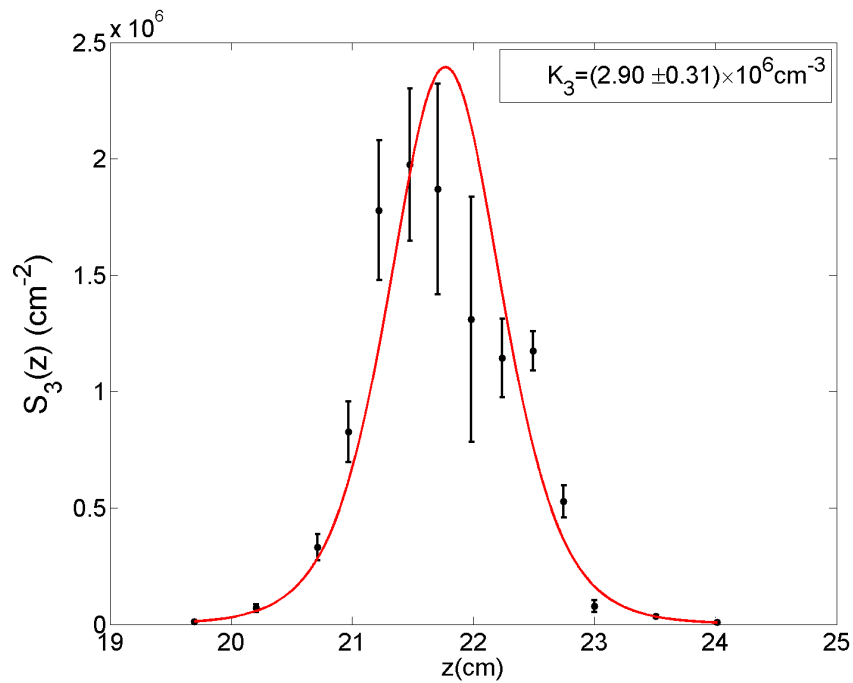


(b) 355nm

Figure 3.14: Laser beam radius, $w(z)$, from knife edge profiles for 266nm and 355nm after focusing with a 20cm UV lens.



(a) 266nm



(b) 355nm

Figure 3.15: The effective volume function, $S_n(z)$, for 266nm and 355nm. K_n , determined by integration using the trapezoidal rule, is given in the inset.

of the electrons between the electrodes is important to ensure that all the electrons from the ionization process are collected.

Since only the electrons moving to the electrodes are measured to determine the NRMPI signal, any loss of electrons in the drift region could affect the results of the measurement. Of particular concern are electron recombination with the xenon holes and electron attachment to impurities in the liquid xenon. The electron lifetime determined by the LXe purity monitor for an O_2 equivalent impurity was ~ 2.6 ms. As shown in Figure 3.13, the drift time of the electrons are on the order of μ s. Thus, electrons attaching to impurities in the liquid xenon are neglected. The density of electron-hole pairs and the drift electric field are two factors

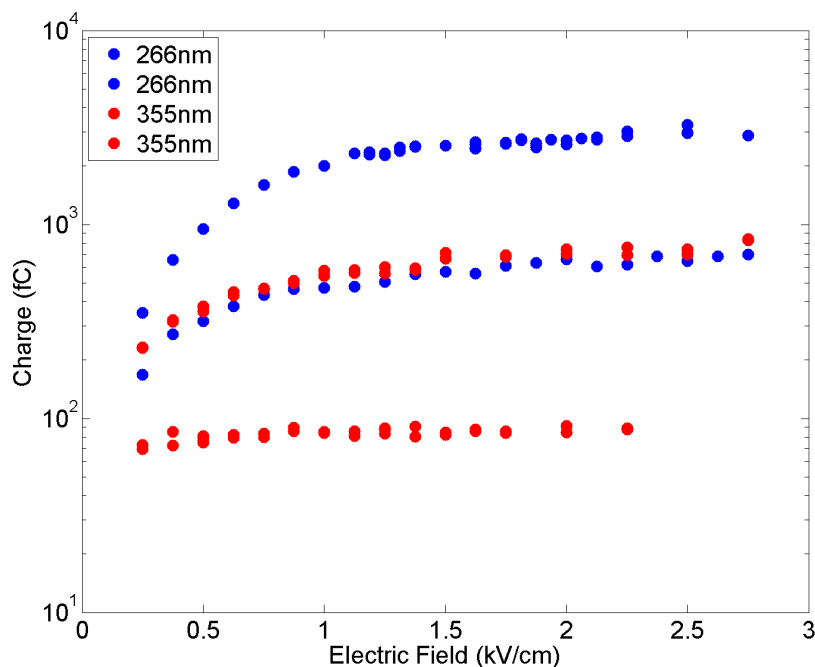


Figure 3.16: Recombination plot for the 355nm focused beam. The plots show that the effect of electron recombination levels off after 1kV/cm. The highest and lowest charge density for measurements made with 266nm and 355nm are shown.

that determine if electrons will recombine. Greater recombination is expected for regions of higher charge ionization density and lower drift electric fields. To prevent recombination, the electrons must be pulled away from the xenon holes before the electrons can recombine. The effect of electron recombination is observed by measuring the collected charge at different

electric fields in the electron drift region. The total charge collected vs. the electric field is shown in Figure 3.16. The highest and lowest charge density for measurements made with 266nm and 355nm are shown. Each point on the plot is an average of 320 laser pulses. Collected charge for the lowest charge density with 355nm is approximately independent of the electric fields. For the higher charge, collected charge levels out at electric fields higher than 1kV/cm. In order to be sure that recombination is minimized, all n values and cross section measurements are performed at the highest drift field.

3.5 Spectroscopy

Figure 3.17 is a schematic diagram of the spectroscopy setup. As mentioned previously, a

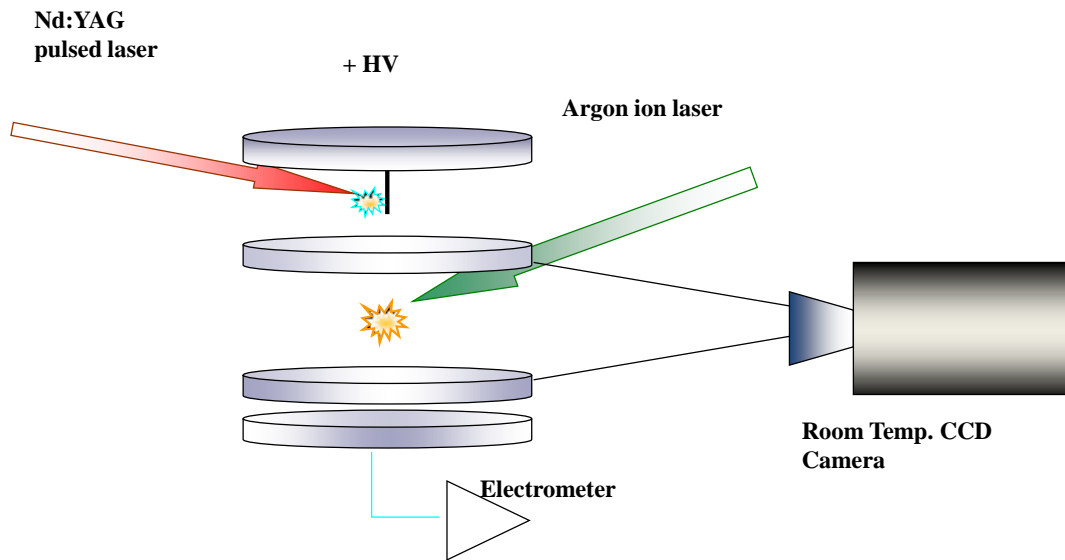


Figure 3.17: Schematic diagram of the spectroscopy setup showing rooming temperature camera used to monitor the experiment

single pulse experiment begins with the laser ablation of the barium metal sample, shown by the red arrow. As the Ba^+ ions are drawn into the liquid xenon, they pass through an argon ion laser beam (green arrow) that is aligned parallel to the accelerator and grid 2 electrodes.

The argon laser is expected to excite the ions. The laser is an LEXEL Model 95-4 argon ion laser with maximum output power of 4 Watts while lasing in the all lines mode. An inter-cavity prism allows the laser to operate at the individual argon ion transitions wavelengths of: 454.5nm, 457.9nm, 465.8nm, 472.7nm, 476.5nm, 488.0nm, 495.5nm, 501.7nm, and 514.5nm. The argon laser is aligned anti-parallel to the Nd:YAG ablation laser and enters the xenon cell from the opposite viewport.

The room temperature video camera in Figure 3.17 displays the entire experimental region. It is a Watec WAT-902HS camera, with a 50mm camera focus lens, and serves as a visual aid during the fluorescence experiments. The video camera output is always recorded during the fluorescence experiments using Ulead multimedia products. A frame taken from

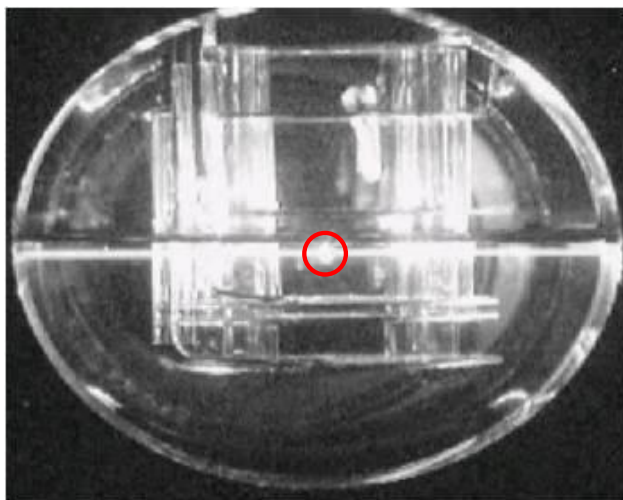


Figure 3.18: Frame from the video camera taken during fluorescence experiments. The white beam of light is Rayleigh and Brillouin scattering of the argon laser.

the camera after the ablation is shown in Figure 3.18. The electrodes and sample tip can be seen in the photo, and the bright line is the Rayleigh and Brillouin scatter from the argon laser. No filter is put in front of the video camera to block any scattered light. Thus it is unknown if the flash is due to the emission from the excited Ba^+ ions or particles scattering at the excitation laser wavelength. Understanding the source of the flash is a major topic of this thesis.

Although, the room temperature video camera is a fairly sensitive CCD and gives a good real time view of the experiment, it is neither quantitative nor sensitive enough to see the low light levels expected from the Ba^+ ions fluorescence. The low light detection setup for quantitative analysis is located at the window opposite to the video camera. The laser focal region is focused through a Raman filter into a spectrometer, whose output is imaged onto LN_2 -cooled CCD camera as shown in Figure 3.19. The spectrometer is an Acton: Spectro Pro

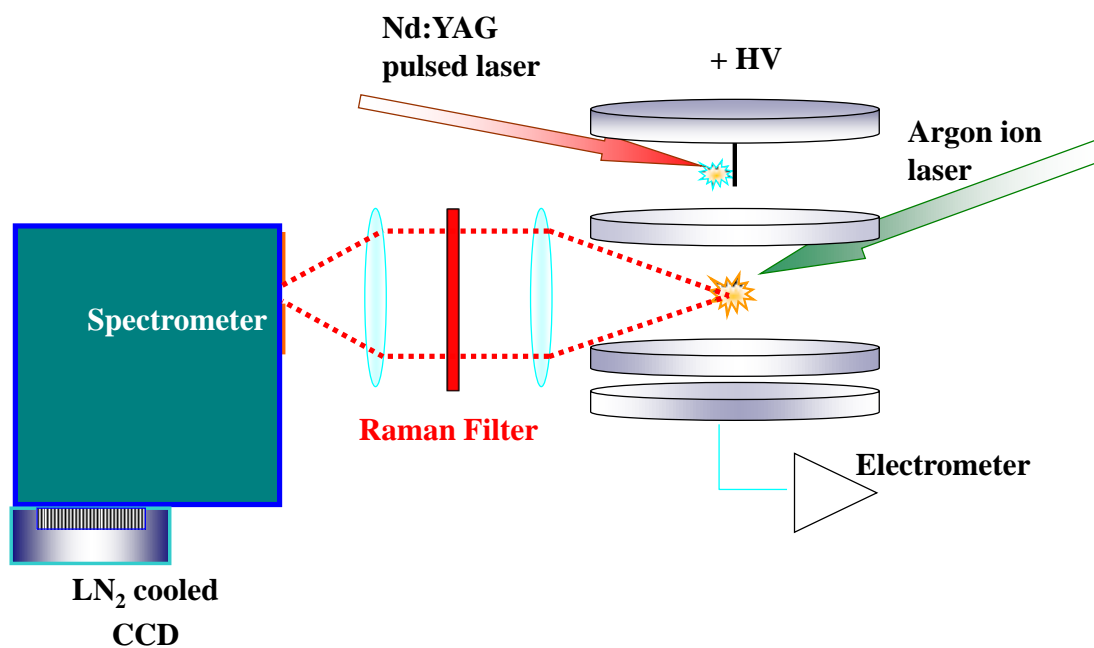
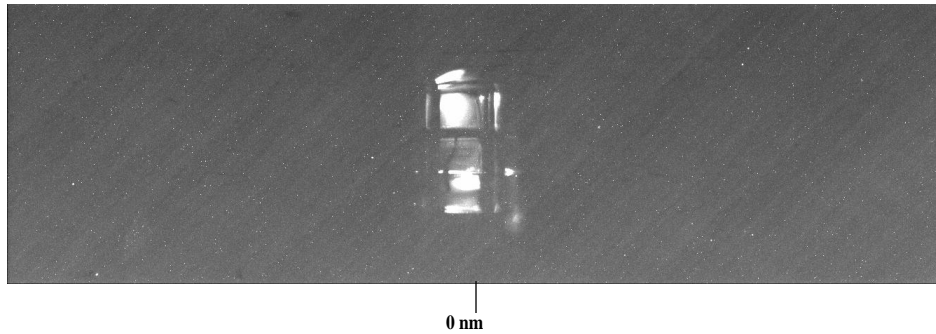


Figure 3.19: Low light setup for fluorescence experiments.

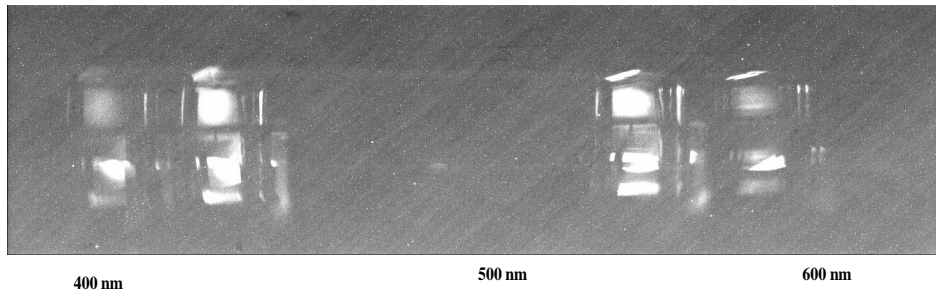
2150i dual grating imaging spectrograph, with a focal length of 150 mm. The spectrometer contains two gratings, 300 lines per millimeter (1/mm) and a 600 l/mm, both with a blaze wavelength of 500nm. Changing gratings takes only seconds and has minimal effect on what is imaged onto the LN_2 -cooled CCD . Thus it is easy to switch between the two gratings during experiments. The maximum resolution of the spectrometer is quoted only for 1200 l/mm grating as ± 0.25 nm. The spectrometer is has f/4 angular acceptance. The second lens in Figure 3.19 is a 50mm Nikon lens that mounts directly onto the spectrometer and focuses the light onto a bilateral adjustable slit that is 10-300 micron wide and 14mm high. The

LN₂-cooled CCD camera is a Roper Scientific SPEC 10: 400B camera with extremely low noise. When the camera is cooled down to -120C, the dark electron rate is 0.3 e-/pixel/hour with a typical readout noise of 3.5 e-RMS per pixel. The LN₂-cooled CCD array is 1340 by 400 pixels; each pixel is 20 by 20 microns. WinSpec software is used to acquire images and spectra.

In imaging mode, each pixel of the LN₂-cooled CCD array is individually read out to record and display an image. The inside of the experimental region illuminated by a mercury lamp is shown in Figure 3.20. When the spectrometer is set for 0th order diffraction,



(a) Spectrometer grating set to 0th order in which it reflects the light like a mirror



(b) Spectrometer grating set to 1st order diffraction

Figure 3.20: Pictures of the experimental region illuminated with a Hg lamp to show the convenient imaging mode of the LN₂-cooled CCD camera.

the gratings behave as mirrors (Figure 3.20a). When the spectrometer is set to 1st order diffraction, multiple images representing the different mercury wavelengths are displayed (Figure 3.20a).

3.5.1 Fluorescence Spectra setup

For the fluorescence experiments, light from the laser beam region is collected by a 10cm focal length lens that makes the light parallel. The parallel light passes through the 50mm Nikon camera lens, which is set to infinity. Figure 3.21 is an image taken with the LN₂-

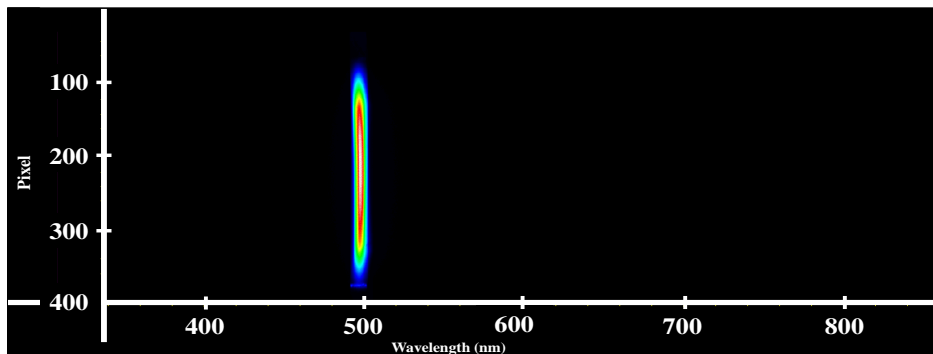


Figure 3.21: This is a spectrum of the excitation laser taken with the LN₂-cooled CCD in imaging mode at very low laser power. The Rayleigh and Brillouin scatter makes it easy to image the beam onto the LN₂-cooled CCD .

cooled CCD with very low argon laser power and with the f/16 setting on the camera lens to prevent saturation of the pixels. The light seen in the picture is the intensity distribution of the Rayleigh and Brillouin scatter in the liquid xenon from the excitation laser. The laser beam region, where the Rayleigh and Brillouin scattering originates is the only region imaged onto the LN₂-cooled CCD . All other light from the experimental region is blocked using the slit of the spectrometer and razor blades that were externally mounted onto the slit fixture. The photo demonstrates the convenience of the imaging mode of the LN₂-cooled CCD. It ensures correct alignment of the laser beam region through the slit to limit the height of the slit. The width of the excitation beam can be determined from images such as these for each fluorescence experiment.

After satisfactory alignment, the excitation laser power is increased and the LN₂-cooled CCD is set to spectroscopy mode to observe the fluorescence. In spectroscopy mode all or a specified subset of the vertical pixels are binned as one, thus decreasing the readout noise by a factor of up to $\sqrt{400}$. The Rayleigh-Brillouin scatter is so intense that it would

saturate the LN₂-cooled CCD , and some of the charge would bleed onto the neighboring pixels if unfiltered. A Raman edge filter is used to attenuate the Rayleigh-Brillion scatter in the liquid. It has a very steep transmission and cutoff edge with attenuation of greater than OD6 below the cutoff wavelength and transmission greater than 98% above the cutoff. Raman filters can be rotated to cut off at lower wavelengths according

$$\lambda(\theta) = \lambda(\theta = 0^\circ) \sqrt{1 - \frac{\sin^2 \theta}{n_{eff}^2}} \quad (3.24)$$

where n_{eff} is the effective index of refraction. A 514nm Semrock Raman edge filter is used in the fluorescence experiments. Rotating is useful when wavelengths lower than the filter cutoff at $\theta = 0^\circ$ are used to excite the Ba⁺ ions because light from the fluorescence spectrum lower than the cutoff will not be blocked.

3.5.2 Plasma Emission Setup

The plasma emission spectrum is used to identify the atomic species that exist in the plasma and to help determine the species responsible for the observed ion current and the fluorescence spectrum. A schematic diagram of the setup for the plasma emission experiments is shown in Figure 3.22. The ablation plasma region is imaged onto the slit of the spectrometer with just the 50mm Nikon lens. Three mirrors are used to image the front laser ablation of the barium sample. The green line is the path of the ablation laser and the red line represents that of the plasma emission light. A blown up image of the light from the plasma emission through a Corning color filter that blocks the 1064nm ablation light with the CCD camera in imaging mode is shown in Figure 3.23. Since the plasma light is so intense, the camera lens is set to the smallest aperature, f/16, and the vertical pixels are not binned together, which helps to prevent saturation. A longer distance from the barium metal to the camera lens also helps to prevent saturation because the solid angle is reduced. The image size of the plasma on the LN₂-cooled CCD is also reduced as the distance between

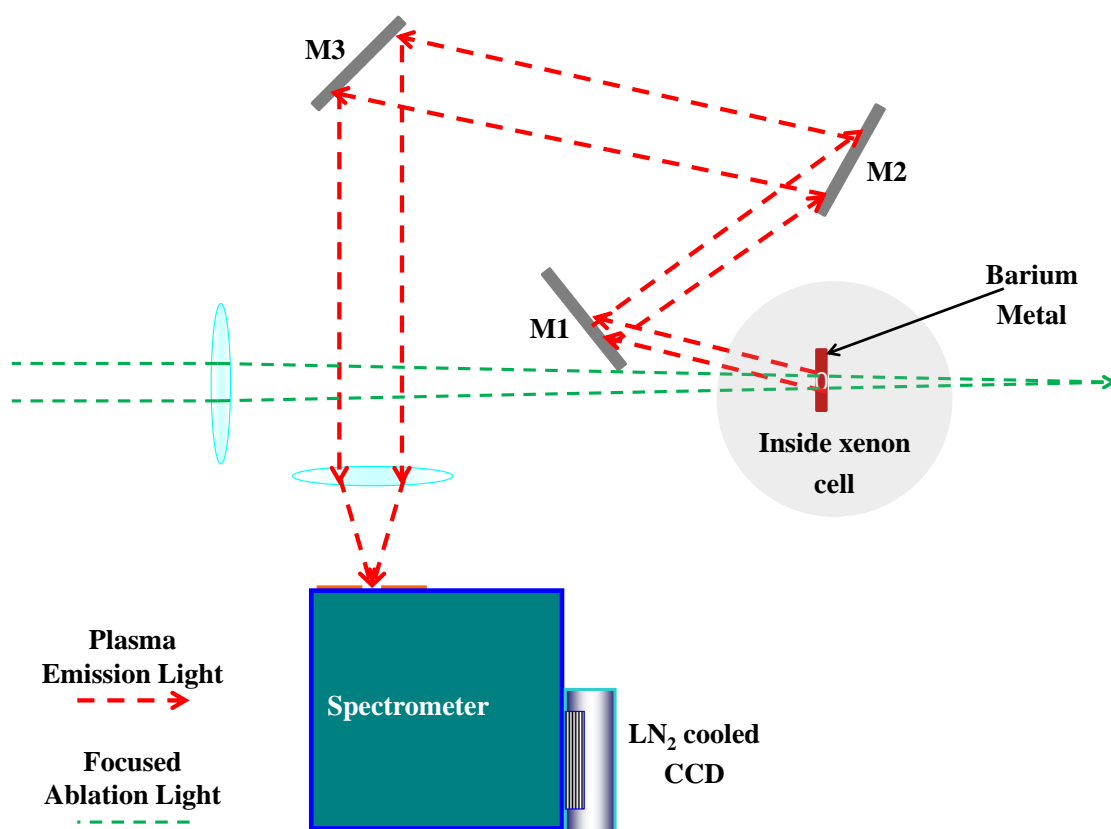


Figure 3.22: Plasma emission setup. Notice that the ablation laser is focused beyond the barium metal in order to have better control of the ablation process.

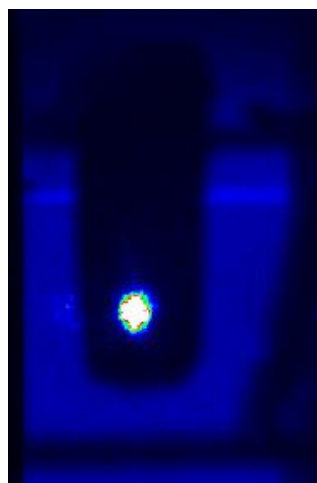


Figure 3.23: Image of the plasma emission from ablation of the barium metal.

the barium metal and camera lens increases. This allows for better spectral resolution since the size of the plasma is imaged onto less pixels. In the best case the image size of the light from the plasma was only 3x3 pixels. ND filters could have been used to prevent saturating the LN₂-cooled CCD, and the slit could have been narrowed to get the same spectral resolution. As will be shown later in the results chapter, the plasmas emission spectrum is studied as a function of ion charge. Since the physical spot size of the plasma and the total amount of light collected is expected to change as the laser energy is varied, it was decided to have the same optical elements, and experimental setup for every ablation shot.

3.5.3 Time Resolved Fluorescence

It is interesting that the fluorescence signals are generally seen when there is a visible flash seen in the laser region of the room temperature camera as seen Figure 3.18. It is important to determine if the flash is from particles scattering at the excitation wavelength or emission from Ba⁺ ions that absorbed the excitation light. The key experimental method used to study the fluorescence spectra and particle scatter are the time resolved studies. Since the Ba⁺ ions take about 3 seconds to travel the drift distance in the liquid xenon, the LN₂-cooled CCD is set up to take multiple shorter frames in order to compare the duration of the observed fluorescence spectrum with the timing of the Ba⁺ ion current. Because of the shorter frames, the Raman filter could be rotated until a fraction of the light from the excitation wavelength could be observed without saturating the CCD. If particles exist, it is expected that they will scatter at the same wavelength as the excitation laser. A relative measurement of the amount of particle scatter compared with the total amount of the light collected from the fluorescence spectrum and the correlation of the duration of the particle scatter with timing of the Ba⁺ ion current will be analyzed in Chapter 5.

3.5.4 Collection Efficiency

The total detection efficiency, ϵ_{tot} , includes many factors multiplied together and is summarized in Table 3.2. The collection efficiency, $\epsilon_{C.E.}$ is determined by the solid angle calculation,

$$\epsilon_{C.E.} = \frac{\pi R_{eff}^2}{4\pi f_l^2} \quad (3.25)$$

where f_l is the focal length of the first collection lens. The effective radius of the cone of light collected R_{eff} is limited by the by the f-number of the spectrometer, $f/\# = f/D_{eff} = f_s/(2R_{eff})$, where f_s is the focal length of the lens used to focus the light into the spectrometer. The f-number of the spectrometer is 4, so the collection efficiency becomes

$$\epsilon_{C.E.} = \frac{f_s^2}{256 * f_l^2} \quad (3.26)$$

A 50mm focal length Nikon lens, $f_l = 5cm$ is used to focus the light into the spectrometer, and the focal length of the collection lens for all the experiments shown was 10cm. The transmission of each optical element, 2 windows and 2 lenses, is about 96%. Three mirrors are used to image the light into the spectrometer. The transmission of each mirror is estimated to be 90%. The values for the CCD quantum efficiency, $\epsilon_{Q.E.}$, grating transmission, $\epsilon_{grating}$, and transmission of the Raman filter, ϵ_{Raman} are determined from the curves given by the manufacture: they are 90%, 50%, and 95% respectively. The digitization factor, $\epsilon_{digitization}$, is 0.5 counts per photon when the CCD is operating in slow ADC.

ϵ	Description	value
$\epsilon_{C.E.}$	Collection Efficiency	9.77E-4
ϵ_{optics}	Optics Transmission	0.85
$\epsilon_{mirrors}$	Mirror Transmission	0.73
$\epsilon_{Q.E.}$	CCD Quantum Efficiency	0.90
$\epsilon_{grating}$	Grating Transmission	0.70
ϵ_{Raman}	Raman Filter Transmission	0.95
$\epsilon_{digitization}$	CCD digitization	0.50
ϵ_{total}	Total Detection Efficiency (counts/e)	1.81E-4

Table 3.2: Collection Efficiency

Chapter 4

Results: Nonresonant Multiphoton Ionization

The results and analysis of experiments in ionization of liquid xenon via nonresonant multiphoton ionization (NRMPI) using 221nm, 266nm, 280nm, and 355nm pulsed laser light are presented in this Chapter. These wavelengths have photon energies of 5.61eV, 4.66eV, 4.43eV, and 3.49eV respectively. All are far less than 9.3eV band gap energy needed to create an electron-hole pair in the liquid xenon. The order n of the nonlinearity of the NRMPI process is determined for all wavelengths. Cross sections are only determined from ionization with 266nm and 280nm wavelengths since the absolute laser energy of the 221nm and 280nm pulses were not known due to the inability to measure the small amount of energy with the available Joule meter.

As discussed previously, in the intensity regime far below saturation, the number of atoms ionized is given by

$$N_{e^-} = n_o \sigma^{(n)} \tau_n V_n \left(\frac{\epsilon}{E_p A_o \tau_n} \right)^n \quad (4.1)$$

If no electrons are lost to combination with impurities or recombination with the xenon holes left behind, Equation 4.1 simplifies to

$$s = C_n \tau_n^{(1-n)} K_n \sigma^{(n)} \epsilon^n \quad (4.2)$$

where the values of C_n , K_n , and τ_n were discussed in Section 3.4 and listed again in Table 4.1. The order n of nonlinearity is a constant determined for each wavelength. The two variables

$\lambda(\text{nm})$	n	$C_n(\text{atoms} * V/\text{cm}^3/\text{J}^n)$	$\tau_n(\text{s})$	$K_n(\text{cm}^{3-2n})$
266	2	7.63×10^{50}	$(4.50 \pm 0.5) \times 10^{-9}$	$(4.65 \pm 1.28) \times 10^3$
355	3	2.42×10^{69}	$(5.50 \pm 0.5) \times 10^{-9}$	$(2.90 \pm 0.31) \times 10^6$

Table 4.1: Laser beam and liquid xenon parameters

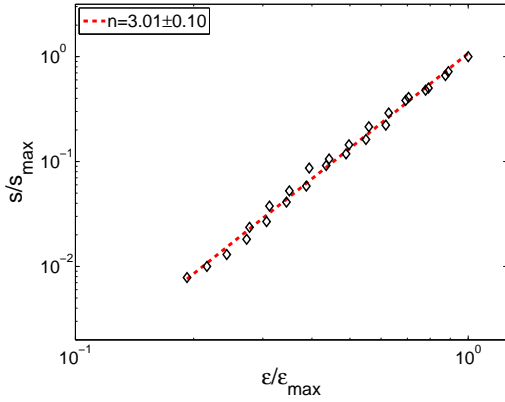
are the number of electrons created in the process, s , and the laser energy, ϵ .

4.1 Order n of the Multiphoton Process

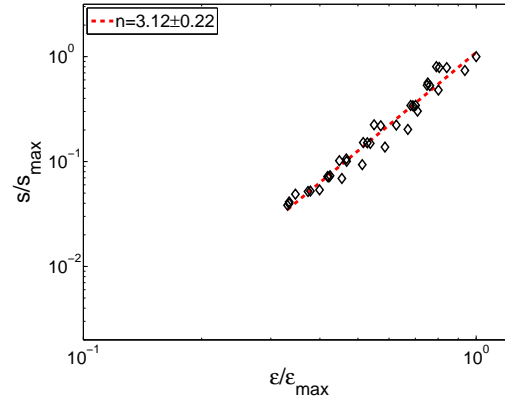
Normalizing Equation 4.2 by the maximum signal taken during each data set gives

$$\frac{s}{s_{max}} = \left(\frac{\epsilon}{\epsilon_{max}} \right)^n \quad (4.3)$$

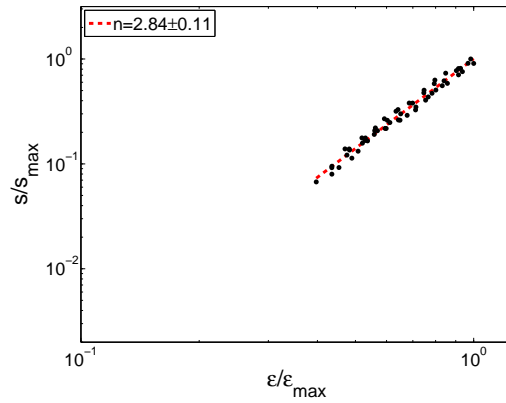
Equation 4.3 is a convenient way of calculating the value of n since only the relative change in laser energy per measurement is needed. Thus the value of n for 221nm and 280nm was determined even though the absolute energy of the laser and variables listed in Table 4.1 for the two wavelengths were not known. Each measurement of s and ϵ consisted of an average of 320 laser pulses with a statistical error of less than 1 percent. The laser energy was attenuated approximately 10 times for each measurement to determine the slope. For the experiments when the attenuation factor was used to determine the difference between the laser energies, the laser energy before the attenuators was recorded in order to measure fluctuations.



(a) relative laser power



(b) relative laser power



(c) absolute laser power

Figure 4.1: Normalize log-log plots for NRMPI of liquid xenon with 355nm pulsed laser light. The slope determines the number of photon absorb to create an electron-hole pair in the liquid xenon.

Several combined data sets for experiments on the same day using a focused 355nm pulsed laser beam are shown in Figure 4.1. A data set consists of one run with the laser attenuated 10 times. The diamond markers are the measurement taken when the laser energy was recorded before the attenuators, Figure 4.1a and Figure 4.1b. The solid line is the best linear fit to Equation 4.3. The slope is the order n of the nonlinear process. One can see that this is a three-photon process. The error on the slope is obtained from the 95% confidence bounds of the linear fits. More experiments were conducted with 355nm in order to gain confidence in the alignment procedure. The consistency in comparison between the experiments conducted with the relative power using the attenuation factor and absolute power for 355nm provides confidence that the value of n could be accurately measured without knowing the absolute power. Combined data sets for the other 3 wavelengths are shown in Figure 4.2. Again, the diamond markers are for the experiments conducted using the relative laser power.

It is apparent from the measurements shown that value of n is 2 for 221nm and 266nm, and 3 for 280nm. As shown in Figure 4.3, these results demonstrate that the measured values of n for the respective wavelengths studied are equal to the minimum number of photons needed to create an electron-hole pair in the liquid xenon.

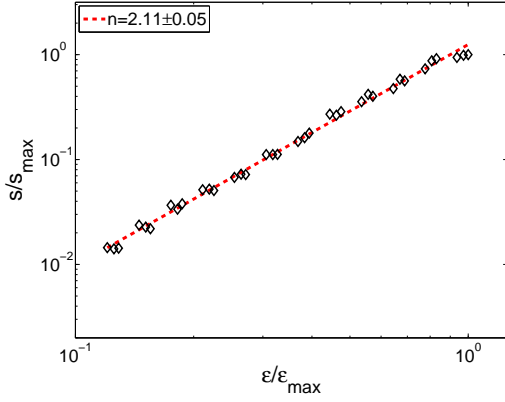
4.2 Cross Section Calculations

The cross sections were calculated by solving Equation 4.2 for $\sigma^{(n)}$, thus

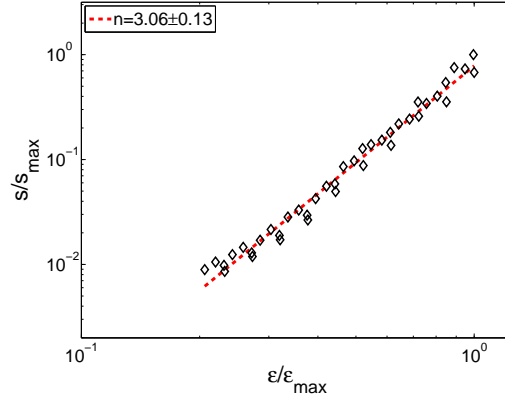
$$\sigma^{(2)} = \frac{\tau_2}{C_2 K_2} \frac{s}{\epsilon^2} \quad \text{for } \lambda(266nm) \quad (4.4)$$

$$\sigma^{(3)} = \frac{\tau_3^2}{C_3 K_3} \frac{s}{\epsilon^3} \quad \text{for } \lambda(355nm) \quad (4.5)$$

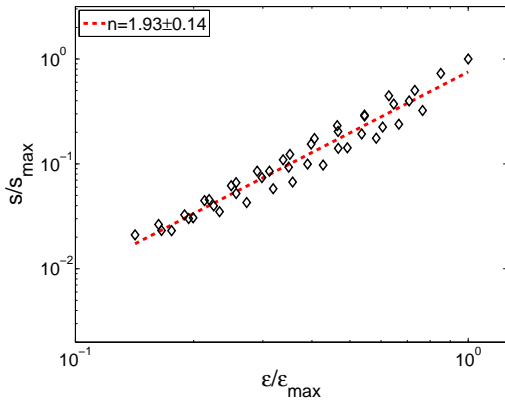
For each experiment, a cross section was calculated for every measurement of s and ϵ . Because the value of n is quantized, the results from the previous section verify that n should be 2 for ionization with 266nm and 3 for 355nm. Since statistical error of s , and ϵ , are less than 1 percent, the largest source of error in the measurement is from the calculation



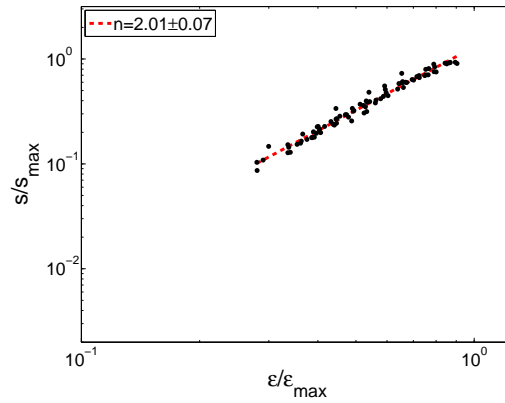
(a) 221nm: relative laser power



(b) 280nm: relative laser power



(c) 266nm: relative laser power



(d) 266nm: absolute laser power

Figure 4.2: Normalize log-log plots for NRMPI of liquid xenon with 221nm(a), 280nm(b) and 266nm (c,d) pulsed laser light. The slope determines the number of photon absorb to create an electron-hole pair in the liquid xenon.

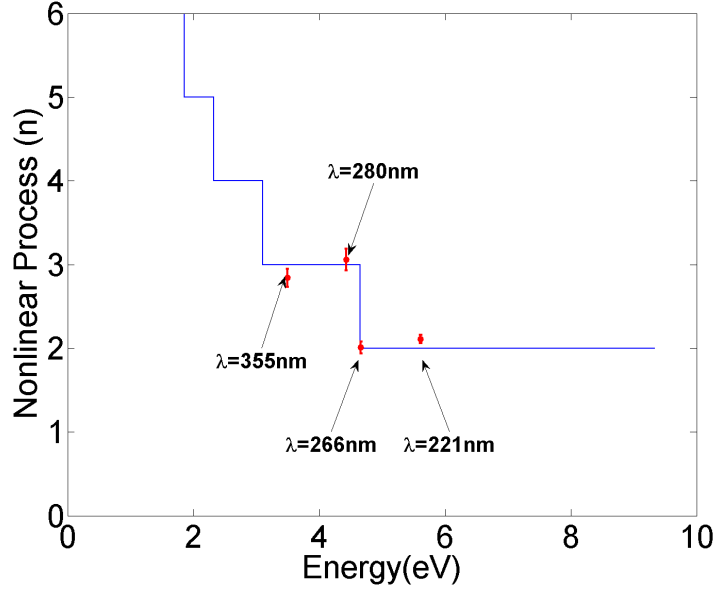


Figure 4.3: The solid line shows the minimum number of photons needed at different laser photon energies in order to create an electron-hole pair in the LXe. The dots represent measured order n of nonlinearity of the multiphoton ionization at four wavelengths.

of K_n , and the estimate of the interaction time τ_n , both systematic errors. Both errors are listed in Table 4.1 and added in quadrature according to

$$\Delta\sigma^{(n)} = \sqrt{\left(\frac{\partial\sigma^{(n)}}{\partial K_n}\Delta K_n\right)^2 + \left(\frac{\partial\sigma^{(n)}}{\partial\tau_n}\Delta\tau_n\right)^2} \quad (4.6)$$

The cross sections calculated for experiments of Figure 4.1c and Figure 4.2d are shown in Figure 4.4. The solid line in the plots is the mean value and the dotted lines are the high and low error limits including systematic errors. The non resonant 2 and 3 photon cross sections calculated for ionization of liquid xenon with 266nm and 355nm are $(1.19 \pm 0.33) \times 10^{-51} \text{ cm}^4\text{s}$ and $(6.95 \pm 0.77) \times 10^{-81} \text{ cm}^6\text{s}^2$ respectively.

4.3 Discussion

The ability to ionize liquid xenon with focused pulsed laser beams is significant for two reasons. First it gave us the ability to have a localized electron source for our liquid xenon

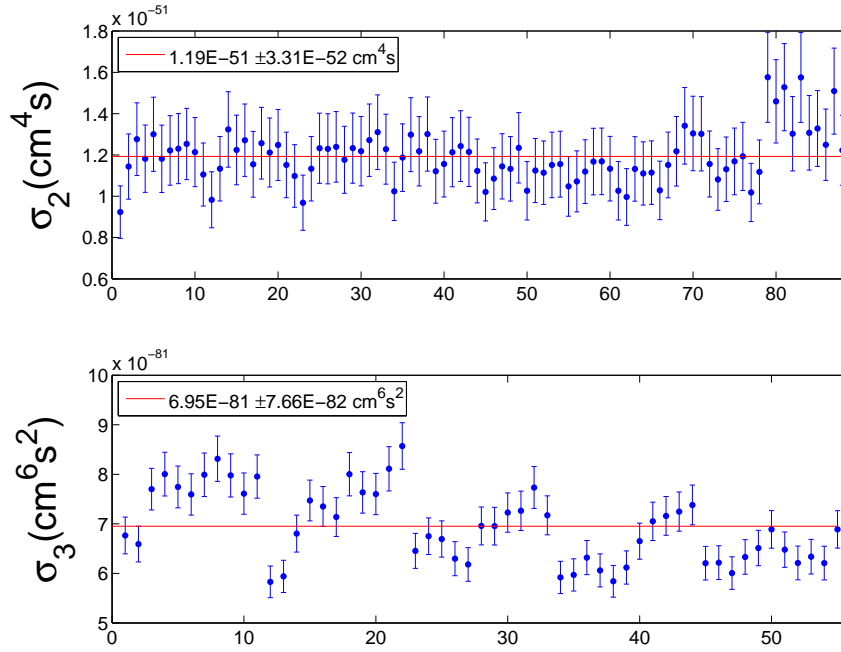


Figure 4.4: Calculated cross sections for ionization with 266nm(top) and 355nm(bottom)

purity monitor. The creation of the electrons in our purity monitor is unique since previous liquid xenon purity monitors used electrons created by hitting a piece of gold metal with 266nm pulse light via the photo-electric effect. After it was realized that we were ionizing the liquid xenon directly via nonresonant multiphoton ionization, we were able to more precisely measure the purity of the liquid xenon. Understanding the purity of the liquid xenon is important for the interpretation of the fluorescence results which is discussed in the next Chapter. Secondly these results are the first measurements of the order n of the nonlinear multiphoton ionization of liquid xenon for a series of wavelengths. We also report the first measurements of the of the nonresonant two-photon and three-photon ionization cross sections of liquid xenon using 266nm and 355nm pulse light respectively. The values of n measured are consistent with the minimum number of photons needed to create a xenon-hole pair in the liquid xenon for the respective wavelengths studied. With a more sensitive Joule meter, measurements of the corresponding cross sections for photon ionization of liquid

xenon using 221nm and 280nm wavelengths should be straightforwardly using the same experimental techniques.

Chapter 5

Results: Ba⁺ Spectroscopy

In this chapter, the results and analysis of the experiments to determine the excitation and emission spectrum of Ba⁺ ions in liquid xenon (LXe) are presented. The only previous spectroscopy studies of Ba⁺ ions in LXe were performed by our group. The most intriguing aspects of the preliminary experiments were the huge fluctuations in the total integrated fluorescence spectrum, and an apparent reduction in the signal as the excitation laser was moved further from the LXe surface. One possible explanation proposed was that the Ba⁺ ions might be attaching to impurities in the liquid xenon, specifically oxygen, causing a reduction in the fluorescence.

For this thesis work, a cleaner liquid xenon system with a purity monitor was constructed, and the fluorescence studies were continued. The measurements of the less than 30ppb O₂ equivalent purity concentration provided evidence that the attachment to impurities might not be responsible for the apparent decrease or disappearance of the fluorescence spectrum. In the initial experiments of this thesis work, two key new features were noticed. (1) The observance of the fluorescence spectrum somewhat correlated with the observance of particles in the video camera used to monitor the experiments, and (2) having an oxide layer on the barium target generally increased the frequency of observation of the fluorescence spectrum with the LN₂-cooled CCD and particle scatter observed in the video camera. The particles are visible because they scatter light from the excitation laser.

Thus a major focus of this thesis was to distinguish between the observed fluorescence spectrum and particle scattering. In particular, the goal was to compare the size of the integrated fluorescence spectrum and integrated laser scatter peak as well as the timing of both with the Ba^+ current signal for the different barium target conditions listed in Section 3.2. In addition to the time resolved comparisons, new studies of the plasma emission spectra from the ablated barium sample were performed. Identification of the emission lines in the spectrum is verification of the atomic and ionic species that are introduced into the liquid.

The plasma emission studies are presented first in Section 5.1. The observed fluorescence spectrum from the excitation with the 9 argon ion laser wavelengths will be presented and briefly discussed to explain the general shape and other details in Section 5.2. The series of experiments using the time resolved technique as a function of different barium tip condition are presented last in Section 5.3.

5.1 Plasma Emission Spectra

A typical plasma emission spectrum is shown in Figure 5.1. The spectrum was taken by looking at the ablation plasma directly, as explained in Section 3.5.2. All 31 major peaks have been identified to be those of neutral Ba atoms and Ba^+ ions. The two strong Ba^+ emission lines from the 6p excited states back to the 6s ground state, the Ba^+ emission from the 6p state to the two meta-stable 5d states, and the strong 6s6p-6s² emission of the neutral Ba are labeled in the figure. The total integrated plasma emission spectrum and the total charge from the integration of the Ba^+ ion current for individual ablation shots are shown in Figure 5.2 as a function of shot number. The amount of charge was varied by changing the ablation laser energy. The plot in the figure is not a correlation plot, but it does show similar size fluctuations between the two. Shown in The same data set is plotted in Figure 5.3 as the total integrated plasma emission spectrum vs. Ba^+ ion charge. A good linear correlation between the plasma emission spectra and the Ba^+ charge is demonstrated from the plot.

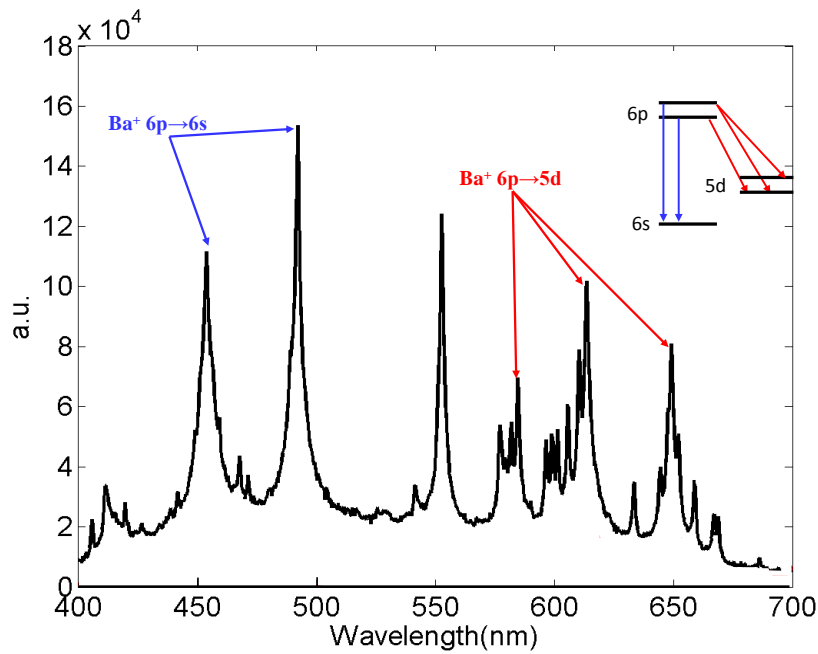


Figure 5.1: Plasma emission spectra of the laser ablated barium target. The spectrum was taken with the plasma imaged directly into the CCD. The unlabeled peak is that of neutral Ba.

The linear relationship shown in Figure 5.3 and the identification of only Ba and Ba^+ ions in the plasma emission spectra is evidence that the charge passing through the liquid is truly that of Ba^+ ions.

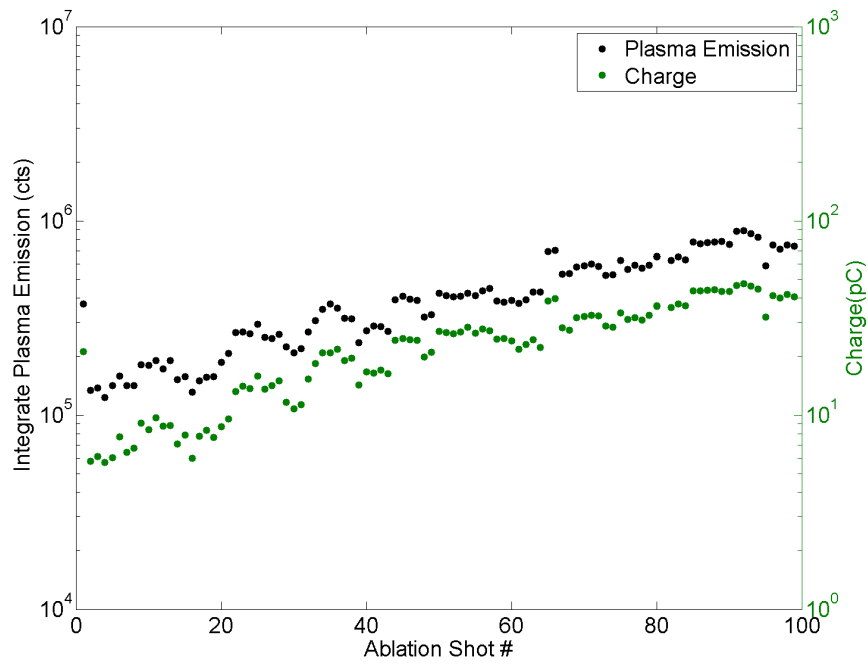


Figure 5.2: The integrated plasma emission spectra and total charge for individual ablations shots.

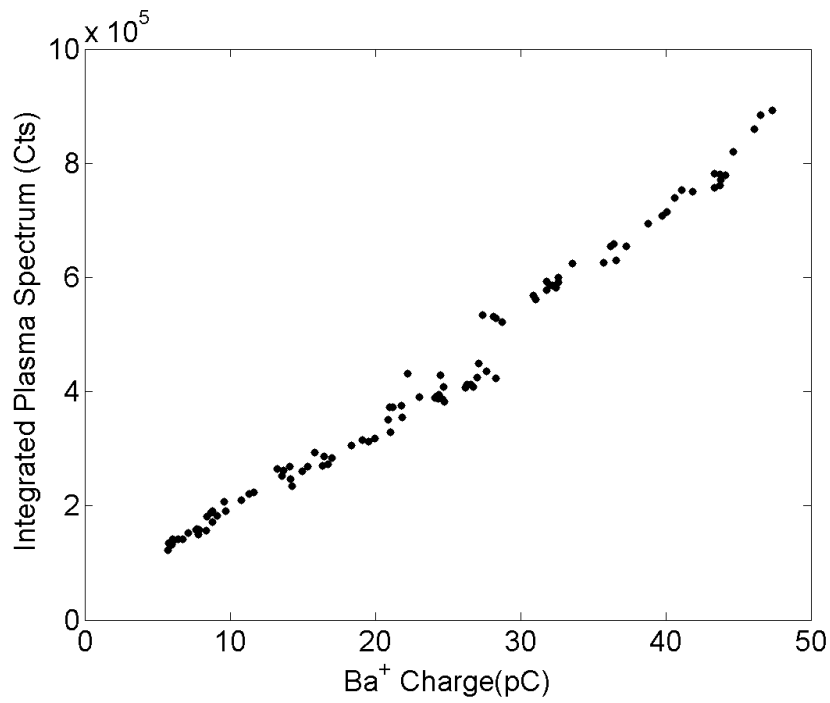


Figure 5.3: The integrated plasma emission spectra vs total charge for individual ablations shots.

5.2 Observed Fluorescence Spectra

Examples of observed fluorescence spectra from excitation with the 9 discrete argon ion

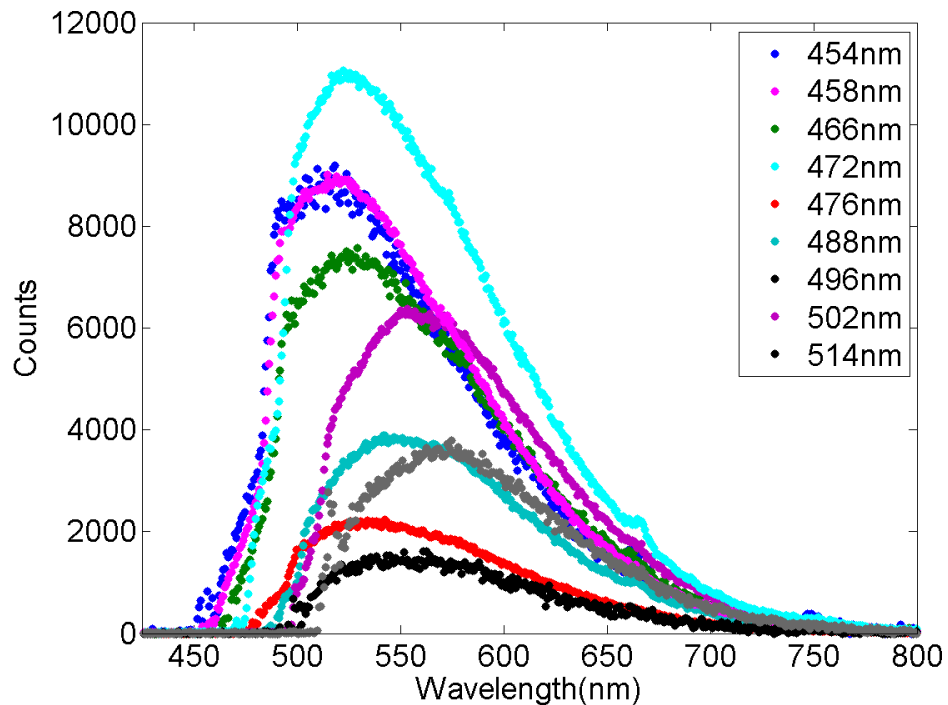


Figure 5.4: The observed spectrums excited with all the Argon-Ion laser wavelengths.

laser wavelengths on the same day are shown in Figure 5.4. The large amount of light from the plasma emission spectrum was not present in the fluorescence spectra because the ablation laser was fired a few milliseconds before the shutter of the CCD camera was opened. Since the Ba^+ ions take seconds to travel through the liquid, the shutter was typically open for 5 seconds to ensure that the entire duration of the fluorescence spectrum was observed. The Raman filter was rotated as the wavelength was changed so that more of the fluorescence light below the 514nm cutoff of the Raman filter could be collected while keeping each of the argon ion wavelengths below the cutoff. The sharp cutoff of the rotated Raman filter is seen in each spectrum. A background spectrum taken before and after each ablation shot was subtracted from the fluorescence spectrum. The background spectrum is taken without laser ablation.

A broad emission that is red shifted from the respective excitation wavelength is observed in all the spectra shown in Figure 5.4. The observed emission extends from the excitation wavelength to about 700nm. The FWHM of the spectra is about 125nm for the excitation wavelengths 488nm and below, and about 100nm for wavelengths 496 and higher. There is also noticeable shift of the peaks. However, it should be noted that the FWHM and shift are likely affected by the cutoff of the Raman filter.

The spectra might be attributed to the emission of Ba^+ ions as they decay from the 6p excited states back to 6s ground state. Given that the emission is so broad, no clear identification of emission from the excited 6p states to the 5d metastable states can be identified, although it is possible that it might be embedded in the high wavelength tail of the broad spectrum. These spectra are consistent with the observations seen in the preliminary experiments conducted prior to this thesis.

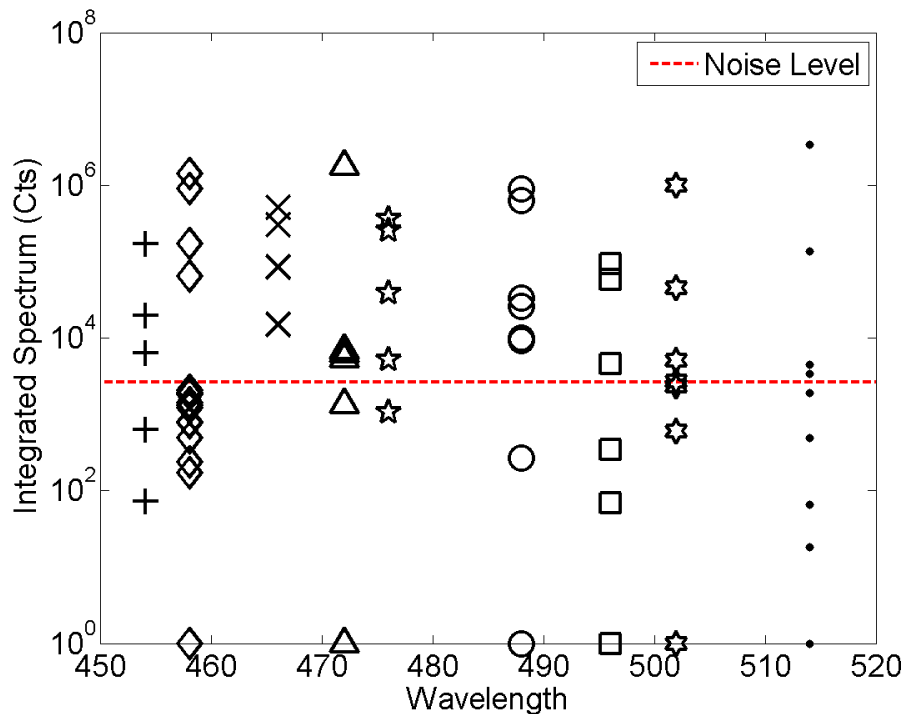


Figure 5.5: The total integrated fluorescence spectrum for individual ablation shots for excitation with 9 argon ion wavelengths normalized by laser power. Each marker represents a single ablation shot.

The total integrated fluorescence spectrum for individual ablation shots normalized by laser power and charge for this data set is shown in Figure 5.5. Each marker on the plot represents an ablation shot. The minimum detectable signal is determined by the following procedure: the background spectra before and after each ablation shot were subtracted and integrated. Next, the absolute value of the all subtracted background spectra was then averaged. The dotted red line in Figure 5.5 is this level. A large variation in signal is seen for all wavelengths, and fairly often the integrated fluorescence spectrum was below the noise level. The times when a fluorescence spectrum minus background integrated to a negative number were assigned a value of 1 so that those ablation shots could be plotted on the semi-log y axis. Even for the fluorescence spectra that were above the noise level, approximately 2 orders of magnitude variation existed.

Prior to conducting these experiments with a controlled tip condition, many different experimental variables and parameters were varied in order to obtain consistency in the size of the total integrated spectra. Consistency was not achieved for excitation with any of the discrete argon ion wavelengths or any condition tried. It was apparent that the observation of a fluorescence spectra usually coincided with the observance of large scatter light viewed in the room temperature camera. Thus we began the time resolved studies. The best fluorescence size vs. charge and laser scatter results will be discussed from the integration of the time resolved experiments.

5.3 Time Resolved Spectroscopy

The relative size of the particle scattering at the excitation wavelength could be measured if Raman filter was rotated to allow some of the excitation light to pass through. The amount of transmitted scattered light at the excitation wavelength was adjusted so that a large particle would not saturate the CCD on any frames. By integrating different portions of the spectrum, the relative size of the particle scatter and the observed fluorescence spectrum

could be compared. Taking multiple shorter frames also allowed both the particles and fluorescence to be correlated with the timing of the Ba^+ ion current.

The stray light from the plasma emission spectrum was always collected in a separate frame and integrated. An example of the plasma emission spectrum collected from the stray

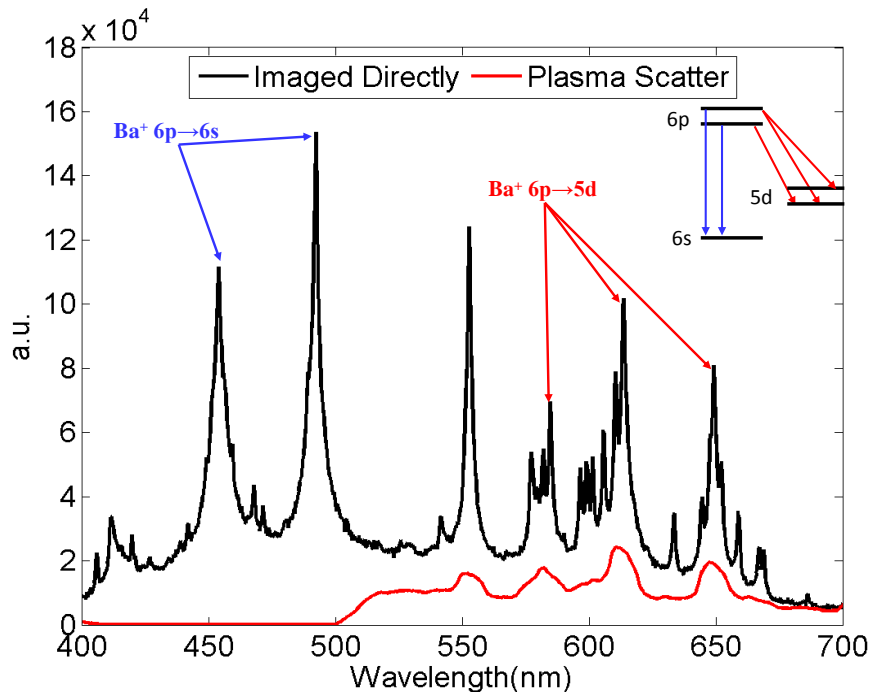


Figure 5.6: Plasma emission spectra of the laser ablated barium target. The red spectrum is from stray light picked up during the fluorescence experiments. The black spectrum is the same as the one shown in Figure 5.6. The spectra are consistent.

light from frame 2 before any fluorescence light was expected is shown in the red curve in Figure 5.6. The black plot is the same plasma emission spectrum that was shown in Figure 5.1. In comparison with the black spectrum, the cutoff at low wavelengths is evident. This is due to the Raman filter that was inserted to block the Rayleigh and Brillouin scatter light for the fluorescence studies. The stray light spectrum is noticeably broader because the slit on the spectrometer was open more to image the entire excitation beam. The emission from first excited 6p states to the 5d metastable states of the Ba^+ ions is clearly observed. The purpose of the comparison between the two plasma emission spectra is to show that they

are consistent. Given the good correlation with charge shown previously in Figure 5.3, the plasma emission spectrum from the stray light is a good indicator of the amount of Ba^+ in the liquid. Thus the size of the plasma emission spectrum was used as an additional source of information in the analysis.

For clarity, the measurable parameters that were recorded and compared in the time resolved studies are listed below:

1. Total Ba^+ plasma emission spectrum vs. Ba^+ ion charge
2. Total size of the fluorescence spectrum vs. total size of excitation laser scatter
3. Total size of fluorescence spectrum/excitation laser scatter vs. charge
4. The time dependence of the laser scattered light and fluorescence spectrum vs. that of the ion current

Each of the 4 comparisons was performed for the 3 different Ba^+ target conditions described in section 3. Since the huge fluctuation in the total size of the fluorescence spectrum was observed for excitation with all the argon ion wavelengths, only data from excitation with 502nm with fixed laser power for all experiments will be shown. The ablation intensity was sometimes varied slightly on different days of experiment in order to produce different amounts of Ba^+ charge, but it was not changed once an experiment began. The electric fields were kept constant for all comparison, but the height of the liquid varied slightly because the liquid xenon was recovered after each experiment and re-condensed before the next.

A typical Ba^+ ion current (black curve), with the shutter state of the CCD for reference (blue curve) is shown in Figure 5.7. The experiments began by triggering the CCD shutter to open. The duration of each frame was set to 0.3s and it took the CCD 0.25s to process each frame. The ablation laser was always triggered in the second frame 0.7 seconds after the CCD shutter was opened for the first time. The sharp photoelectron spike in the current denotes the time of the ablation laser pulse. The light from the plasma emission spectrum is always observed in this frame. According to the width of the current shown and since

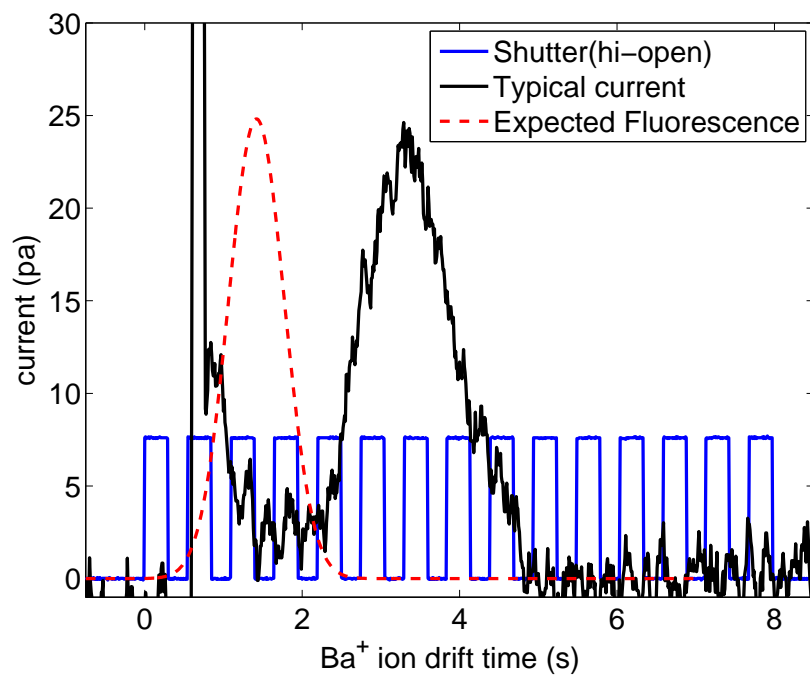


Figure 5.7: A typical current signal shown with the shutter state of the CCD and the expected duration of the fluorescence spectrum.

the ions pass through the laser beam before being collected, the fluorescence spectrum was expected to be in the first 5 frames after the ablation frame on grid 2. To calculate the total size of the fluorescence and laser scatter signals, integrated counts in 7 frames after summed. The use of 7 frames allows for fluctuation in the time of the peak of the current. The results of the time resolved experiments are presented in following sections grouped according to the type of Ba target used.

5.3.1 Oxidized Ba Metal Experiments

The comparison between the Ba^+ charge and the size of the total integrated plasma emission spectrum for each ablation shot is shown in Figure 5.8. All experiments were conducted by hitting a few different spots on the oxidized barium metal target except the one shown in Figure 5.8b, in which a single spot was ablated. The most noticeable feature of the plots is the reduced size of the total plasma emission spectrum and Ba^+ charge in the first few ablation shots on a new spot. The reduced Ba^+ ion charges that were not detectable above the noise level of the electrometer were assigned a value of 1.

Two photographs of the barium metal tip are shown in Figure 5.9: one before any ablation shot and one after the third shot. This is for the first spot of the experiment shown in Figure 5.8a. A color difference in the ablation area after the third shot is seen. A change in the oxide layer is indicated. For all time resolved studies, photographs such as these were taken until a change in the color of the barium metal was seen. The photographs confirmed the pattern of a current being detectable and greater total plasma emission being observed when the barium metal was exposed. The number of ablation shots it took to see a clear color change depended qualitatively on the amount of oxide exposure.

The other noticeable feature in Figure 5.8 is the constancy in the size of the charge and the total plasma emission after the barium metal was exposed. There are times when an increase in the size of the Ba^+ charge on a new spot does not track exactly with an increase in the total plasma emission from spot to spot. One might argue that this contradicts the

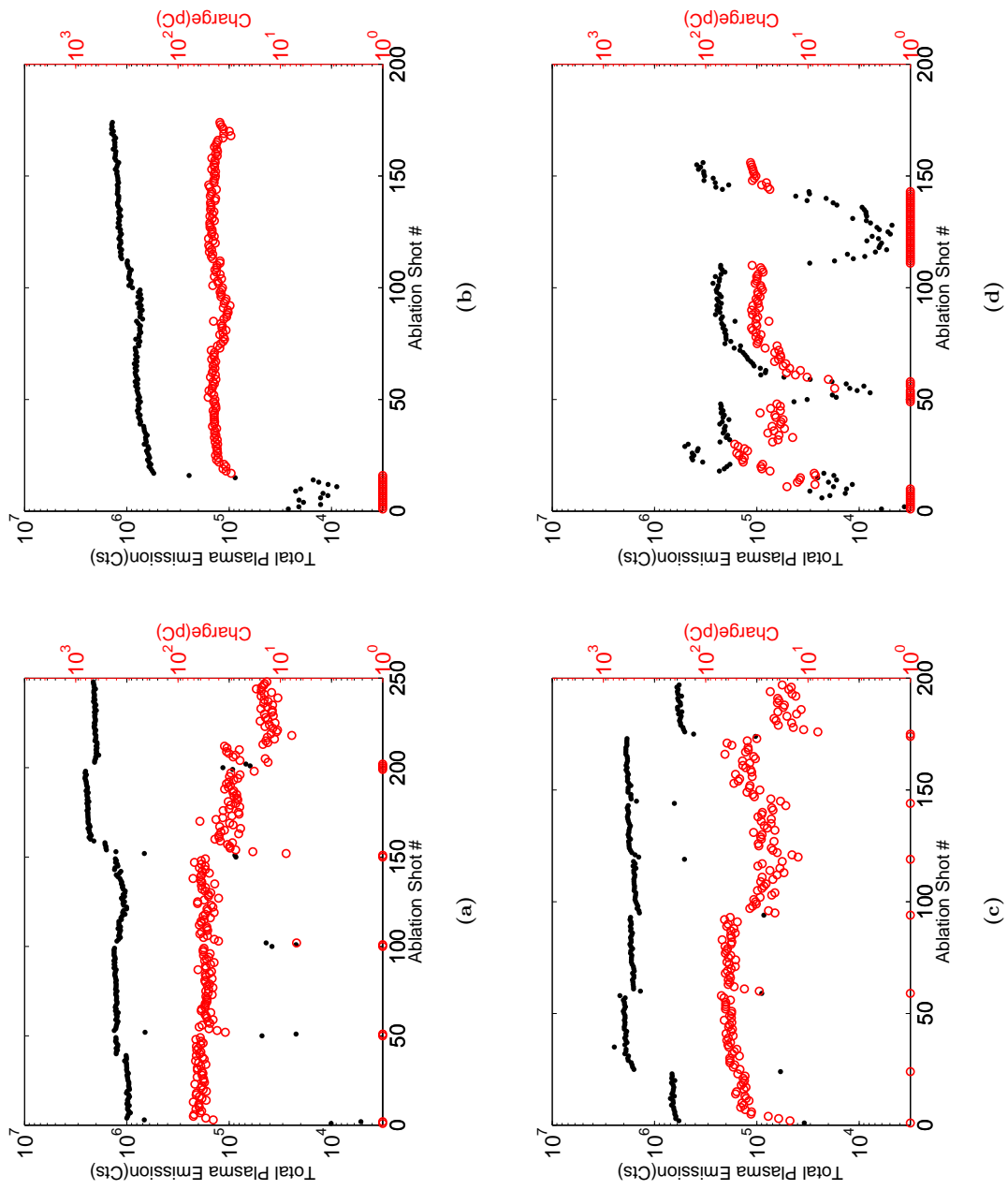


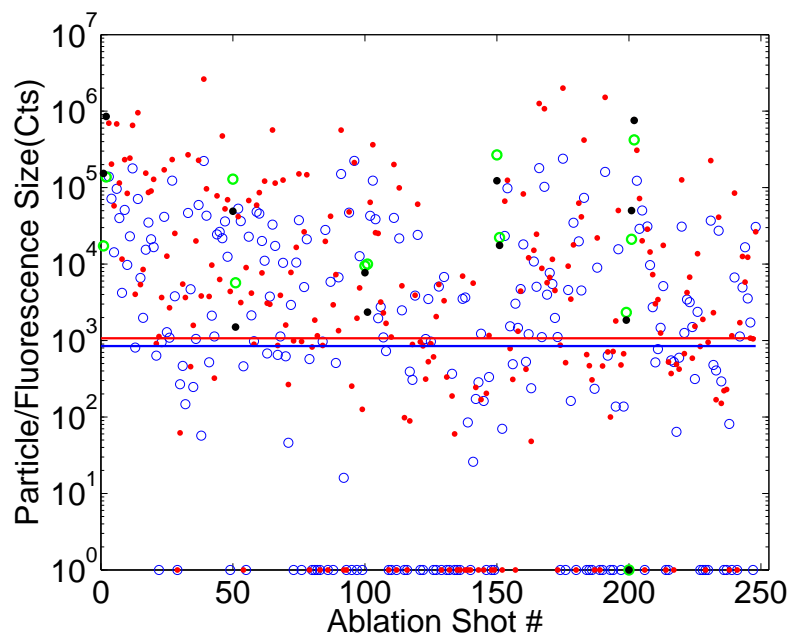
Figure 5.8: The comparison between the size of the integrated plasma emission spectrum (black dots) and total Ba⁺ ion charge (red dots) after each ablation shot for various (a-d) oxidized tip experiments.



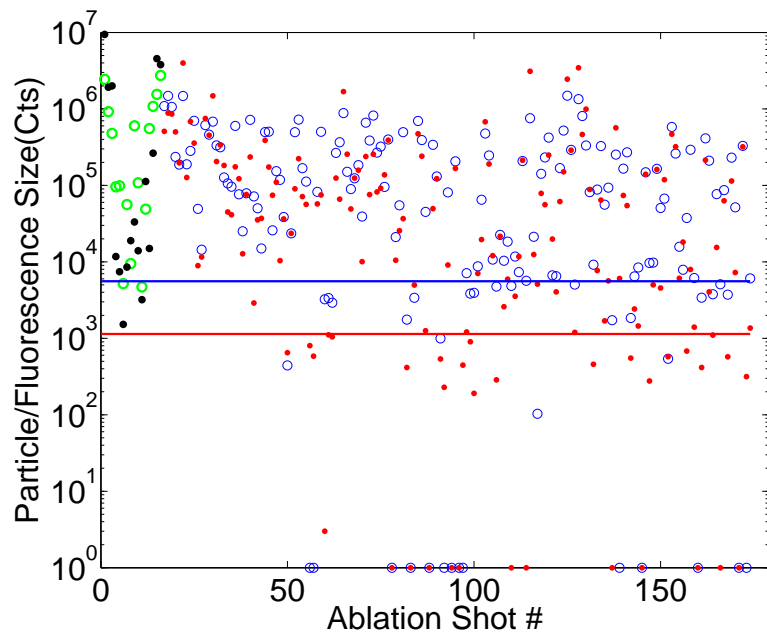
Figure 5.9: Photograph(a) is a picture of the oxidized barium metal tip before any ablation shots. Photograph(b) shows the tip after the first current signals was detected.

linear relationship shown in Figure 5.2. Since the area where the plasma emission originates is not directly imaged, it is possible that the amount of plasma emission light that enters into the spectrometer could vary as the ablation laser is moved to different positions on the barium target. The change in ablation position could cause either more or less of the stray light from the plasma emission spectrum to enter into the spectrometer, causing it to be not directly correlated with the size of the charge when a new oxidized spot is ablated. Notice that once a new spot is established there is consistency between the total plasma emission spectrum and the Ba^+ ion charge.

The integrated particle scatter (circles) and fluorescence spectrum (dots) for each ablation shot are shown in Figure 5.10. It is seen that the size of both particle scatter and the fluorescence spectrum is above the noise level for most shots. The noise level for each frame is determined by the procedure discussed in Section 5.2. In ablation shots where the size of the particle scatter or fluorescence spectrum was below zero a value of 1 was assigned so it could be plotted.

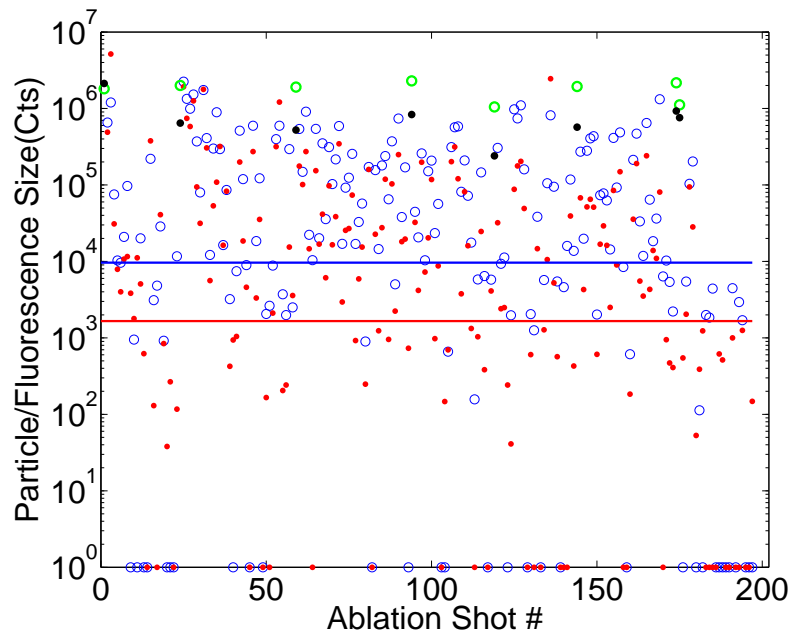


(a)

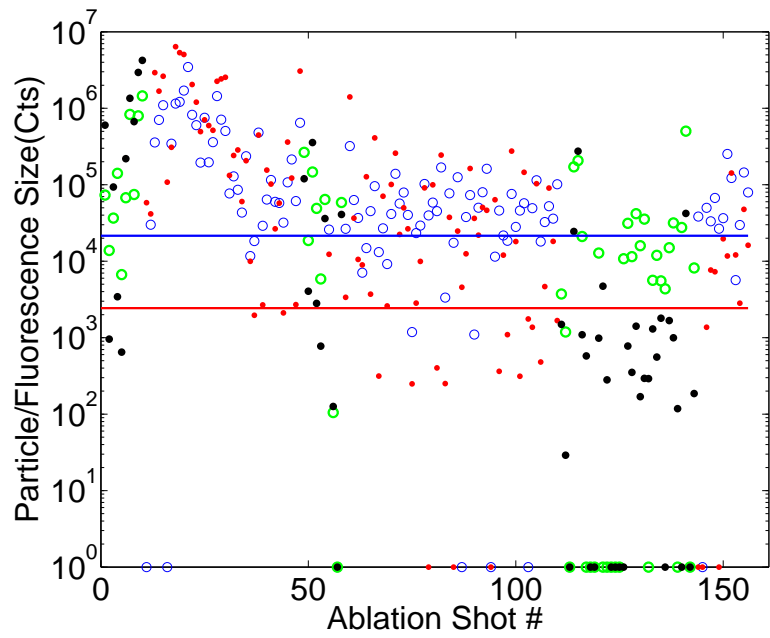


(b)

Figure 5.10: The total size of the particle scatter and fluorescence spectrum after each ablation shot for the same oxidized tip experiments shown in Figure 5.8. The circles and dots represent the size of the particle scatter and fluorescence spectrum for each ablation shot respectively. The black dots and green circles represent the ablation shots that produce no detectable Ba^+ ion current. The red (fluorescence) and blue (particle scatter) lines are the noise levels.



(c)



(d)

Figure 5.10: see previous page for caption

The green circles and black dots in Figure 5.10 correspond to the shots hitting a new oxidized spot on the metal when no current was detected. In many cases a detectable fluorescence spectrum is observed, which is surprising if there are truly no Ba^+ ions in the system. The measurement of a reduced plasma emission spectrum for the ablation shots that produce no current confirms that only a small number of Ba^+ ions entered into the liquid. In all cases of no detectable current, the size of the fluorescence and the particle scatter is neither stronger nor weaker than ablation shots that produced a detectable current. This curious observation is not understood.

The size of the particle scatter and fluorescence spectrum versus the charge for each ablation shot in these experiments is shown in Figure 5.11. Only the sizes of the signals above the noise level are plotted. The plots show a huge amount of scatter, and it is not apparent in any of the experiments shown that either the particle scatter or fluorescence spectrum correlates with the Ba^+ charge.

The correlation between the sizes of the fluorescence and particle scatter signals is shown in Figure 5.12. In all cases, the size of the laser scatter light generally increased when the size of the spectrum increased. However, since both signals vary independently by 2 orders of magnitude, we cannot conclude that there is a direct correlation between the total fluorescence spectrum and the particle scatter from these plots. The red line is a linear fit with a fixed slope of 1.

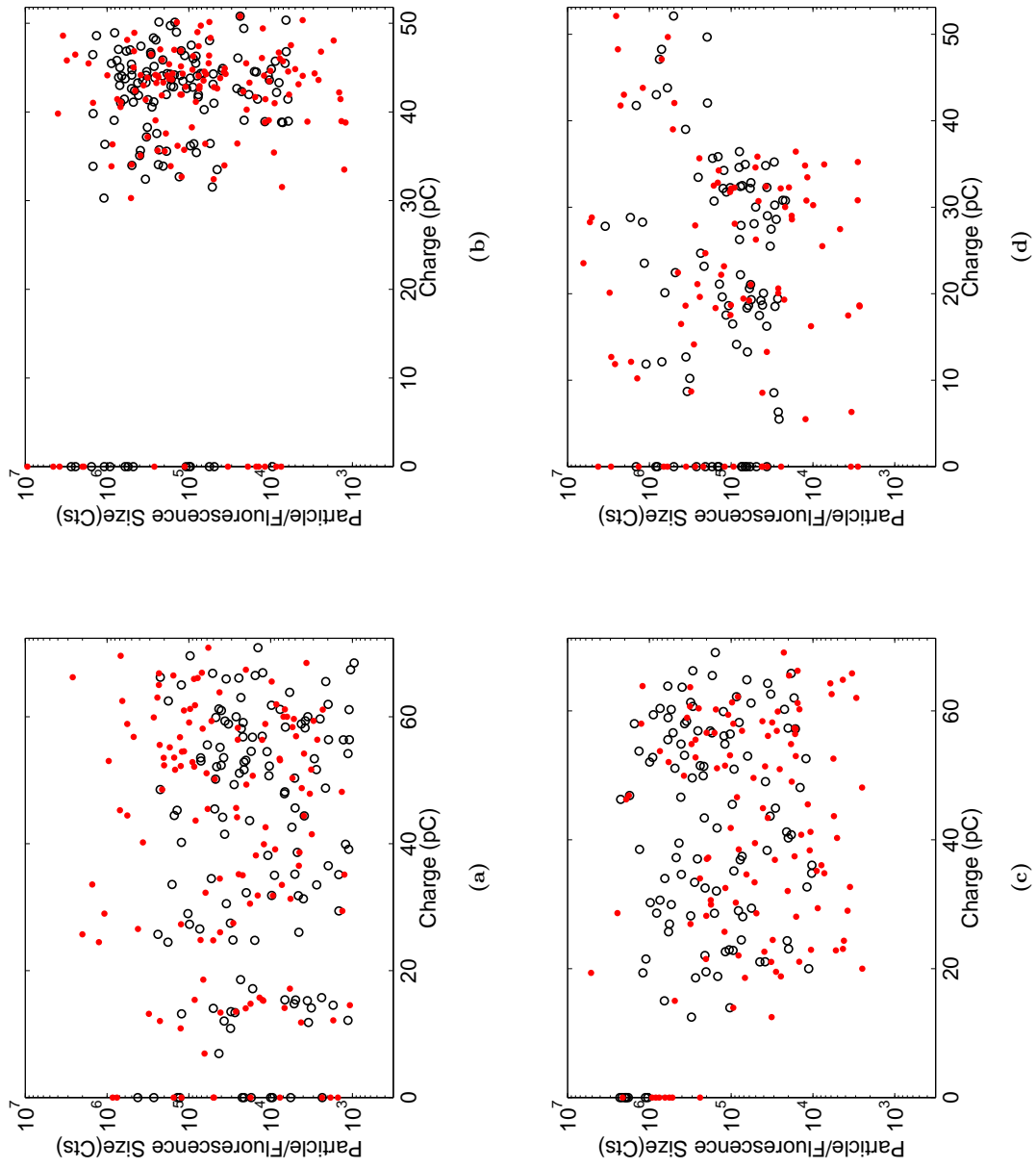


Figure 5.11: Size of the particle scatter (black circles) / fluorescence spectrum (red dots) vs. charge for various oxidized tip experiments.

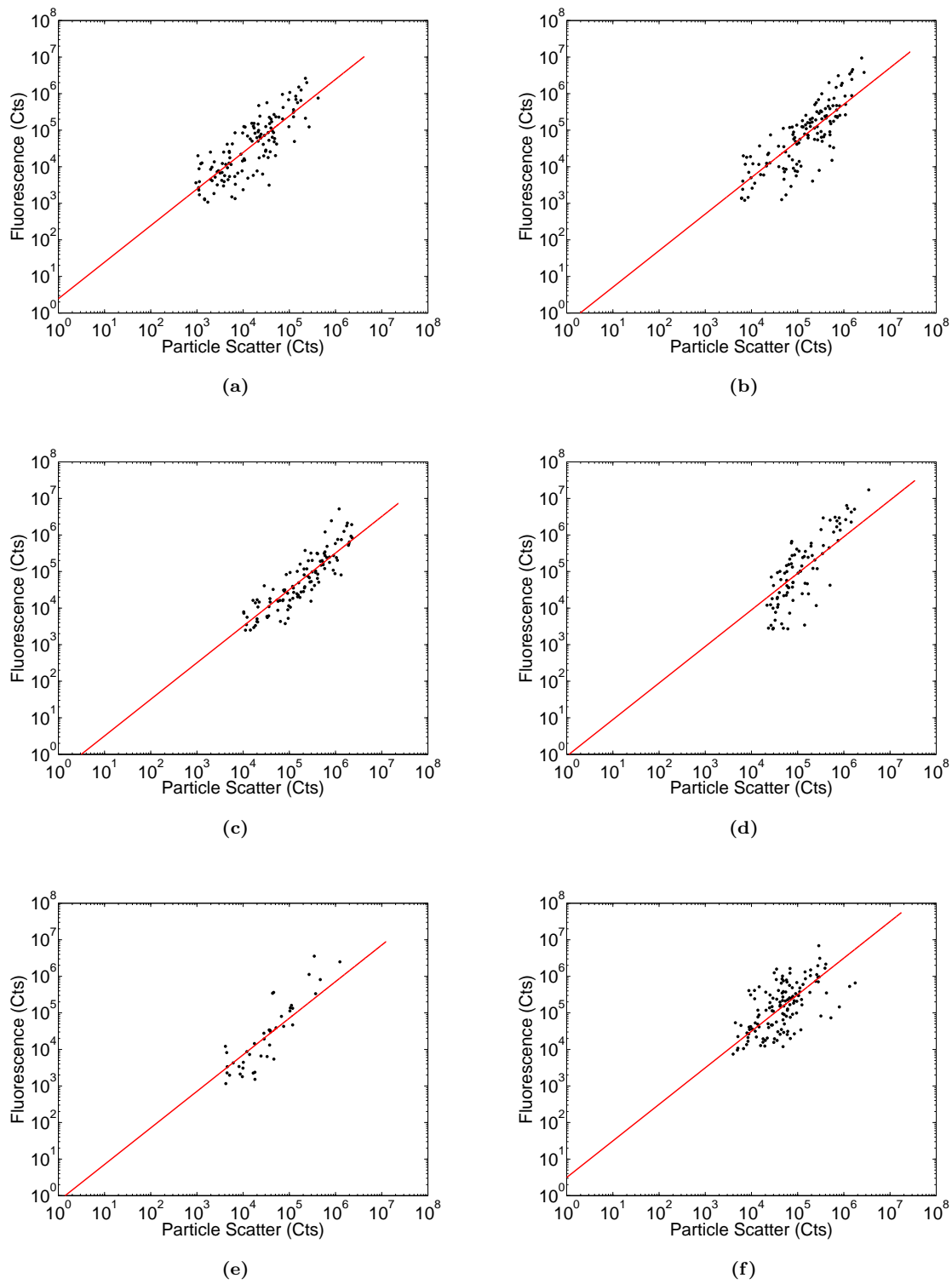


Figure 5.12: Size of the fluorescence spectrum vs. the size of the particle scatter for six oxidized tip experiments. Only the sizes of the signals above the noise levels are shown.

The other possible variable for determining if the fluorescence spectrum is related to particle scatter or excited Ba^+ ions is the time when the signals arrive in comparison with the Ba^+ current. In Figure 5.13 the size of the particle scatter and fluorescence spectrum in each frame is averaged over a whole run, and plotted on the same time scale as the averaged current for six experiments. Only the ablation shots above the noise level are averaged in the plots; also excluded from the average are shots when no current was detected. In all the experiments shown, the excitation laser beam is effectively 6 times closer to the LXe surface than the electrode where the Ba^+ current is being detected. Since the Ba^+ ions take several seconds to travel to the collector electrode, the peak of the integrated fluorescence is expected to be well before the peak of the Ba^+ ion current. In Figure 5.13 it is seen that the fluorescence signal on average comes arrives about the expected time relative to the Ba^+ ion current. The average particle scatter correlates only partially in time with the current and the fluorescence spectrum. The large signals dominate the averaged frame signal since the fluctuation in the size of the signals above the noise level are so large (e.g. see Figure 5.11). Thus time resolved plots for individual ablation shots are also interesting.

The timing analysis of 8 randomly selected individual ablation shots from the same averaged experiment (Figure 5.13a) are shown in Figure 5.14. It is observe that the particle scatter and fluorescence spectra do not always correlate with the Ba^+ ion current. The times when the fluorescence spectrum shows the poorest correlation with the Ba^+ ion current are the times when the sizes of the signals are small. It is possible that the maximum signals were missed during the periods when the CCD shutter was closed, but given the width of the current signals, this is unlikely.

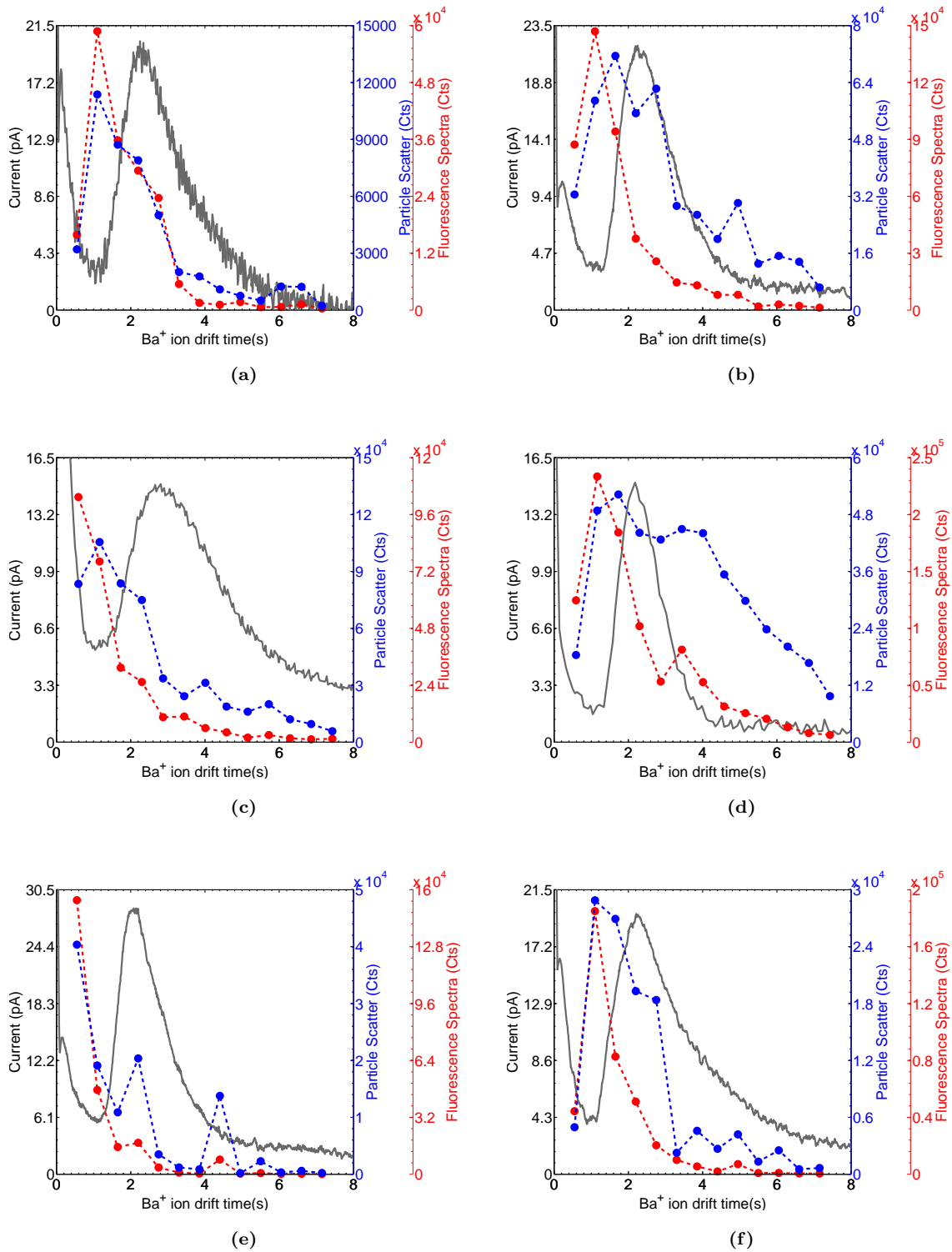


Figure 5.13: Time correlation of the particle scatter and fluorescence spectrum. Each point represents the average size of the particle scatter (blue) and fluorescence spectrum (red) in the frame. The current is the average of the individual currents.

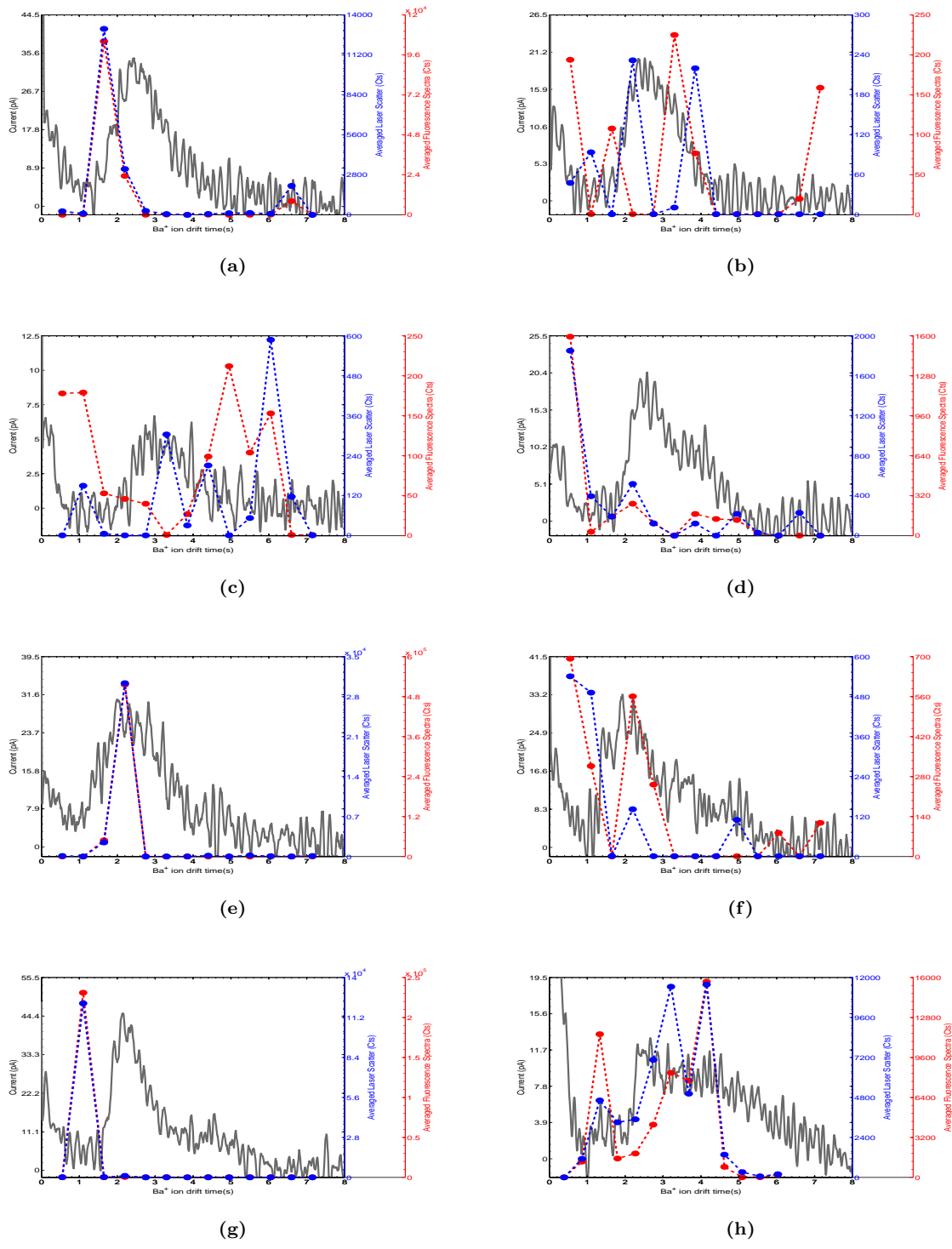


Figure 5.14: Time correlation of the size of the particle scatter (blue) and fluorescence spectrum (red) with Ba^+ current for randomly selected ablations shots for the same experiment as shown in the averaged analysis shown in Figure 5.13a.

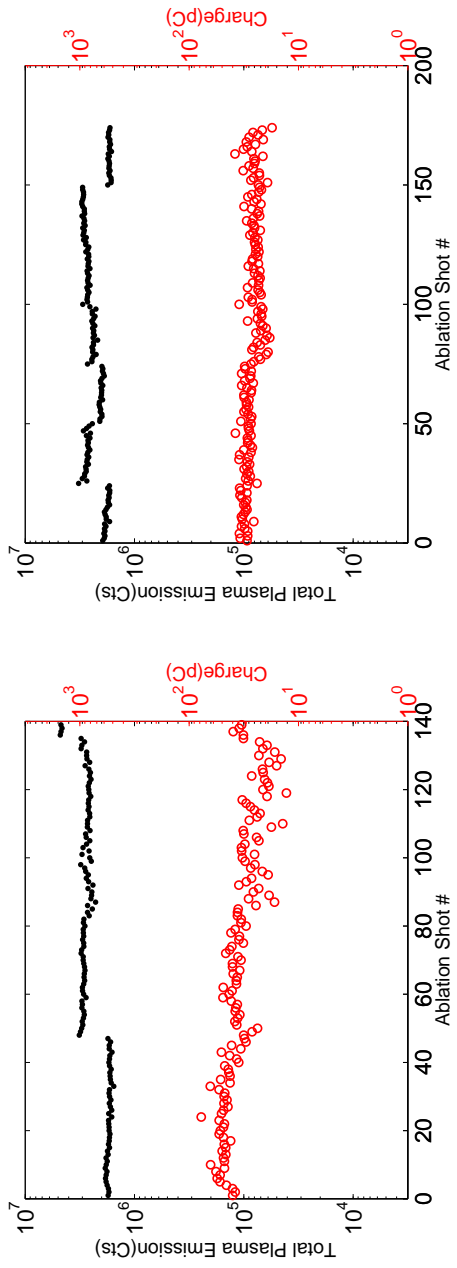
5.3.2 Cleaned Ba Metal and BaAl₄

The Ba⁺ ion charge and size of the plasma emission spectrum are compared in Figure 5.15 for 3 cleaned barium metal tip experiments (a,b,c) and one experiment with the BaAl₄ getter(d). The most noticeable difference from the oxidized experiments is that a current was detected for every laser ablation shot even after moving to a new spot. New spots can be identified on the plots by the slight jumps or dips in the plasma emission spectrum for the barium metal experiments.

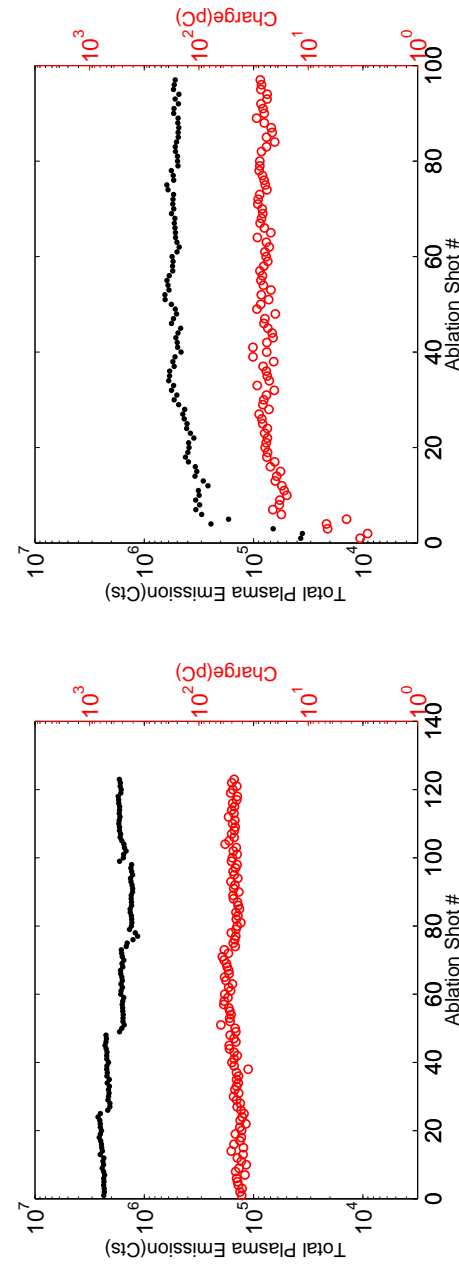
Only one spot was ablated on the getter. The charges of the first 4 shots for the getter experiment were noticeably smaller but definitely detectable; this might be evidence of a small oxide layer. These results are consistent with the results of the oxidized experiments after the Ba⁺ metal become visible. Since the charge is more stable in these experiments with the cleaned Ba⁺ metal tip, the changes of the size of the plasma emission spectrum are more evident. As mentioned earlier, this may be because the ablation spot is not being directly imaged.

The integrated particle scatter and integrated fluorescence are shown in Figure 5.16 as a function of ablation shot number. Only a small percentage of shots have particle scatter and fluorescence spectra above the noise level and most signals are below the noise level or negative. The dotted black vertical lines represent when the ablation spot was changed. These results provide evidence that the oxide layer has an influence on particle scatter and fluorescence spectra. The experiment ablating the BaAl₄ getter has a similar frequency of signals to the cleaned Ba⁺ metal experiments (Figure 5.16d). The same 2 orders of magnitude variation in the sizes of the particle scatter and fluorescence that was observed in the oxidized experiments is illustrated best in Figure 5.16a.

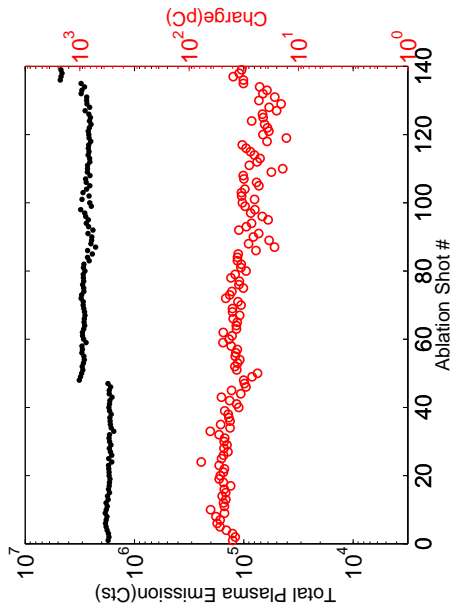
The size of fluorescence signal versus the laser scatter for signals above the noise levels individual ablation shots of all the cleaned tip experiments are plotted together in Figure 5.17. In Figure 5.18, the size of the particles scatter and fluorescence spectrum are plotted vs. charge. The colors represent different experiments. Since so few signals are observed in



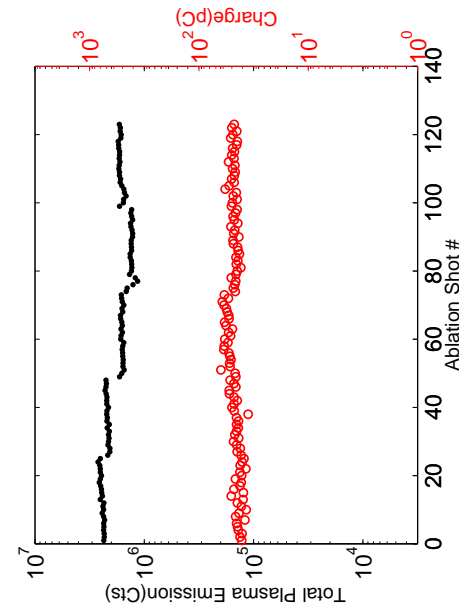
(a)



(b)

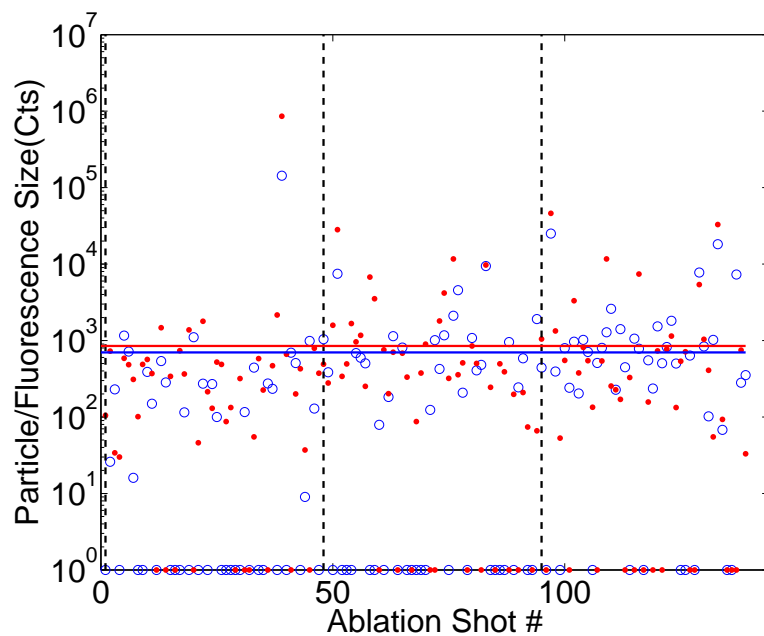


(c)

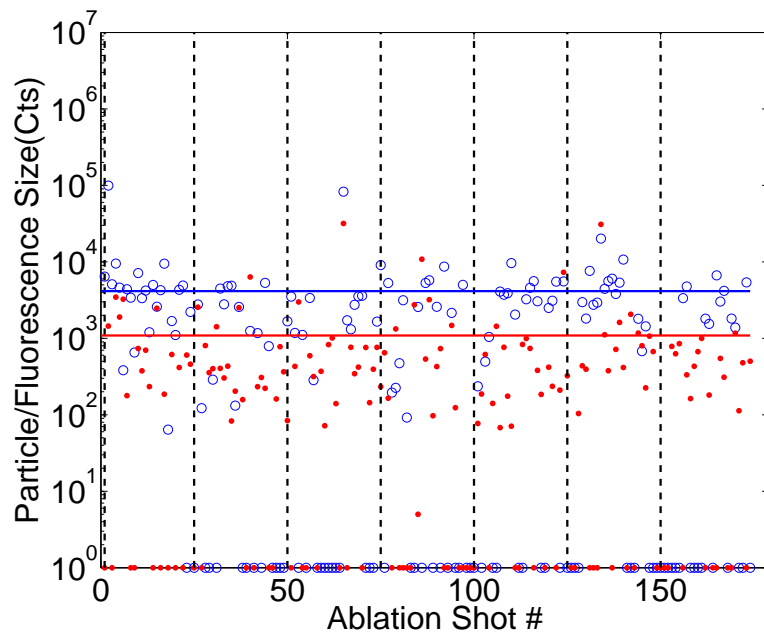


(d)

Figure 5.15: The comparison between the size of the plasma emission spectrum (black dots) and total Ba⁺ ion charge (red dots) after each ablation shot for the experiments conducted with the heavy white oxide layer removed (a,b,c) from the barium metal, and for the BaAl₄ getter (d).

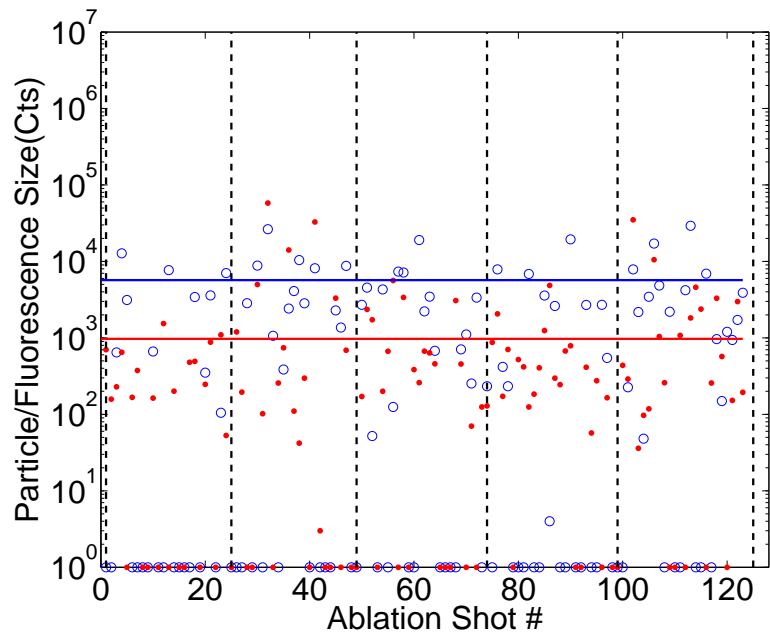


(a)

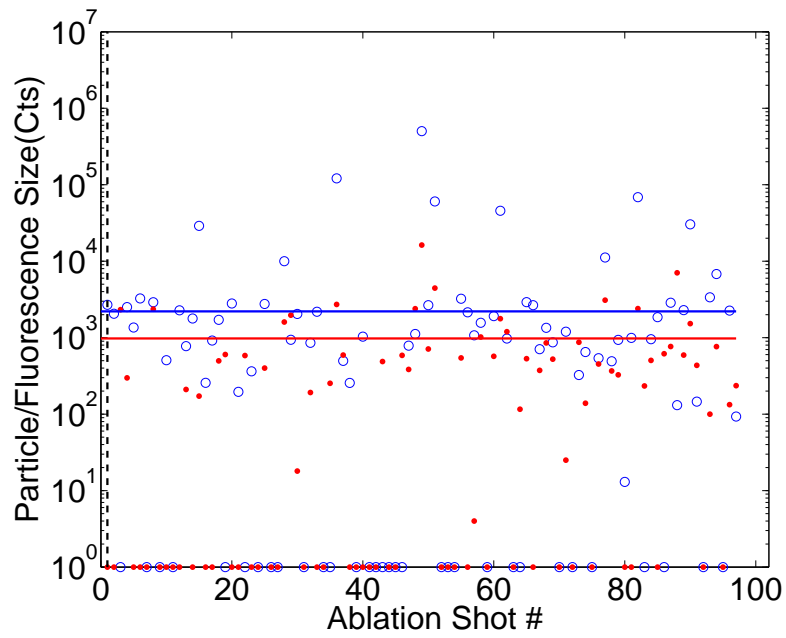


(b)

Figure 5.16: The total size of the particle scatter and fluorescence spectrum after each ablation shot for the same cleaned tip experiments shown in Figure 5.15. The circles and dots represent the size of the particle scatter and fluorescence spectrum for each ablation shot respectively. The black dotted lines represent when the ablation spot was changed for the barium metal experiments (a, b, c). Only on spot was ablated one the BaAl₄ getter (d). The red (fluorescence) and blue (particle scatter) lines are the noise levels.



(c)



(d)

Figure 5.16: see previous page for caption

these experiments, not much information is learned about the correlation of particle scatter, fluorescence spectra and the Ba^+ ion charge. But the general trends are similar to those observed in the oxidized tip experiments.

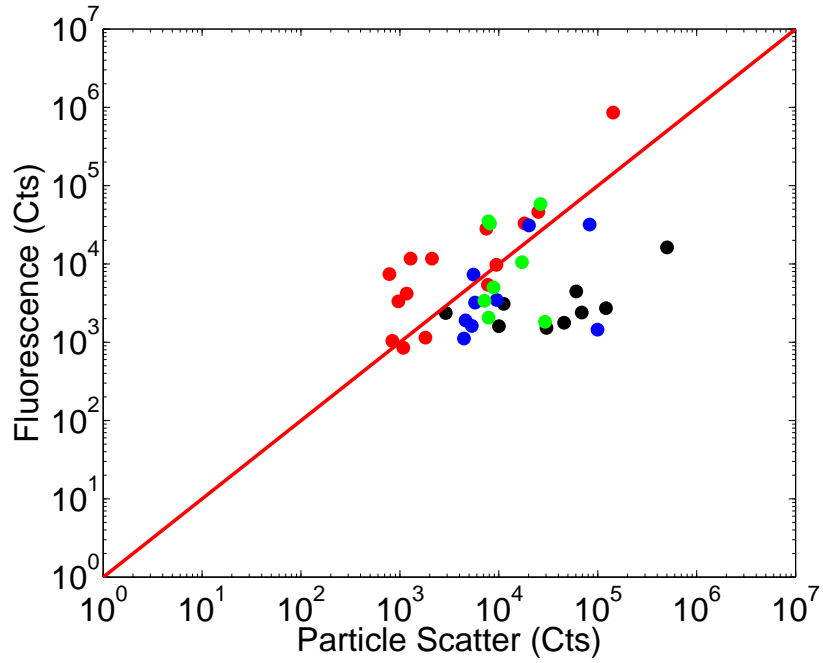


Figure 5.17: Size of the fluorescence spectrum vs. the size of the particle scatter for the 3 cleaned barium metal tip experiments (red, blue, green) and on BaAl_4 getter (black).

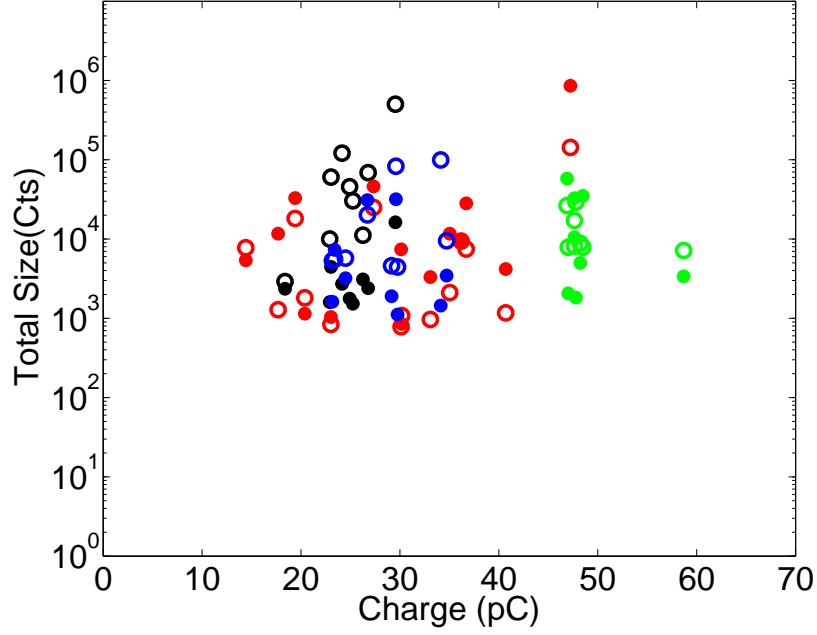


Figure 5.18: Size of the particle scatter/fluorescence spectrum vs. charge for 3 cleaned barium metal tip experiments (red, blue, green) and one BaAl₄ getter (black).

The time correlation plots for signals averaged over a whole experiment are shown in Figure 5.19. The results are generally consistent with the oxidized tip experiments and show that on average the fluorescence arrives before the current peaks. Time correlation plots for randomly selected shots for the experiment shown in Figure 5.16a with the most shots above the noise are shown in Figure 5.19. The individual shots also show that small fluorescence and scatter signals do not correlate well with the Ba⁺ ion current. This is also consistent with the oxidized tip experiments.

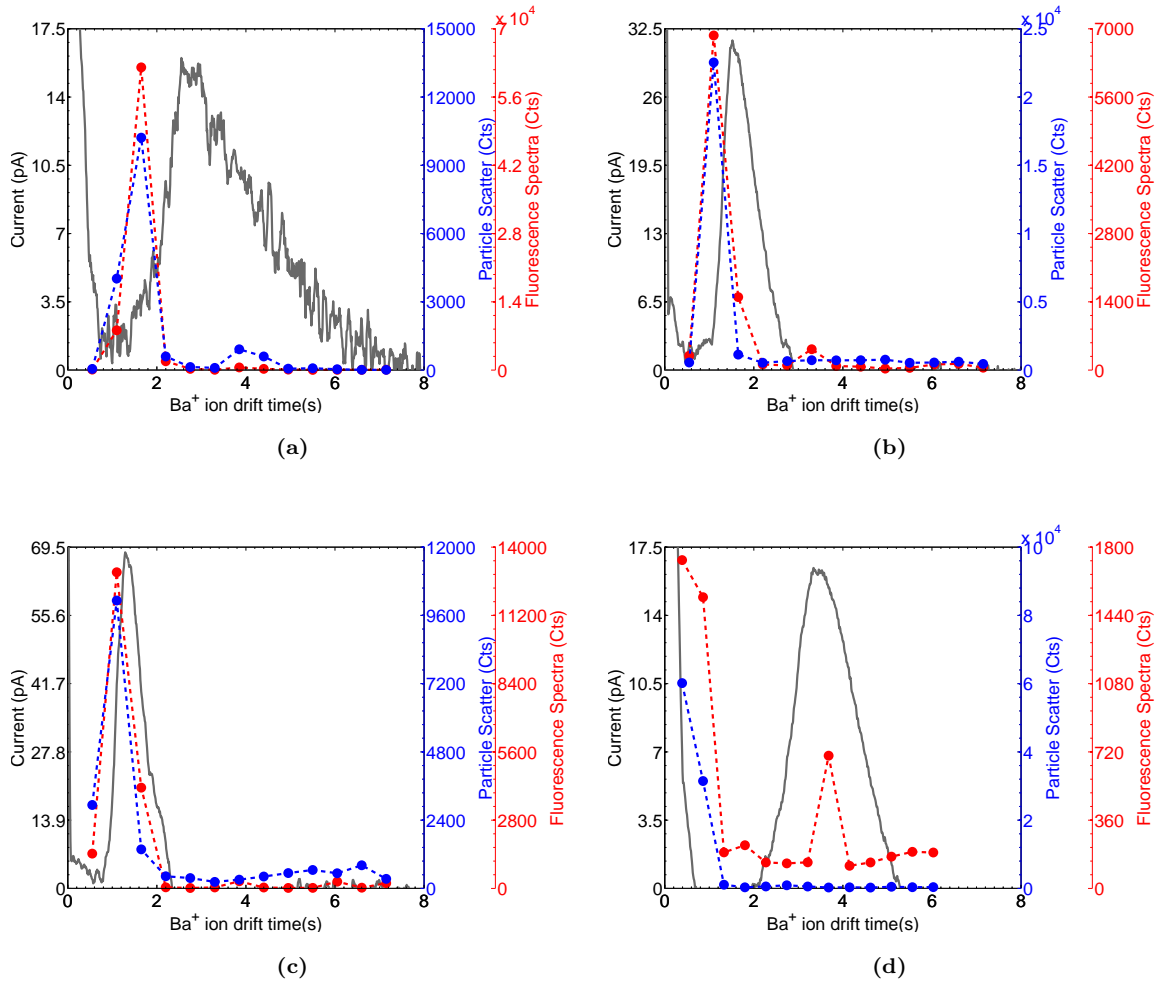


Figure 5.19: Time correlation of the particle scatter and fluorescence spectrum for experiments with the heavy oxide layer removed. Each point represent the average size of the particle scatter (blue) and fluorescence spectrum (red) in the frame. The current is the average of the individual currents. Plots a, b, and c are for the barium metal, and plot d is for the BaAl₄ getter.

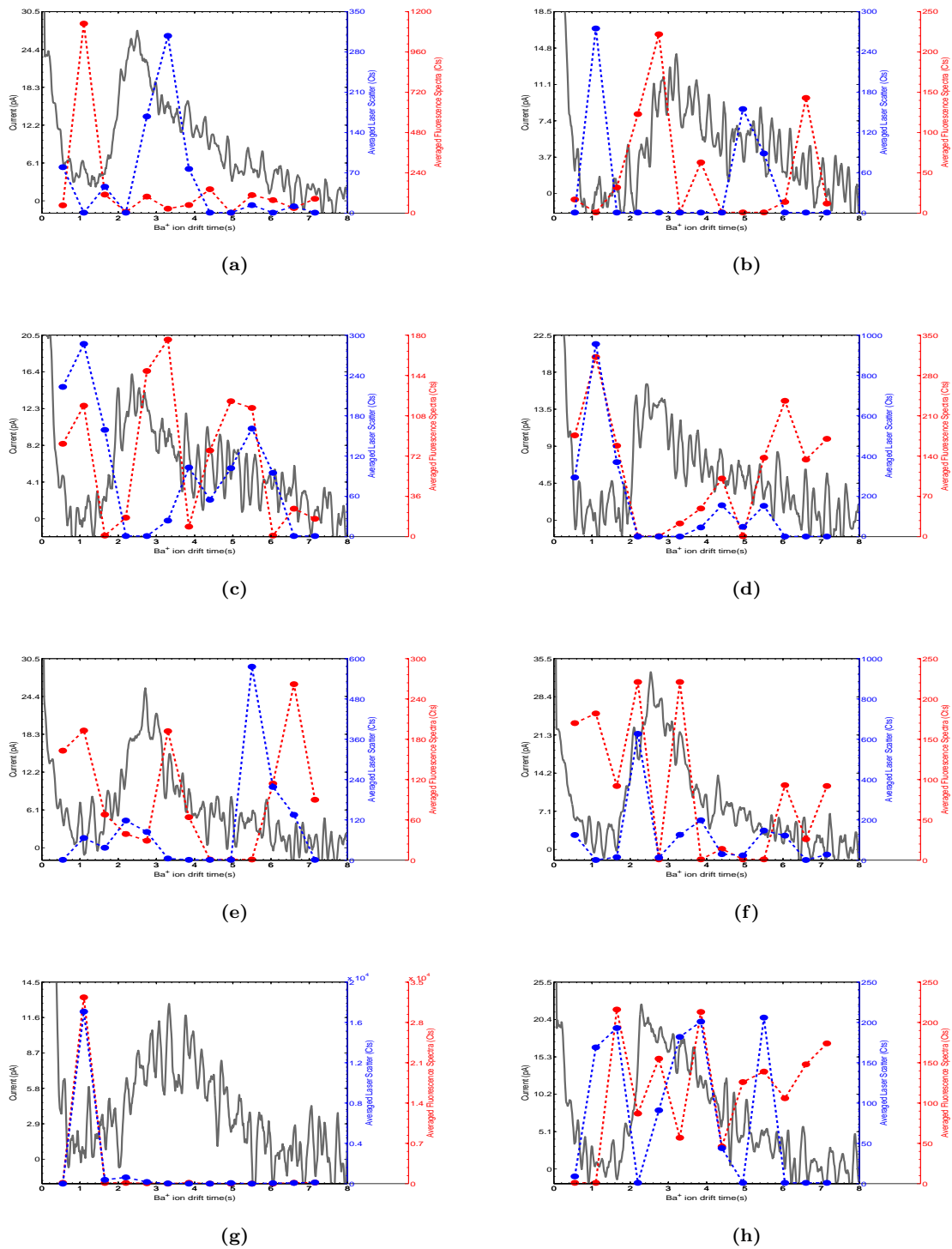


Figure 5.20: Time correlation of the particle scatter and fluorescence spectrum with Ba^+ current for randomly selected ablation shots for the same experiment as shown in the average analysis shown in Figure 5.19a.

5.4 Discussion

Many experiments studying the particle scatter and the fluorescence spectrum from the possible excitation of Ba^+ ions with 502nm light for different tip conditions have been reported. Fewer detailed studies with excitation using the other 8 wavelengths were performed.

Although the data shows large scatter in some cases, some key information could be extracted from experiments. (1) A strong correlation between the size of the plasma and the Ba^+ current was shown. This correlation is significant because it demonstrates that we do have Ba^+ ions passing through the liquid xenon. This result confirms a Ba^+ species as the ion measured in the mobility measurements of Jeng et al [34]. (2) The high percentage of particle scatter and fluorescence signals for the oxidized tip compared to the low percentage of signals observed when the thick white oxidized layer of the barium metal was removed was apparent in the data shown. This could be interpreted as evidence that the fluorescence spectrum might be associated with oxidized species such as BaO or BaO^+ from the ablation of the oxidized barium metal sample. A counter argument is that neither of these species was observed in the plasma emission spectrum. In addition, purity measurements after ablation show no contamination of oxygen in the bulk liquid xenon at the ppb level. The results, however, do not rule out contamination on the liquid xenon surface the Ba^+ ions pass through upon entering the liquid xenon. (3) On average, the timing of the fluorescence signal correlates better with the Ba^+ current than the timing of the particle scatter, especially when the total size of the fluorescence is large. The arrival time of the observed fluorescence and scatter is more erratic on individual ablation shots, especially when smaller signals were observed.

The overall conclusion of this Chapter is that because of the considerable amount of fluctuation of the data, in the experiments performed, it is not possible to confirm that the fluorescence observed in liquid xenon from the excitation with the discrete argon ion wavelengths is associated with Ba^+ ions.

Chapter 6

Summary

A considerable amount of effort has been given to understand the spectroscopy of Ba^+ ions in liquid xenon. A broad fluorescence spectrum has been observed when the Ba^+ ions are excited with the discrete argon ion laser wavelengths. From the studies explained in Chapter 5, we are unable to confidently determine that the fluorescence is due to the emission of the Ba^+ ions after excitation. Thus we could not confirm that Ba^+ ions fluoresce in liquid xenon.

An important positive result is that the linear correlation of the plasma emission spectra with the Ba^+ charge shown in this work confirms that the Ba^+ ion mobility measurement made by our group previously is indeed that of Ba^+ ions. This confirmation is important because, no matter the Ba tagging technique chosen, one will have to be able to follow the Ba daughter in the liquid.

Currently our group at CSU is conducting spectroscopy and mobility studies of Ba^+ ions at different xenon gas pressures. These experiments are interesting because the Ba^+ ions in all liquid xenon studies to date are created in 1-2 atm of xenon gas before they are drawn into the liquid. The gas studies might provide evidence that will shed some light on the ion species that enter the liquid xenon.

An unexpected major success of this thesis is the observation of the nonresonant multiphoton ionization (NRMPI) of liquid xenon. The order n of the nonlinear process was determined for ionization with pulsed laser beams of 221nm, 266nm, 280nm, and 355nm.

The values of n measured are consistent with the minimum number of photons needed to create a xenon-hole pair in the liquid xenon according the liquid xenon band gap. The 2-photon and 3-photon cross sections for ionization with 266nm and 355nm respectively are reported for the first time.

Since the NRMPI process is proportional to laser intensity to the power n , electrons are only created in a localized spot at the beam focus. As the order of n is increased, the position of the electrons is better defined, as the non focused part of the beam will contribute less. An exciting possible application in a liquid noble gas time projection chamber is that the localized source of electrons from NRMPI can be used as a way to determine the purity in different parts of the detector. The localized source can also be used as a way to obtain better accuracy in the event reconstruction because the beam focus would provide a known z position in the TPC. The recent choice of detector for the Long Baseline Neutrino Experiment (LBNE) is a very large detector containing 10's of kilotons of liquid argon. These methods might also be applicable to the LBNE detector.

Bibliography

- [1] Felix Boehm and Petr Vogel. *The Physics of Massive Neutrinos*. Cambridge University Press, 1992. 1, 6, 7
- [2] W Pauli. Letter to the Physical Society of Tübingen. *unpublished; the letter is reproduced in Brown, L.M., Physic Today*, 31:9,3, 1978. unpublished; the letter is reproduced in Brown, L.M.,. 1
- [3] E Fermi. *Z. Physik*, 88:161, 1934. 1
- [4] C. L. Cowan Jr., F. Reines, F. B. Harrison, H. W. Kruse, and A. D. McGuire. Detection of the free neutrino: A Confirmation. *Science*, 124(3212):pp. 103–104, 1956. 2
- [5] G. Danby, J-M. Gaillard, K. Goulianos, L. M. Lederman, N. Mistry, M. Schwartz, and J. Steinberger. Observation of high-energy neutrino reactions and the existence of two kinds of neutrinos. *Phys. Rev. Lett.*, 9:36–44, Jul 1962. 2
- [6] M. L. Perl and et al. Evidence for anomalous lepton production in $e^+ - e^-$ annihilation. *Phys. Rev. Lett.*, 35:1489–1492, Dec 1975. 2
- [7] DONUT Collaboration. Observation of tau neutrino interactions. *Physics Letters B*, 504(3):218 – 224, 2001. 2
- [8] B Pontecorvo. *Soviet physics, JETP*, 6:429 – 431, 1958. 2
- [9] B Pontecorvo. Neutrino experiments and the problem of conservation of leptonic charge. *Soviet Physics JETP*, 26:984, 1968. 3

- [10] Sakata S. Maki Z., Masami N. Remarks on the unified model of elementary particles. *Progress of Theoretical Physics*, 28:870–880, 1962. 3
- [11] Raymond Davis, Don S. Harmer, and Kenneth C. Hoffman. Search for neutrinos from the sun. *Phys. Rev. Lett.*, 20:1205–1209, May 1968. 4
- [12] Q. R. Ahmad and et al. Measurement of the rate of $\nu_e + d \rightarrow p + p + e^-$ interactions produced by ^8B solar neutrinos at the sudbury neutrino observatory. *Phys. Rev. Lett.*, 87:071301, Jul 2001. 4
- [13] J. N. Abdurashitov and et al. Measurement of the solar neutrino capture rate with gallium metal. *Phys. Rev. C*, 60:055801, Oct 1999. 4
- [14] T.A and Kirsten. Progress in GNO. *Nuclear Physics B - Proceedings Supplements*, 118(0):33 – 38, 2003. Proceedings of the XXth International Conference on Neutrino Physics and Astrophysics. 4
- [15] R. Becker-Szendy, C. B. Bratton, D. Casper, S. T. Dye, W. Gajewski, M. Goldhaber, T. J. Haines, P. G. Halverson, D. Kielczewska, W. R. Kropp, J. G. Learned, J. M. LoSecco, S. Matsuno, G. McGrath, C. McGrew, R. Miller, L. R. Price, F. Reines, J. Schultz, H. W. Sobel, J. L. Stone, L. R. Sulak, and R. Svoboda. Electron- and muon-neutrino content of the atmospheric flux. *Phys. Rev. D*, 46:3720–3724, Nov 1992. 4
- [16] K.S. Hirata and et al. Observation of a small atmospheric ν_μ/ν_e ratio in Kamiokande. *Physics Letters B*, 280(12):146 – 152, 1992. 4
- [17] Y. Ashie and et al. Evidence for an oscillatory signature in atmospheric neutrino oscillations. *Phys. Rev. Lett.*, 93:101801, Sep 2004. 4
- [18] K. Abe and et al. The T2K experiment. *Nuclear Instruments and Methods in Physics Research Section A: Accelerators, Spectrometers, Detectors and Associated Equipment*, 659(1):106 – 135, 2011. 4

- [19] P. Adamson and et al. First direct observation of muon antineutrino disappearance. *Phys. Rev. Lett.*, 107:021801, 2011. 4
- [20] Atsuto Suzuki and KamLand Collaboration. Results from kamland reactor neutrino detection. *Physica Scripta*, 2005(T121):33, 2005. 4
- [21] Eligio Lisi Leslie Camilleri and John F. Wilkerson. Neutrino masses and mixings: status and prospects. *Annual Review of Nuclear and Particle Science*, 58:343–369, 2008. 4
- [22] G Altarelli. Status of neutrino masses and mixing in 2009. 2009. 5
- [23] G. L. Fogli, E. Lisi, A. Marrone, A. Melchiorri, A. Palazzo, P. Serra, and J. Silk. Observables sensitive to absolute neutrino masses: Constraints and correlations from world neutrino data. *Phys. Rev. D*, 70:113003, Dec 2004. 5
- [24] M. Prall. The Katrin experiment and the pre-spectrometer at reduced retarding potential. *Progress in Particle and Nuclear Physics*, 66(2):418 – 423, 2011. Particle and Nuclear Astrophysics International Workshop on Nuclear Physics, 32nd Course. 5
- [25] Alessandro Melchiorri, Francesco De Bernardis, and Eloisa Menegoni. Limits on the neutrino mass from cosmology. *AIP Conference Proceedings*, 1256(1):96 – 106, 2010. 5
- [26] K. and Zuber. On the physics of massive neutrinos. *Physics Reports*, 305(6):295 – 364, 1998. 6
- [27] N. Ackerman and et al. Observation of two-neutrino double-beta decay in ^{136}Xe with the EXO-200 detector. *Phys. Rev. Lett.*, 107:212501, Nov 2011. 7, 10
- [28] O. Civitarese and J. Suhonen. Extracting information on the decays from the decays. *Nuclear Physics A*, 761(34):313 – 332, 2005. 7
- [29] H. Klapdor-Kleingrothaus, A. Dietz, and I. Krivosheina. Neutrinoless double beta decay: Status of evidence. *Foundations of Physics*, 32:1181–1223, 2002. 10.1023/A:1019722802931. 7

- [30] H. V. KLAPDOR-KLEINGROTHAUS and I. V. KRIVOSHEINA. The evidence for the observation of $0\nu\beta\beta$ decay: The identification of $\nu\beta\beta$ events from the full spectra. *Modern Physics Letters A*, 21(20):1547 – 1566, 2006. 7
- [31] C. E. Aalseth and et al. Comment on evidence for neutrinoless double beta decay. *Modern Physics Letters A*, 17(22):1475, 2002. 7
- [32] M. Auger and et al. The EXO-200 detector, part I: Detector design and construction. JInstr accepted for publication; arXiv <http://arxiv.org/abs/1202.2192v1>. 10
- [33] M. K. Moe. Detection of neutrinoless double-beta decay. *Phys. Rev. C*, 44:R931–R934, Sep 1991. 10, 12
- [34] S-C Jeng, W M Fairbank Jr, and M Miyajima. Measurements of the mobility of alkaline earth ions in liquid xenon. *Journal of Physics D: Applied Physics*, 42(3):035302, 2009. 10, 14, 17, 98
- [35] B. K. Sahoo, Md. R. Islam, B. P. Das, R. K. Chaudhuri, and D. Mukherjee. Lifetimes of the metastable ${}^2D_{\frac{3}{2},\frac{5}{2}}$ states in Ca^+ , Sr^+ , and Ba^+ . *Phys. Rev. A*, 74:062504, Dec 2006. 16
- [36] H.J. Reyher, H. Bauer, C. Huber, R. Mayer, A. Schfer, and A. Winnacker. Spectroscopy of barium ions in He II. *Physics Letters A*, 115(5):238 – 244, 1986. 16
- [37] Frank S and Ham. The Jahn-Teller effect: A retrospective view. *Journal of Luminescence*, 85(4):193 – 197, 2000. 16
- [38] Milton W. Cole and Richard A. Bachman. Structure of positive impurity ions in liquid helium. *Phys. Rev. B*, 15:1388–1394, Feb 1977. 17
- [39] V. E. Bondybey and J. H. English. Ion–matrix interactions: Optical spectrum of the Ca^+ cation in solid argon. *The Journal of Chemical Physics*, 75(1):492–493, 1981. 17

- [40] L. C. Balling, M. D. Havey, and J. F. Dawson. Absorption and emission spectra of Na atoms trapped in rare-gas matrices. *The Journal of Chemical Physics*, 69(4):1670–1675, 1978. 19
- [41] L. C. Balling, M. D. Havey, and J. J. Wright. Absorption and emission spectra of k atoms trapped in rare-gas matrices. *The Journal of Chemical Physics*, 70(5):2404–2408, 1979. 19
- [42] C. Crepin-Gilbert and A. Tramer. Photophysics of metal atoms in rare-gas complexes, clusters and matrices. *International Reviews in Physical Chemistry*, 18(4):485 – 556, 1999. 19
- [43] C.Y. She and et al. Measuring the velocity of individual atoms in real time. *Opt. Lett* 2, 2:30, 1978. 21
- [44] M. Goeppert-Mayer. Elementary processes with two quantum transitions. *Annalen der Physik*, 18(7-8):466–479, 2009. 21
- [45] G.S. Voronov and N.B. Delone. Multiphoton ionization of the hydrogen molecule in the strong electric field of ruby laser emission. *Sov. Phys.-JETP Letter. (Engl. Transl.)*, 1:42, 1965. 21
- [46] C. C. Lim. Indium seals for low-temperature and moderate-pressure applications. *Review of Scientific Instruments*, 57(1):108–114, 1986. 29
- [47] Shie Chang Jeng. *New Fluorescence technique to search for neutrino masses by identification of $0\nu\beta\beta$ decay $^{136}\text{Ba}^+$ ion daughters in liquid xenon*. PhD thesis, Colorado State University, 2004. 31
- [48] O. Bunemann, T. E. Cranshaw, and J. A. Harvey. Design of grid ionization chambers. *Canadian Journal of Research*, 27a(5):191–206, 1949. 36

- [49] George Bakale, Ulrich Sowada, and Werner F. Schmidt. Effect of an electric field on electron attachment to sulfur hexafluoride, nitrous oxide, and molecular oxygen in liquid argon and xenon. *The Journal of Physical Chemistry*, 80(23):2556–2559, 1976. 41
- [50] P. Benettiet and et al. A simple and effective purifier for liquid xenon. *Nuclear Instruments and Methods in Physics Research Section A: Accelerators, Spectrometers, Detectors and Associated Equipment*, 329(12):361 – 364, 1993. 41